SYNTHESIS OF NEEDLE-LIKE AND ROD-LIKE NANO $BACO_3$ PARTICLES

A Thesis Submitted to
the Graduate School of Engineering and Sciences of
İzmir Institute of Technology
in Partial Fulfillment of the Requirements for the Degree of

MASTER OF SCIENCE

in Chemical Engineering

by
Tuğçe Nefise KAHYAOĞLU

August, 2016

İZMİR

We approve the thesis of **Tuğçe Nefise KAHYAOĞLU**

Examining Committee members:

Assoc. Prof. Dr. Ekrem ÖZDEMİR

Department of Chemical Engineering, İzmir Institute of Technology

Prof. Dr. Selahattin YILMAZ

Department of Chemical Engineering, İzmir Institute of Technology

Assoc. Prof. Dr. Şerafettin DEMİÇ

Department of Material Science and Engineering, Katip Çelebi University

1 August 2016

Assoc. Prof. Dr. Ekrem ÖZDEMİR

Supervisor, Department of Chemical Engineering,

İzmir Institute of Technology

Prof. Dr. Fehime ÇAKICIOĞLU ÖZKAN

Head of the Department of

Chemical Engineering

Prof. Dr. Bilge KARAÇALI

Dean of the Graduate School of

Engineering and Sciences

ACKNOWLEDGMENTS

I would like to express my gratitude to my supervisor, Assoc. Prof. Dr. Ekrem ÖZDEMİR, whose experience, encouragement, stimulating and suggestions enabled me to develop an understanding of the subject.

I would like to give my special thanks to our lab friends for their help and friendship. I would also like to give my special thanks to my best friend, Alaz İZER for their help, support and friendship.

I would like to thank to Center for Materials Research of Izmir Institute of Technology (İYTE-MAM) for SEM and XRD measurements.

Finally, I would like to express my thanks to my family for their motivation, love and endless support though my life experience.

ABSTRACT

SYNTHESIS OF NEEDLE-LIKE AND ROD-LIKE NANO $BACO_3$ PARTICLES

Barium carbonate ($BaCO_3$) has been widely used in soft and heavy industries such as ferrite magnets, solid oxide fuel cells, optical glass manufacturing, coatings, and polymeric composite materials as well as ceramic and brick industries. Using $BaCO_3$ in nano sizes will improve some of the physical properties of materials such as tensile strength, opacity, and thermal resistance. Production of $BaCO_3$ by chemical method requires extensive crystallization times and higher temperatures. Production of $BaCO_3$ by carbonation method usually yields particles with some agglomeration. In a study, conducted by our group funded by The Scientific and Technological Research Council (TUBITAK), a method was developed to synthesize hollow nano Calcium Carbonate ($CaCO_3$) particles. It was aimed to apply the developed method, which is unique in its kind, to produce nano $BaCO_3$ particles in different morphologies. Parameters such as effect of barium hydroxide ($Ba(OH)_2$) concentration, CO_2 flow rate, length in reaction chamber, and stirring rate were studied. Conductivity and pH values of the solution were monitored during crystallization. Surface morphology and crystal structure of the produced $BaCO_3$ particles were characterized by Scanning Electron Microscopy (SEM) and X-Ray Diffraction (XRD), respectively. It was shown that rod-like $BaCO_3$ particles produced in nano sizes with almost homogeneous size distributions. The rod-like $BaCO_3$ particles had a diameter from 100 to 400 nm and an aspect ratio of about from 3 to 10. The produced rod-like nano $BaCO_3$ were all in orthorhombic phase of $BaCO_3$ called as *Witherite*.

ÖZET

İĞNE ŞEKİLLİ VE ÇUBUK ŞEKİLLİ NANO $BACO_3$ TANECİKLERİNİN SENTEZLENMESİ

Baryum karbonat ($BaCO_3$), ferrit mıknatıs yapımı, katı oksit yakıt hücresi yapımı, kaplama ve optik cam sanayi, polimerik kompozit malzemeler ve aynı zamanda seramik ve tuğla gibi birçok hafif ve ağır sanayide kullanılmaktadır. Kimyasal metot ile üretilen $BaCO_3$ da uzun kristalizasyon zamanlarına ve yüksek sıcaklıklara ihtiyaç vardır. Karbonizasyon metodu ile üretilen $BaCO_3$ tanecikleri genellikle topaklaşma problemi ile sonuçlanmaktadır. Türkiye Bilimsel ve Teknolojik Araştırma Kurumu (TÜBİTAK) tarafından desteklenen ve araştırma grubumuz tarafından gerçekleştirilen bir çalışmada içleri boş nano kalsiyum karbonat ($CaCO_3$) taneciklerinin üretimleri başarılmıştır. Alanında tek olarak geliştirilen bu yöntemi kullanarak farklı morfolojilerde nano $BaCO_3$ tanecikleri üretilmesi amaçlanmıştır. Baryum hidroksit ($Ba(OH)_2$) konsantrasyonu, CO_2 akış hızı, reaksiyon bölmesi içindeki uzunluk ve karıştırma hızı gibi parametreler çalışılmıştır. Kristalizasyon esnasında çözeltinin iletkenlik ve pH değerleri monitör edilmiştir. Üretilen $BaCO_3$ taneciklerinin yüzey morfolojisi ve kristal yapısı sırasıyla Taramalı Elektron Mikroskobu (SEM) ve X-ışını Saçılımı (XRD) yöntemleriyle karakterize edilmiştir. Nano boyutlarda ve hemen hemen homojen boyut dağılımında çubuk şeklinde $BaCO_3$ taneciklerinin üretildiği gösterilmiştir. Çubuk şekilli nano $BaCO_3$ tanecikleri 100 nm ile 400 nm çaplarda ve 3 ile 10 çap uzunluğu başına boy uzunluğundadırlar. Üretilen çubuk şekilli $BaCO_3$ tanecikleri, viterit olarak adlandırılan, ortorombik fazdadır.

TABLE OF CONTENTS

LIST OF FIGURES

Figure **Page**

LIST OF TABLES

Table **Page**

CHAPTER 1

INTRODUCTION

Synthesis of inorganic materials such as carbonates with different morphologies and sizes has attracted by researchers and scientists recently. Barium carbonate ($BaCO_3$) is an important raw material due to its magnetization, its close relationship with aragonite, low loss and high permeability for various fields such as electronic, ceramic, paint, optical, chemical, brick and metallurgical industries (Tipcompor, Thongtem, Phuruangrat, & Thongtem, 2012). $BaCO_3$ is used as a filling material in various fields such as polymeric composites, producing plastics, paint, ceramics, and bricks and used as precursor for magnetic ferrites, ferroelectric materials, barium salts, electric condensers and optical glass (T. Hong, F. L. Chen, & C. R. Xia, 2015; Kaszuwara, Witkowski, Leonowicz, Pawlik, & Paszula, 2008; Omrani, Rostami, & Sedaghat, 2010; Shamsipur, Pourmortazavi, Hajimirsadeghi, & Roushani, 2013; Zak, Hashim, & Darroudi, 2014). Different morphologies usually show different behaviors and properties for the same material. $BaCO_3$ has high tensile strength due to their high aspect ratios. $BaCO_3$ is used in high temperature and stress applications one of which is fiber reinforcement of ceramic composites (Xu & Xue, 2006).

$BaCO_3$ has 3 polymorphisms such as orthorhombic, hexagonal and cubic. Under ambient conditions, just orthorhombic phase is stable. Orthorhombic phase is called as Witherite. The orthorhombic form of $BaCO_3$ transforms first with hexagonal phase and then cubic phase. The faces of crystals are generally rigid and striped horizontally. $BaCO_3$ with more thermodynamically stable crystal form is an important mineral as compared to other carbonates (Shamsipur et al., 2013; Zelati, Amirabadizadeh, & Kompany, 2011).

Production methods of $BaCO_3$ can be divided into two groups: one is the physical method and the other is the recrystallization as shown in Figure 1.1. In physical method, $BaCO_3$ can be produced from natural sources by crushing, grinding and sieving processes, respectively. However, cost of these processes is high and $BaCO_3$ particles

obtained from natural sources are usually in micron sizes and they are not in desired quality and purity. Consequently, $BaCO_3$ particles in desired quality and purity need to be produced by recrystallization methods.

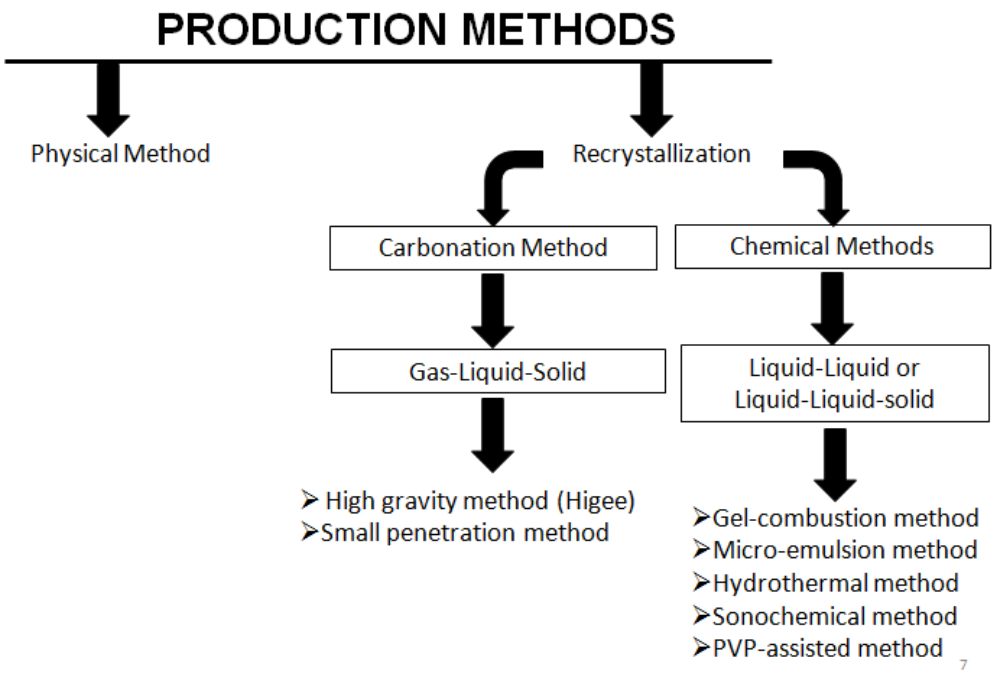

Figure 1.1. Schematic of $BaCO_3$ production methods

The recrystallization methods can be divided into two groups such as carbonation methods and chemical methods. Chemical methods include sol-gel, micro emulsion, hydrothermal, sonochemical, and PVP-assisted method. The carbonation methods include small penetration method which have already been developed by our research team and high gravity method (Higee). Gas-solid-liquid systems are participated in carbonization methods and liquid-liquid or liquid-liquid-solid systems are participated in chemical methods (P.-C. Chen, Cheng, Kou, Shia, & Chung, 2001; Khorsand, Habibian, Rohani, & Zarei, 2010).

$BaCO_3$ particles have been produced with various morphologies and sizes. These morphologies can be listed as bundle-like, rod-like, pencil-like, needle-like, sphere-like, spindle-like, dendritic-like particles. These different morphologies have been obtained by different synthesis methods, however, each one has advantages and disadvantages (Xu & Xue, 2006).

The aims of this thesis were to apply newly developed method by our research group recently for the hollow nano $CaCO_3$ particles on the synthesis of value added $BaCO_3$ particles and to produce $BaCO_3$ in nano sizes and rod-like morphology by homogeneous size distribution and also to investigate the effect of parameters such as barium hydroxide ($Ba(OH)_2$) concentration, CO_2 flow rate, length of reaction chamber and stirring rate on the morphology and sizes of $BaCO_3$.

CHAPTER 2

LITERATURE REVIEW

2.1. Usage of $BaCO_3$

Barium carbonate is used in producing magnetic barium ferrites. By reaction of barium carbonate ($BaCO_3$) and iron(III) oxide (Fe_2O_3) by mechanical alloying, barium ferrites were produced (Kaszuwara et al., 2008). Barium ferrites are important for hard magnetics with their high chemical resistance and low cost. Particle size is an important parameter for magnetic properties. Magnetic properties can be altered by using particles in nano sizes. High resistance of a magnetic material to changes in magnetization has nanosize particles.

$BaCO_3$ is also used to increase the reduction activity of oxygen in solid oxide fuel cells. Performance of solid fuel cells (SOFCs) is controlled by oxygen reduction reaction (ORR) in the cathodes. Nanoscale $BaCO_3$ particles are preferred due to nanostructured electrodes which could increase the surface area of electrocatalyst. $BaCO_3$ are connected to electrodes by impregnation and act as high temperature oxygen reduction catalyst (T. Hong, F. Chen, & C. Xia, 2015).

$BaCO_3$ is also used in optical glass industry. Optical properties of glass are improved by the reaction of $BaCO_3$ with some metal oxides via several production methods. When concentration of $BaCO_3$ increases, resonance frequency of permittivity and refractive index are improved (Zak et al., 2014).

In coating industry, $BaCO_3$ is used by addition of $BaCO_3$ into epoxy matrix to form composites. $BaCO_3$ has an effect of thermal curing of epoxy/1,8-naphthalene diamine system (Omrani et al., 2010). In addition, $BaCO_3$ is used in several industries such as ceramics, bricks and so on and these are common application of $BaCO_3$ but optic industry, coating industry, making ferrite magnets and making fuel cells are advanced technologies for the usage of $BaCO_3$.

2.2. Production Methods of $BaCO_3$

Production methods of barium carbonate are divided into two groups as physical methods and recrystallization methods. In physical method, $BaCO_3$ is produced from natural sources by crushing, grinding and sieving processes. The cost for these processes is high and the produced $BaCO_3$ is not in desired quality, purity, sizes and morphology. Therefore, $BaCO_3$ need to be produced by recrystallization. Recrystallization is also divided into two groups as carbonation method which includes small penetration method and high gravity method and chemical methods which includes sol-gel technique, sonochemical method, hydrothermal method, micro-emulsion method and so on.

Liquid-Liquid or Liquid-Liquid-Solid systems are employed in chemical method. Gas-Liquid-Solid systems are participated in carbonation method. By gas-solid-liquid system, production of $BaCO_3$ was investigated from Kubota et al. by bubbling of CO_2 in a solution of barium sulfide in two semi-batch reactors. $BaCO_3$ which has pillar-like morphology and larger size was obtained (P.-C. Chen et al., 2001; Khorsand et al., 2010). Chen et al. studied the production of $BaCO_3$ in a liquid-liquid system. As a result of this production, morphology of $BaCO_3$ particles were affected by pH values of solution and initial concentration of reactants (P.-C. Chen et al., 2001).

2.3. Chemical Production Methods of $BaCO_3$

In the literature, there are many studies by chemical methods to produce $BaCO_3$ particles. These methods are hydrothermal method (Xu & Xue, 2006), mechano-chemical method (Moayyer, Ataie, Nozari, & Jafari, 2013), sol-gel method (Zelati, Amirabadizadeh, Kompany, & Larimi), solid-state decomposition route (Dadkhah, Salavati-Niasari, & Davar, 2013), micro-emulsion method (Li et al., 2006), sonochemical method (Alavi & Morsali, 2008), PVP-assisted method (Zeng et al., 2011), thermal method (Cho & Huh, 2012).

In hydrothermal method, crystallization occurred between barium chloride ($BaCl_2$) and urea ($CO(NH_2)_2$) with mole concentration of 6:1 as urea/Ba^{+2} at 90°C and 12 hour in Teflon-lined stainless steel autoclave with a capacity of 40 ml. As a result of

this method, hexagonal pencil-like shaped $BaCO_3$ particles were produced in 5 µm diameter and 50 µm length as shown in Figure 2.1 (Xu & Xue, 2006). This method needed high temperatures and long reaction times.

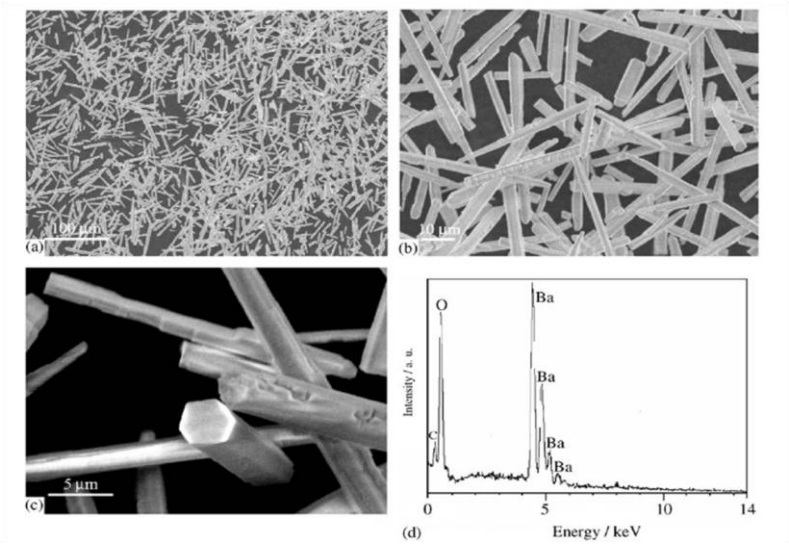

Figure 2.1. SEM images of $BaCO_3$: (a) and (b) low magnification view (c) high magnification view, (d) EDX (Source: Xu & Xue, 2006)

In mechano-chemical method, the crystallization occurred between barium hydroxide octahydrate ($Ba(OH)_2.8H_2O$) and sodium carbonate (Na_2CO_3) in a ball mill with different milling times (10, 20, 30 and 300 minutes) and different process control agents as ethanol, polyvinyl alcohol (PVA) and stearic acid at 30 minutes. Figure 2.2 shows those pencil-like and globular-like shapes of $BaCO_3$ particles. There was no morphology effect of increasing milling time on $BaCO_3$ particles in this method (Moayyer et al., 2013).

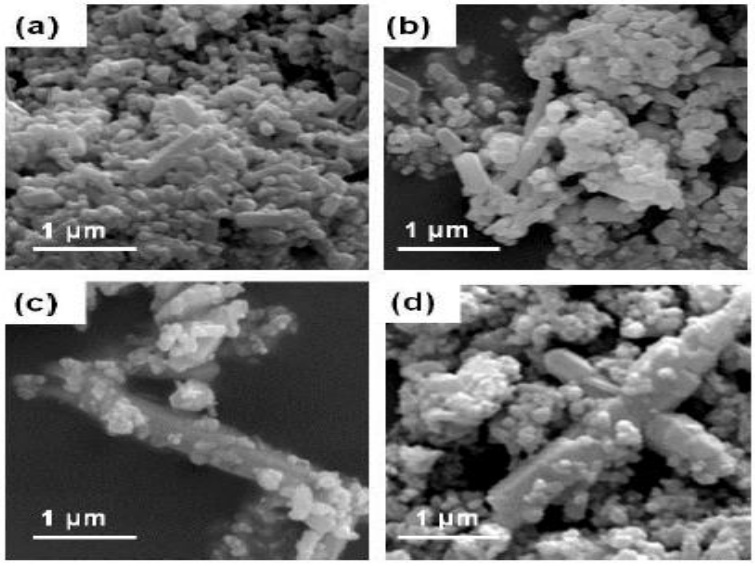

Figure 2.2. SEM images of $BaCO_3$ milled for (a) 10 min (b) 20 min (c) 30 min (d) 300 min (Source: Moayyer et al., 2013)

However, as shown in Figure 2.3 by the addition of ethanol, pencil-like morphology was dominant, globular-like morphology was dominant by addition of PVA, and lower amounts of pencil-like $BaCO_3$ particles and higher amounts of globular-like $BaCO_3$ particles in the presence of stearic acid were present. There was an agglomeration problem among particles. The lowest mean particle size was provided by the addition of stearic acid and 30 minutes milled as 54 nm (Moayyer et al., 2013).

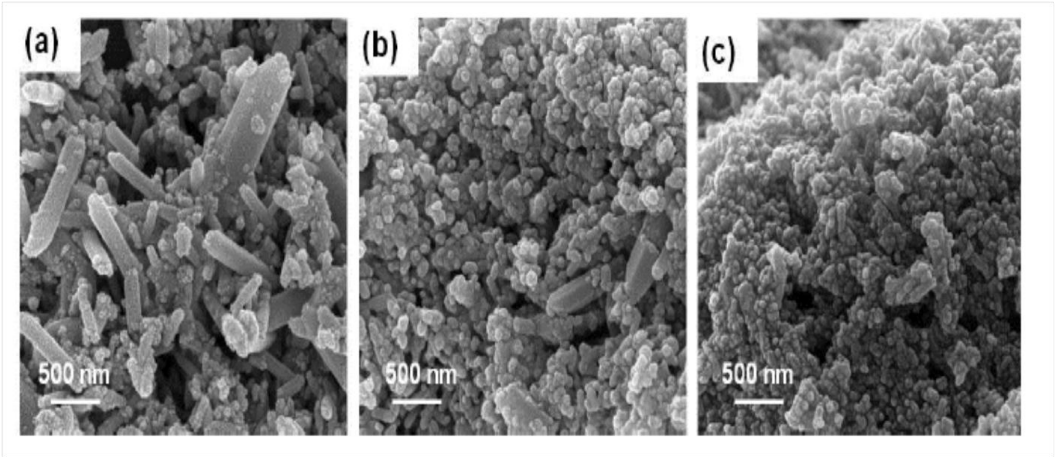

Figure 2.3. FESEM images of 30 minutes milled $BaCO_3$ particles with addition of 2 wt.% (a) ethanol (b) PVA (c) stearic acid (Source: Moayyer et al., 2013)

In gel-combustion (sol-gel) method, there were several stages for the preparation of sol, preparation of gel, gel combustion and calcination, respectively. In sol preparation stage, barium nitrate ($Ba(NO_3)_2$) solution was prepared and added to citric acid at 70°C. Then sol was evaporated at 80°C in gel preparation stage. At 100°C, auto combustion was done and nitric acid (HNO_3) was added (Zelati et al., 2011). Effect of different calcination temperatures (450°C, 600°C and 750°C) on mean crystallite size of $BaCO_3$ was studied. According to Table 2.1, mean crystallite size increases with increasing calcination temperatures.

Table 2.1. Mean Crystallite size of $BaCO_3$ particles on different calcination temperatures (Source: Zelati et al., 2011)

Calcination temperature	<d>
No calcination	33.3 nm
T = 450 °C	33.6 nm
T = 600 °C	34 nm
T = 750 °C	35 nm

Producing $BaCO_3$ from barium-*o*-phthalate ($Ba(Pht)(H_2O)_2$) was studied by solvent free thermal decomposition route. Prepared $Ba(Pht)(H_2O)_2$ was exposed to heat treatment at temperatures at 400°C, 500°C, 600°C and 700°C in air for 3 h. According to Figure 2.4, at 500°C, the smallest particle size with 35 nm of width and 70 nm of length and best morphology was obtained as bean-like shaped and (Dadkhah et al., 2013).

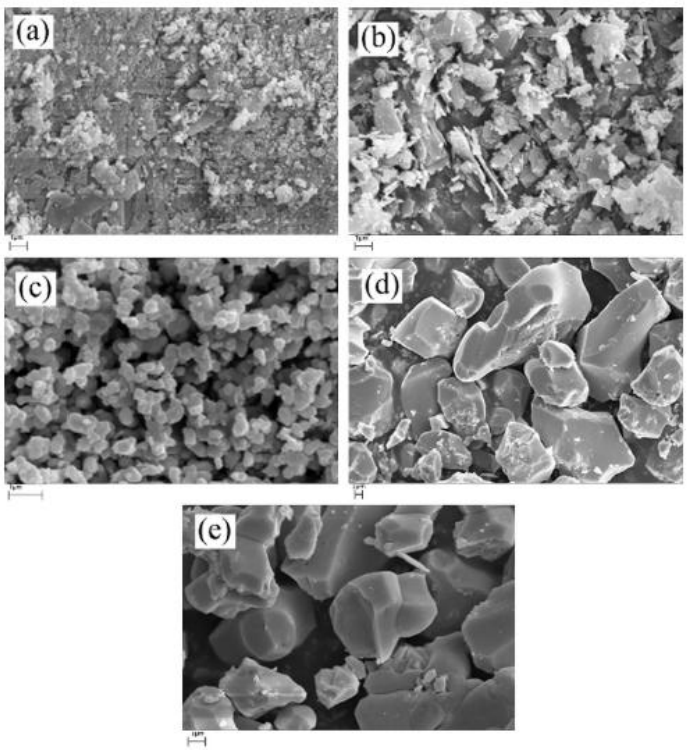

Figure 2.4. SEM images of (a) $Ba(Pht)(H_2O)_2$; $BaCO_3$ occurred at (b) 400°C, S1 (c) 500°C, S2 (d) 600°C, S3 (e) 700°C, S4 (Source: Dadkhah et al., 2013)

Also Cho and Huh studied hydrothermal method. Solution of $Ba(NO_3)_2$, glucose, cyclohexane, cetyltrimethylammonium bromide (CTAB) and *N,N,N',N'*-tetramethykethylenediamine (TMEDA) was prepared and put into Teflon-lined stainless steel autoclave which has 100 ml capacity at 140°C for 16 hour. Effect of different reaction temperatures (80°C, 100°C, 120°C, 140°C) on morphology of $BaCO_3$ particles was investigated. According to Figure 2.5, at 140°C, urchin-like $BaCO_3$ particles were produced in Figure 2.4-(d). Also, in Figure 2.5-(f) at 140°C, spindle-like $BaCO_3$ particles were produced in the absence of cyclohexane (Cho & Huh, 2012).

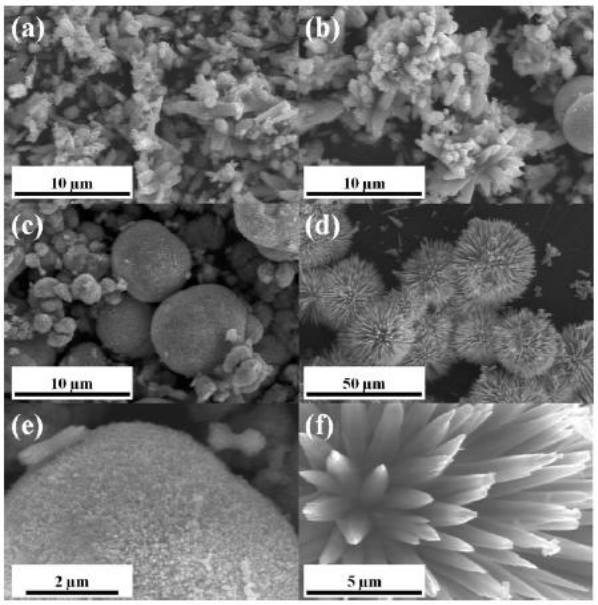

Figure 2.5. SEM images of $BaCO_3$ particles at reaction temperatures (a)80°C (b)100°C (c and e)120°C (d and f)140°C (Source: Cho & Huh, 2012)

Microemulsion method of production of $BaCO_3$ was studied by two solutions were prepared by dissolving of CTAB or Np_{10} in 20 ml of cyclohexane and 2 ml of n-pentanol. Then 0.18 ml of 0.1 M Na_2CO_3 and 0.1 M $BaCl_2$ were added to these solutions. These solutions called as A1 and stirred for 12 hours. A1 solutions were placed into Teflon lined stainless steel autoclave with a volume of 50 ml at 140°C and 12 hour of crystallization, then, $BaCO_3$ particles were synthesized. Effects of different concentrations of surfactants and reactants on $BaCO_3$ particle morphology were investigated. Figure 2.6 shows belt-like $BaCO_3$ particles were produced with sizes of 200 nm in diameter and 3.4 µm in length. According to this figure, some of nanobelts were agglomerated and some of block $BaCO_3$ particles were occurred as the temperature was increased to 180°C from 140°C (Li et al., 2006).

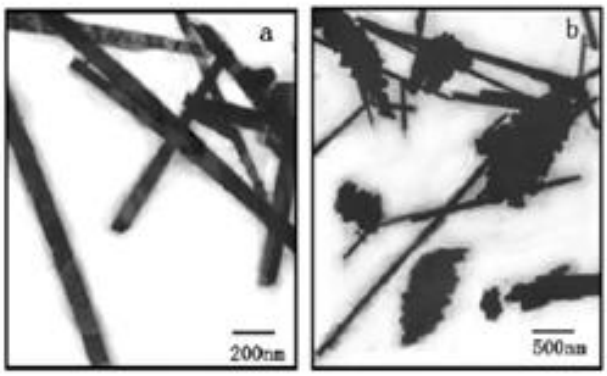

Figure 2.6. TEM images of $BaCO_3$ in the microemulsion with hydrothermal treating for 12 h ([$BaCl_2$] = [Na_2CO_3] = 0.1 M, [NP10] = 0.127 M) (a) 140°C (b) 180°C (Source: Li et al., 2006)

In the sonochemical method, crystallization was realized between barium acetate ($Ba(CH_3COO)_2$) and sodium hydroxide (NaOH) or tetramethylammonium hydroxide (TMAH) with different aging times such as 30 min, 1 h and 2 h and different sonication powers such as 3-6 W, 12-15 W and 36-39 W. As can be seen in Figure 2.7-(d), rod like and spherical like $BaCO_3$ particles were produced, but these particles seem to be aggregated (Alavi & Morsali, 2008).

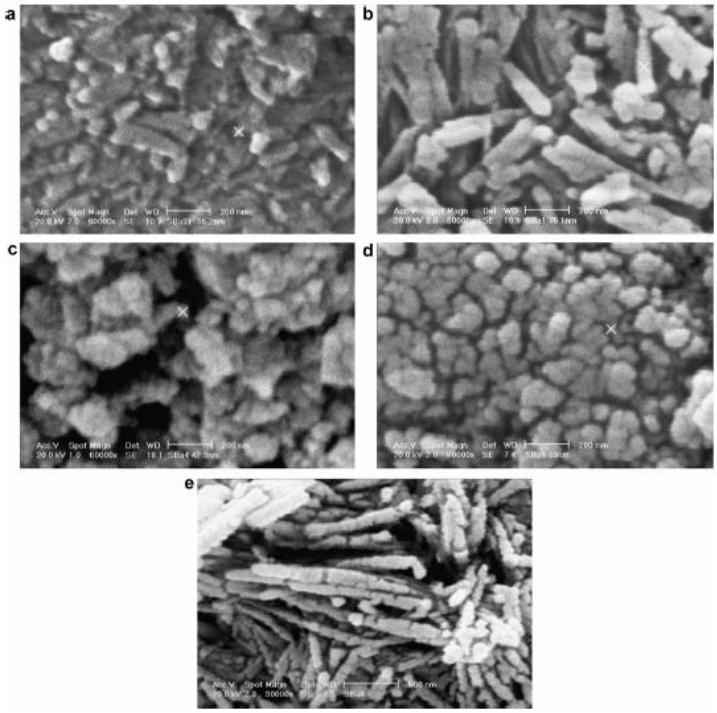

Figure 2.7. SEM images of $BaCO_3$ (a) sample no 3 (b) sample no 1 (c) sample no 9 (d) sample no 10 (e) sample no 8 (Source: Alavi & Morsali, 2008)

$BaCO_3$ particles were produced by PVP-assisted method by aging of barium nitrate ($Ba(NO_3)_2$) solution with the addition of sodium carbonate (Na_2CO_3), lactic acid and polyvinyl pyrrolidone (PVP) with different reaction conditions. Figure 2.8 shows the shape of $BaCO_3$ particles which changed from rod-like to dendritic-like by increasing molar ratio of lacticacid/Ba^{2+} (Zeng et al., 2011).

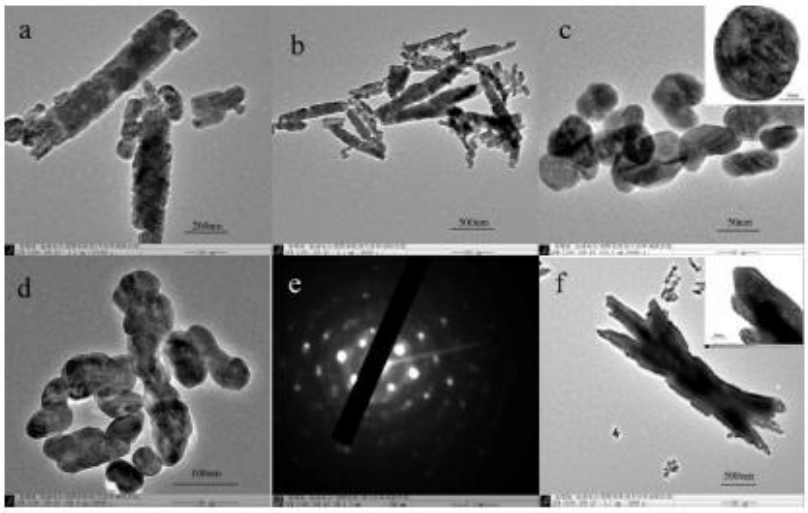

Figure 2.8. (a) SEM image of S1, TEM image of (b) S2, (c) S3, (d) S4, (f) S5, (e)SAED pattern of S3 (Source: Zeng et al., 2011)

2.4. Types of Carbonation Methods

Carbonation methods include small penetration method which was developed by our research group and high gravity technique (Higee). There is no study about the small penetration method for production of $BaCO_3$ in the literature. Small penetration method was applied for the first time on this study to produce nano $BaCO_3$ particles.

High gravity (Higee) technique was designed for resource and energy savings, space saving by minimizing the equipment scale in a rotating packed bed (RPB) by Ramshaw and Mallison in 1979. Production of $CaCO_3$ was a first large scale application of RPB in China by using lime and CO_2 (J. Chen & Shao, 2003). Then, Higee technology was used for $BaCO_3$. Schematic of $BaCO_3$ production by Higee technique was shown in Figure 2.9. Desired amount of solution was prepared by addition of $Ba(OH)_2$ in H_2O via pumping of CO_2, the $BaCO_3$ slurry was obtained by carbonation. Different amounts of sodium hexametaphosphate (Na-HMP) were added to the slurry to provide a good dispersion of $BaCO_3$. Figure 2.10 shows that there was no difference on morphology between with using 4.4 g of Na-HMP and without Na-HMP. In both case, rod like $BaCO_3$ particles were obtained. When 35.2 g of Na-HMP was added, size of $BaCO_3$ particles becomes smaller to about 330 nm (Tai & Liu, 2006).

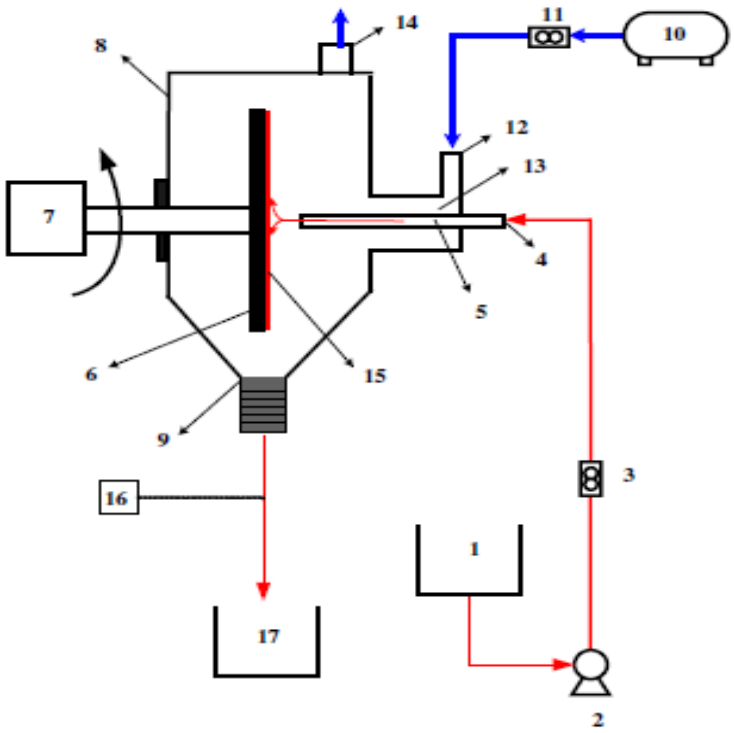

Figure 2.9. By carbonation, experimental schematic to produce $BaCO_3$ particles (Source: Tai & Liu, 2006)

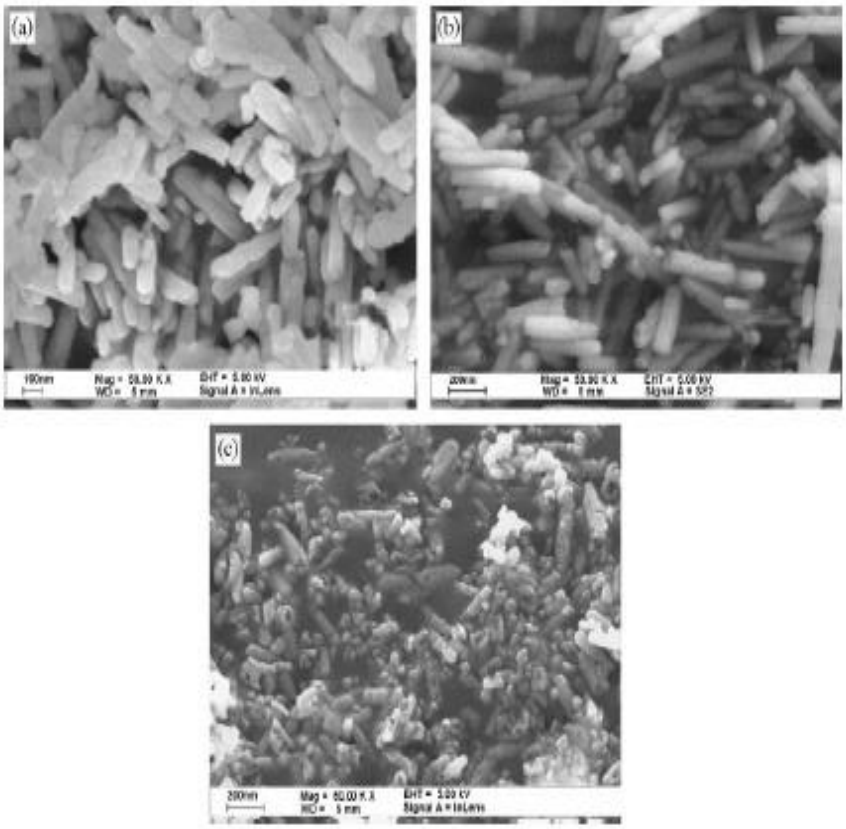

Figure 2.10. SEM images of Na-HMP: (a) absence of Na-HMP, (b) 4.4 g of Na-HMP/kg slurry, (c) 35.2 g of Na-HMP/kg slurry (Source: Tai & Liu, 2006)

2.5. Reactors Used in $BaCO_3$ Production

Decrease in size of particles is very important for chemical industry in order to use desired morphology of particles which can be used in different fields, quality of products, controlling the size, size and morphological distribution and increasing in efficiency (J. Chen & Shao, 2003; Zhao, Shao, & Chen, 2010). Reactors for recrystallization processes are designed with respect to controlling of parameters such as stirring rate, gas flow rate, liquid flow rate, concentration of surfactants and precursors, temperature, pressure, presence of additives, molar ratios of reactants on morphology and size of particles. Therefore, several different reactors were used to produce $BaCO_3$ particles. These reactors are Spinning Disk Reactor (SDR) (Tai & Liu, 2006), Fluidized Bed Reactor (Moguel, Muhr, Dietz, & Plasari, 2010), and Bubble Column Scrubber (P.-C. Chen, Shi, Du, & Chen, 2014).

Spinning Disk Reactor (SDR) was used to produce $BaCO_3$ particles via carbonation route by high gravity technique. It was used for the mass transfer between liquid and gas reactants to decrease contact area. Figure 2.11 shows the spinning disk reactor.

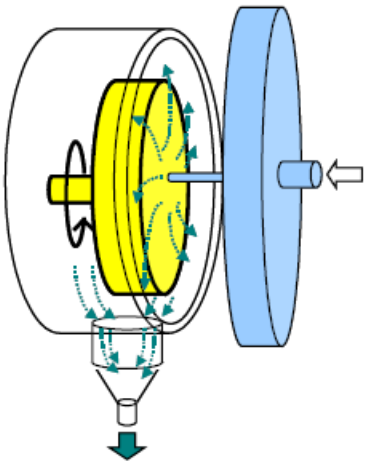

Figure 2.11. Spinning Disk Reactor (Source: Tai & Liu, 2006)

Figure 2.12 shows fluidized bed reactor to synthesize well defined nano particles. Fluidized bed reactor provides a way to control the particle size distribution, prevent agglomeration of particles and to have well defined crystalline $BaCO_3$ products forms (Moguel et al., 2010).

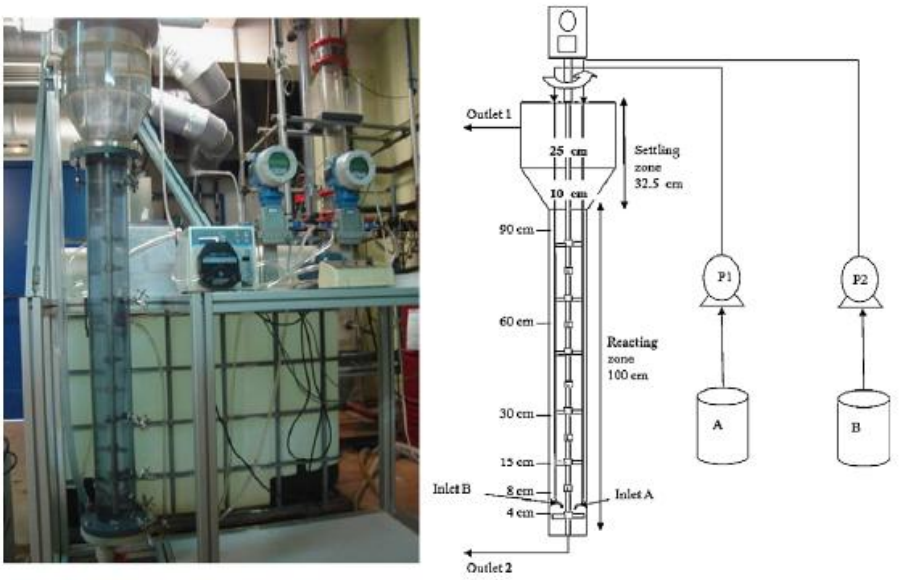

Figure 2.12. Fluidized Bed Reactor (Source: Moguel et al., 2010)

Bubble Column Scrubber was shown in Figure 2.13 which is important for adsorption of CO_2 in solutions. These types of reactors are widely used in several industries and it is also used in production of $BaCO_3$ particles since they have higher removal efficiency, higher mass and heat transfer coefficients, provide simplicity in controlling the liquid residence time, and easy construction (P.-C. Chen et al., 2014).

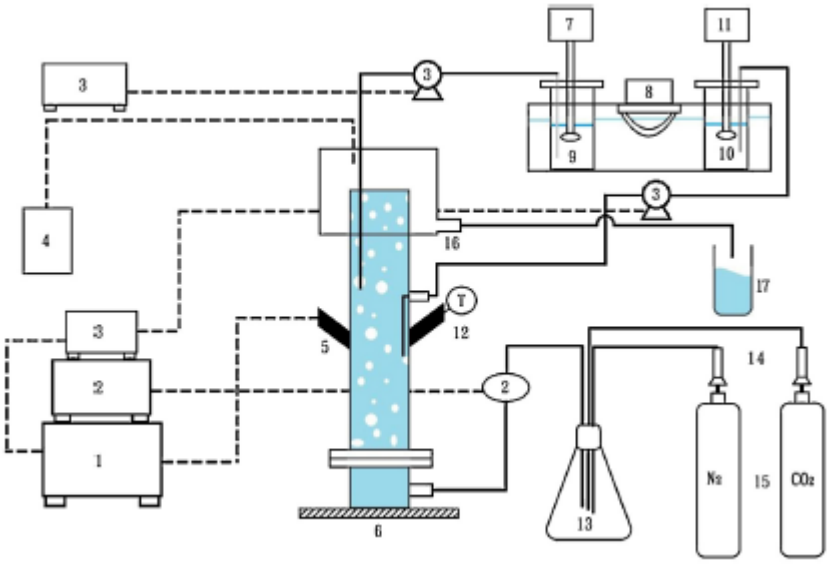

Figure 2.13. Continuous Bubble Column Scrubber; (1) pH-controller, (2) pressure gauge, (3)speed controller, (4) PCO_2 meter, (5) pH-electrode, (6) bubble column, (7) motor, (8) heater, (9) feed tank for $BaCl_2$, (10) feed tank for NaOH, (11) motor, (12) digital temperature (Source: P.-C. Chen et al., 2014)

In this thesis, small penetration method was used to produce rod-like and needle-like nano $BaCO_3$ particles. The method was previously developed by our research group and successfully employed to produce hollow nano $CaCO_3$ particles. Because of the developed procedure is simple to operate, believe that it will save time and energy to produce well defined nano $BaCO_3$ particles.

CHAPTER 3

MATERIALS AND METHODS

3.1. Materials

Barium hydroxide octahydrate ($Ba(OH)_2.8H_2O$), carbon dioxide (CO_2) and deionized water were used in the experimental procedures. $Ba(OH)_2.8H_2O$ was purchased from Merck with a purity of ≥%98 and specifications were given in Table 3.1. Deionized water (DI) was used from a MilliQ (Millipore- Elix UV5/ Milli-Q) water purification system to a purity of 18.2 μohm at 25 °C. CO_2 gas was purchased from Güneş Sinai Gas Ltd., Turkey with a purity of %99,999.

Table 3.1. Specifications of $Ba(OH)_2.8H_2O$ (Source: http://www.merckmillipore.com)

Purity	≥ 98.0 %
Substances insoluble in dilute hydrochloric acid	≤0.01 %
Carbonate (as $BaCO_3$)	≤2.0%
Chloride (Cl)	≤0.002%
Sulphide (S)	≤0.001%
Heavy Metals (as Pb)	≤0.002%
Ca (Calcium)	≤0.005%
Fe (Iron)	≤0.001%
Sr (Strontium)	≤1.0 %
Substances not precipitated by dilute sulfuric acid (as sulphate)	≤0.2 %
Molecular weight	315.48 g/mol

3.2. Methods

3.2.1. Small Penetration Method

Small Penetration method was developed such that the amount of gas dissolved in the liquid phase may be controlled by a short contact time between the gas and the liquid phases at the flow system. The CO_2 gas was attempted to transform into a flowing liquid phase through a small penetration thickness. The CO_2 diffusion profile in liquid phase is shown in Figure 3.1. By applying small penetration experimental set-up, controlling of CO_2 diffusion from gas phase to liquid phase may be occurred.

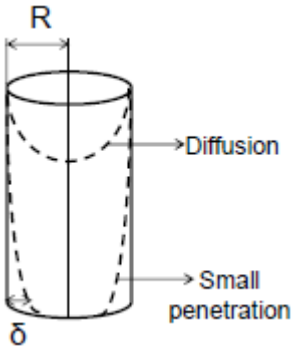

Figure 3.1. CO_2 diffusion profile in liquid phase

Experimental set-up for the small penetration method was shown in Figure 3.2. The experimental apparatus consists of reaction chamber and a stabilization tank. The solution was withdrawn from the stabilization tank by a circulation pump and solution was sent to the reaction chamber where CO_2 gas diffuse into the flowing liquid to certain diameter. Any particle formed at the gas-liquid boundary will flow into the stabilization tank. In the stabilization tank, particles were stirred for suspension and both conductivity and pH were monitored. Samples were withdrawn from the stabilization tank and analyzed at the desired time frames. When pH decrease to 7 or conductivity reduces to about zero, the crystallization was terminated. Particles, then, were separated by centrifugation and analyzed.

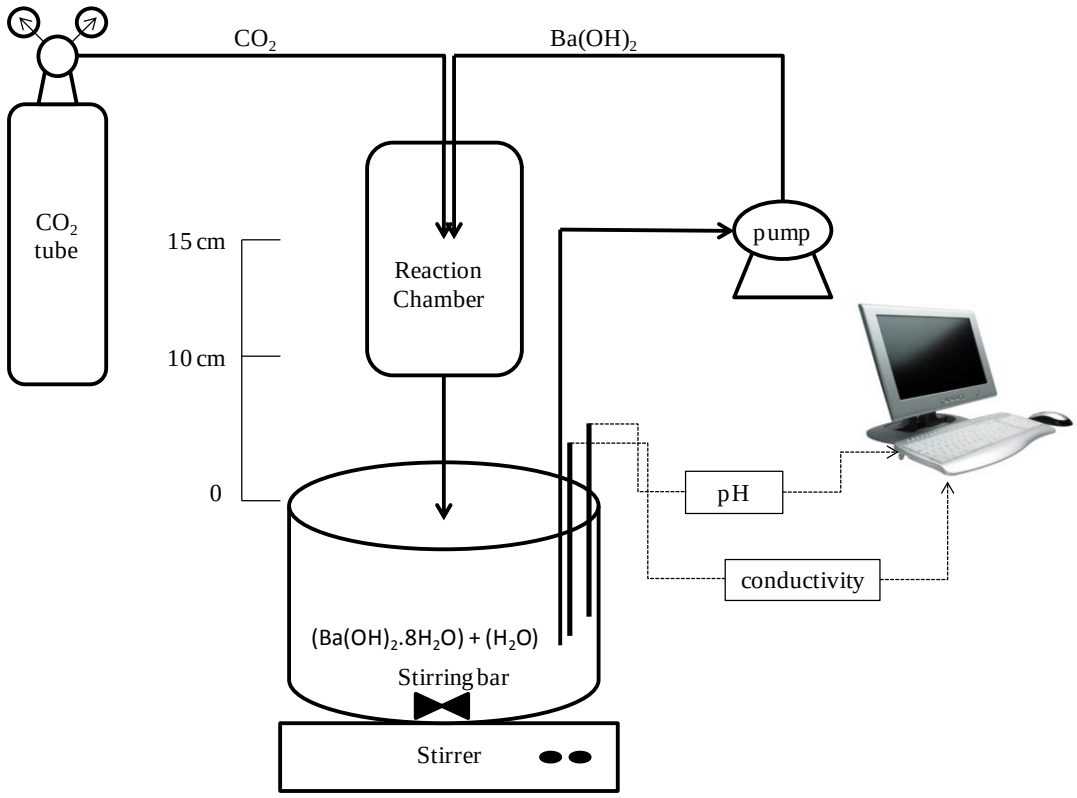

Figure 3.2. Experimental schematic of production of $BaCO_3$

3.2.2. Effect of Concentration of $Ba(OH)_2$ on Production of $BaCO_3$

Effect of different concentration of $Ba(OH)_2.8H_2O$ on production of $BaCO_3$ particles were investigated by using 5-neck jacketed reactor. 5-neck jacketed reactor was shown in Figure 3.3. Firstly, 420 ml of deionized (DI) water was added to the reactor and 190 ml of deionized water was added to pump which was connected to the system. Then desired amount of $Ba(OH)_2.8H_2O$ was added to the reactor. The solution was mixed on a magnetic stirrer. pH and conductivity probes where installed within the reactor by THERMO ORION 5 STAR pH meter were monitored. pH and conductivity probes were calibrated with calibration solutions before each experiments. The $Ba(OH)_2.8H_2O$ solution prepared in the reactor was circulated between the reactor and the mixing chamber by the pump and CO_2 injection was initiated. All data were monitored and recorded with a Star Plus Navigator 21 software program. In this device, data were collected at each 3 seconds.

Figure 3.3. 5-neck jacketed reactor

During the crystallization, 1 ml of solutions was withdrawn from the reactor at indicated times in order to determine the particle shape and size by the SEM analysis. 2 ml of sample was also withdrawn from the reactor at different times in order to determine the crystal structure of produced particles by the XRD analysis. Also, 1 ml of samples was withdrawn from the reactor in order to determine the surface area and porosity of produced $BaCO_3$ particles by the BET analysis. Also, 2 ml of sample was withdrawn from the reactor in order to determine the thermal behavior of produced $BaCO_3$ particles by the TGA and DSC analysis. Totally, four sets of samples were taken at 7 different time frames during the experiment and used for SEM, XRD, BET, TGA and DSC analysis. Then, these different samples were put into the centrifuge for 4 minutes at 7000 rpm (Hettich-Universal 320). The precipitated samples were collected and washed by acetone. Then, the precipitated particles were put into an oven (Nuve-EV 018) under vacuum condition at 110 °C overnight for drying. Then precipitated samples were sent to SEM, XRD, BET, TGA and DSC for their characterizations.

While keeping other parameters constant, concentration of $Ba(OH)_2.8H_2O$ was varied. 30 mM, 60 mM, 80 mM, 100 mM, 150 mM, 250 mM, 300 mM and 400 mM of $Ba(OH)_2.8H_2O$ concentrations were studied for their effect on the particle size and particle morphologies. As the molarity was the investigated parameter, temperature, stirring rate, flow rate of feeding CO_2, liquid flow rate, tank volume and length of reaction chamber were constant. $Ba(OH)_2.8H_2O$ amount in different concentration experiments were given below Table 3.2. Other experimental conditions were listed in Table 3.3.

Table 3.2. Amount of barium hydroxide octahydrate for different concentrations

Concentration (mM)	**Amount of $Ba(OH)_2.8H_2O$ (g)**
30	5.77
60	11.55
80	15.39
100	19.24
150	28.86
250	48.11
300	57.73
400	76.97

Table 3.3. Experimental conditions as different concentration of barium hydroxide octahydrate values

Parameter	**Value**
Temperature	25°C
Stirring rate	900 rpm
Flow rate of CO_2	16 ml/s
Flow rate of liquid	80 ml/s
Total Volume	610 ml
Length of reaction chamber	15 cm

3.2.2.1. Solubility of Barium Hydroxide Octahydrate ($Ba(OH)_2.8H_2O$)

Solubility of $Ba(OH)_2.8H_2O$ in water is an important parameter. Given solubility values of $Ba(OH)_2.8H_2O$ in water at different temperatures are shown Table 3.4 at 1 atmosphere pressure. Solubility is given of grams per 100 ml of water. According to this table, solubility of $Ba(OH)_2.8H_2O$ in water was calculated at 25°C to be 4.74 g/100 ml water by interpolation. The solubility of $Ba(OH)_2.8H_2O$ was estimated by measuring the conductivity values at different $Ba(OH)_2.8H_2O$ concentrations.

Table 3.4. Solubility values of barium hydroxide octahydrate in water at different temperatures (Source: https://en.wikipedia.org/wiki/Solubility_table)

Temperature	0°C	10°C	20°C	30°C	40°C	50°C	60°C	80°C
Solubility of $Ba(OH)_2.8H_2O$	1.67	2.48	3.89	5.59	8.22	11.7	20.9	101

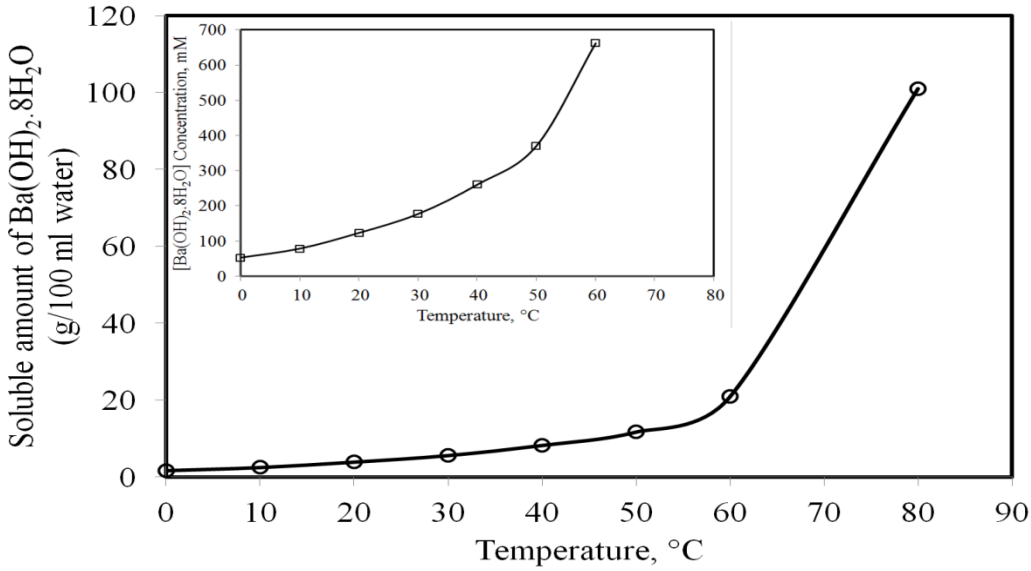

Figure 3.4. Soluble amount of $Ba(OH)_2.8H_2O$ in 100 ml water vs. Temperature

Figure 3.4 shows the solubility of $Ba(OH)_2.8H_2O$ at different temperatures. As shown in the figure, the solubility of $Ba(OH)_2.8H_2O$ increases with temperature. When temperature was greater than 60°C, the solubility of $Ba(OH)_2.8H_2O$ increases sharply. At room temperature, the solubility of $Ba(OH)_2.8H_2O$ was about 150 mM.

3.2.3. Effect of CO_2 Flow Rate on $BaCO_3$ Production

Effect of CO_2 flow rate on particle size and shape of $BaCO_3$ particles was investigated. The CO_2 flow rates were chosen to be 4, 12 and 16 ml/s was studied with the system. Other experimental conditions were constant and listed in Table 3.5.

Table 3.5. Experimental conditions as different CO_2 flow rate

Parameter	Value
Stirring rate	900 rpm
Tank Volume	610 ml
Flow rate of liquid	80 ml/s
Concentration of $Ba(OH)_2.8H_2O$	100 mM
Temperature	25°C
Length of reaction chamber	15 cm

3.2.4. Effect of Length in Reaction Chamber

Effect of length in reaction chamber on particle size and shape of $BaCO_3$ particles was investigated. The lengths in the reaction chamber were chosen to be 10 and 15 cm studied in the system. Other experimental conditions were constant as listed in Table 3.6.

Table 3.6. Experimental conditions as different length of reaction chamber

Parameter	**Value**
Stirring rate	900 rpm
Tank Volume	610 ml
Flow rate of liquid	80 ml/s
CO_2 flow rate	16 ml/s
Concentration of $Ba(OH)_2.8H_2O$	100 mM
Temperature	25°C

3.2.5. Effect of Stirring Rate on $BaCO_3$ Production

Effect of stirring rate on particle size and shape of $BaCO_3$ particles was investigated. The stirring rates were chosen to be 600 and 900 rpm studied in the system. Other experimental conditions were constant as listed in Table 3.7.

Table 3.7. Experimental conditions as different stirring rate

Parameter	**Value**
Concentration of $Ba(OH)_2.8H_2O$	100 mM
Tank Volume	610 ml
Flow rate of liquid	80 ml/s
CO_2 flow rate	16 ml/s
Temperature	25°C
Length of reaction chamber	15 cm

3.2.6. $BaCO_3$ Synthesis by Bubbled Stirred Tank Reactor

Bubbled stirred tank reactor was studied for the nano $BaCO_3$ synthesis as shown in Figure 3.5. A circular pipe with holes was placed into stirred tank at two levels; one is at bottom and one is at top as shown in the figure. Firstly, 3.5 L of DI water was added to the reactor and stirred at 600 rpm. pH and conductivity probes were placed into the reactor and connected to a computer by the THERMO ORION 5 STAR pH meter. All data were monitored and recorded with a Star Plus Navigator 21 software program. Data were collected at each 3 seconds time intervals. Then, 110.42 g of $Ba(OH)_2.8H_2O$ solution was added to prepare 100 mM of $Ba(OH)_2.8H_2O$ solution. Star plus navigator software program was started to measure conductivity and pH values. After $Ba(OH)_2.8H_2O$ was dissolved in water completely, CO_2 gas was supplied from the CO_2 glister as soon as CO_2 was bubbled and crystallization has initiated.

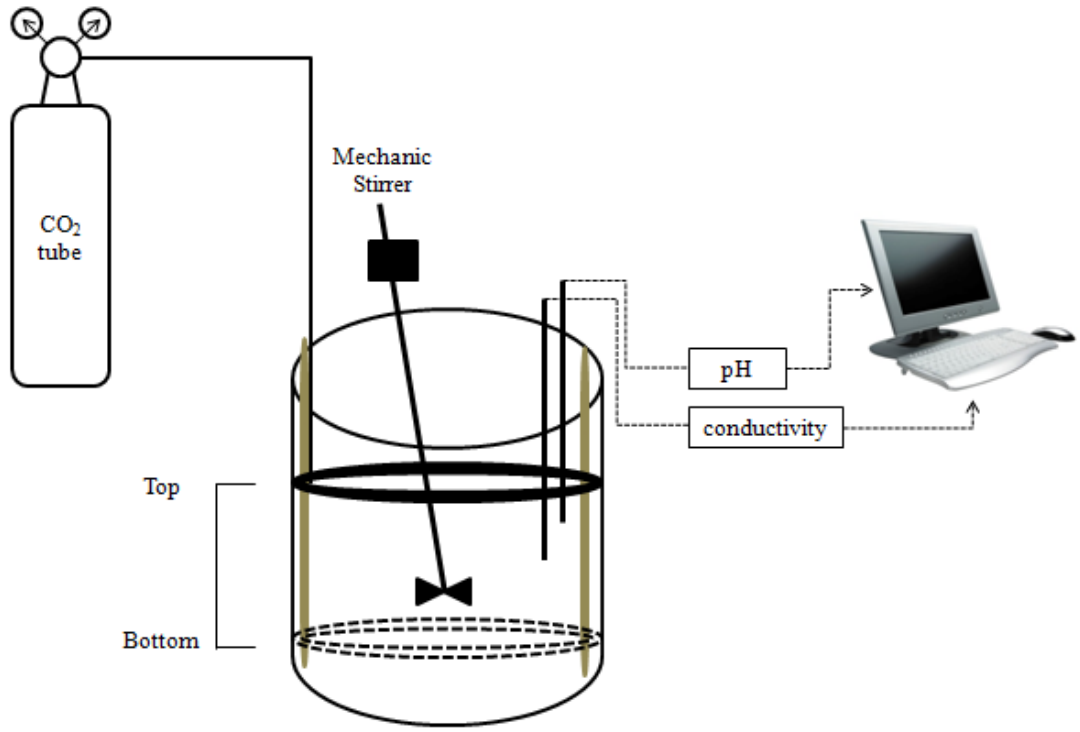

Figure 3.5. Experimental set-up of partially bubbled stirred tank reactor with CO_2 injection by rubber hose with holes

The only parameter to study was the position of rubber hose with holes while others were stayed constant. The other parameters were listed in Table 3.8.

Table 3.8. Experimental conditions for different position of rubber hose with holes

Parameter	Value
Concentration of $Ba(OH)_2.8H_2O$	100 mM
Tank Volume	3.5 L
CO_2 flow rate	12 ml/s
Stirring rate	600 rpm
Pressure of gas tube	5 bar
Temperature	25°C

1 ml of solutions was withdrawn from the reactor at the indicated time frames in order to determine the particle size and morphology by the SEM analysis during the reaction. 2 ml of sample was withdrawn from the reactor at different times in order to determine the crystal structure of produced particles by XRD analysis. Totally, 7 samples in two sets which were used for SEM and XRD were taken from the system during the experiments at different times into eppendorf tubes. Then, these different samples were put into the centrifuge for 4 minutes at 7000 rpm (Hettich-Universal 320). The precipitated samples were collected and washed by acetone. Then, the precipitated particles were put into an oven (Nuve-EV 018) under vacuum condition at 110 °C overnight for drying. Lastly precipitated samples were sent to SEM and XRD for the characterization of them.

3.3. Characterization of Particles

3.3.1. Scanning Electron Microscopy (SEM) Analysis

Scanning Electron Microscope (SEM) is a beam of high energy electron to generate a variety of signals at the surface of solid specimen. SEM analysis gives information about particle morphology and sizes. SEM was used by signals deriving from electron sample interactions. The SEM analysis was applied in order to investigate surface morphology and particle size of $BaCO_3$ samples. As shown in Figure 3.6, all of barium carbonate particles were coated at a current of 15 mA under vacuum of $6x10^{-2}$ mbar during 90 seconds with gold on copper sample stubs with conducting carbon tape by Sputter Coater which was the model of Emitech K550X before the SEM analysis.

Figure 3.6. Gold Coating of $BaCO_3$ samples (Source: http://mam.iyte.edu.tr/)

Figure 3.7 shows the Quanta and Philips devices used for SEM analysis. Philips XL 30S FEG was operating at an accelerated voltage of 3 kV and spot of 2.0. FEI QUANTA 250 FEG was operating at an accelerated voltage of 5 kV and spot of 3.0.

Figure 3.7. Philips XL 30S FEG (Source: http://mam.iyte.edu.tr/)

3.3.2. X-Ray Diffraction (XRD) Analysis

Figure 3.8 shows the X-Ray Diffraction measurements conducted by using Philips X'Pert Pro X-ray Diffractometer. The crystal structure was determined by using Cu-Kα radiation with 40 mA and 45 kV. The diffraction pattern was recorded for 2Θ

degree in the range between 10° and 80° and speed of scan was standard as 0.139 °/sec. Identification of $BaCO_3$ crystals was done by Search Match Computerized Technique.

Figure 3.8. Philips X'Pert Pro X-ray Diffractometer (Source: http://mam.iyte.edu.tr/)

CHAPTER 4

RESULTS AND DISCUSSION

4.1. Effect of $Ba(OH)_2.8H_2O$ Concentration on $BaCO_3$ Production

Effect of $Ba(OH)_2.8H_2O$ concentration on the crystallization of $BaCO_3$ was studied. Different $Ba(OH)_2.8H_2O$ concentrations with deionized water from 30 mM to 400 mM were prepared. Effect of $Ba(OH)_2.8H_2O$ concentration on morphology and sizes of $BaCO_3$ particles were determined by keeping other experimental parameters constant. Figure 4.1 shows the changes in conductivity with time for different $Ba(OH)_2.8H_2O$ concentrations during $BaCO_3$ crystallization. Before CO_2 injection, there was a slightly increase in conductivity by dissolving $Ba(OH)_2.8H_2O$. Increasing in conductivity was mostly related to the presence of Ba^{++} ions from the dissolved $Ba(OH)_2.8H_2O$. The constant conductivity indicated that $Ba(OH)_2.8H_2O$ was dissolved completely. Both pump for liquid circulation and CO_2 injection were started in order to initiate $BaCO_3$ crystallization. In this case, a decrease in conductivity was observed. The initial $Ba(OH)_2.8H_2O$ concentration was calculated according to 610 ml of DI water. 420 ml of DI water was present in the reactor. Additional 190 ml of DI water was present in the pump. By the start of CO_2 injection and pump, DI water in the pump was mixed with the dissolved $Ba(OH)_2.8H_2O$ which caused a sudden decrease in conductivity resulting in the dilution of solution. After CO_2 injection, conductivity values decreased almost linearly for $Ba(OH)_2.8H_2O$ concentrations greater than 250 mM, conductivity started to decrease almost linearly. $BaCO_3$ particles were started to appear. By CO_2 injection, CO_2 was started to transform from gas phase to liquid phase and conductivity values decreased as a result of decrease in the metal ions as CO_3^{2-} ions were precipitated with Ba^{++} ions. There was a turning point about zero conductivity values where conductivity increases slightly. This turning point shows that all the dissolved $Ba(OH)_2.8H_2O$ reacted with CO_2, and $BaCO_3$ particles were produced completely. The increase in the conductivity could be related to the increase in charged species due to the CO_2 dissolution as well as Ba^{++} ions as a result of the redissolution of $BaCO_3$. For higher concentrations of $Ba(OH)_2.8H_2O$, conductivity increased after CO_2

injection. The fact that $Ba(OH)_2.8H_2O$ can not dissolve completely at higher concentrations since solubility limit of $Ba(OH)_2.8H_2O$ was reported to be 4.74 g/100 ml of water or about 150 mM at 25°C. Above the 150 mM of $Ba(OH)_2.8H_2O$ concentrations, it seems that the dissolved $Ba(OH)_2.8H_2O$ was consumed upon CO_2 injection and during this time a sudden dissolution of $Ba(OH)_2.8H_2O$ would increase the conductivity of the solution. Upon consumption of the ions in solution, the conductivity values were seemed to decrease almost linearly. The linear decrease in conductivity also indicated that CO_2 dissolution rate was also constant throughout the $BaCO_3$ crystallization.

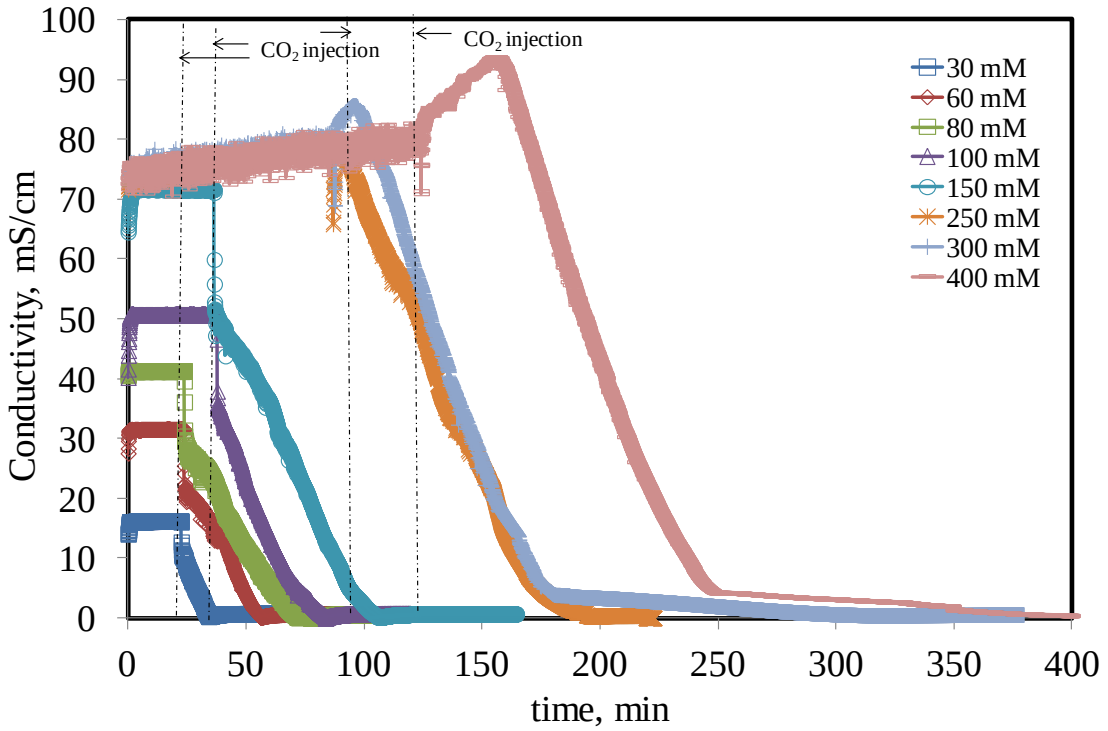

Figure 4.1. Conductivity values during $BaCO_3$ crystallization at different $Ba(OH)_2.8H_2O$ concentrations

Figure 4.2 shows the change in pH at different $Ba(OH)_2.8H_2O$ concentrations with time during $BaCO_3$ crystallization. As can be seen in the figure, pH increased by dissolving the $Ba(OH)_2.8H_2O$ before the CO_2 injection. After completely dissolution of $Ba(OH)_2.8H_2O$, pH values remained constant. When CO_2 injection was started, pH values started to decrease first slowly and, to the end, pH values showed sharp decrease

and then stayed almost unchanged. According to these two figures, crystallization time was shorter with decreasing $Ba(OH)_2.8H_2O$ concentration.

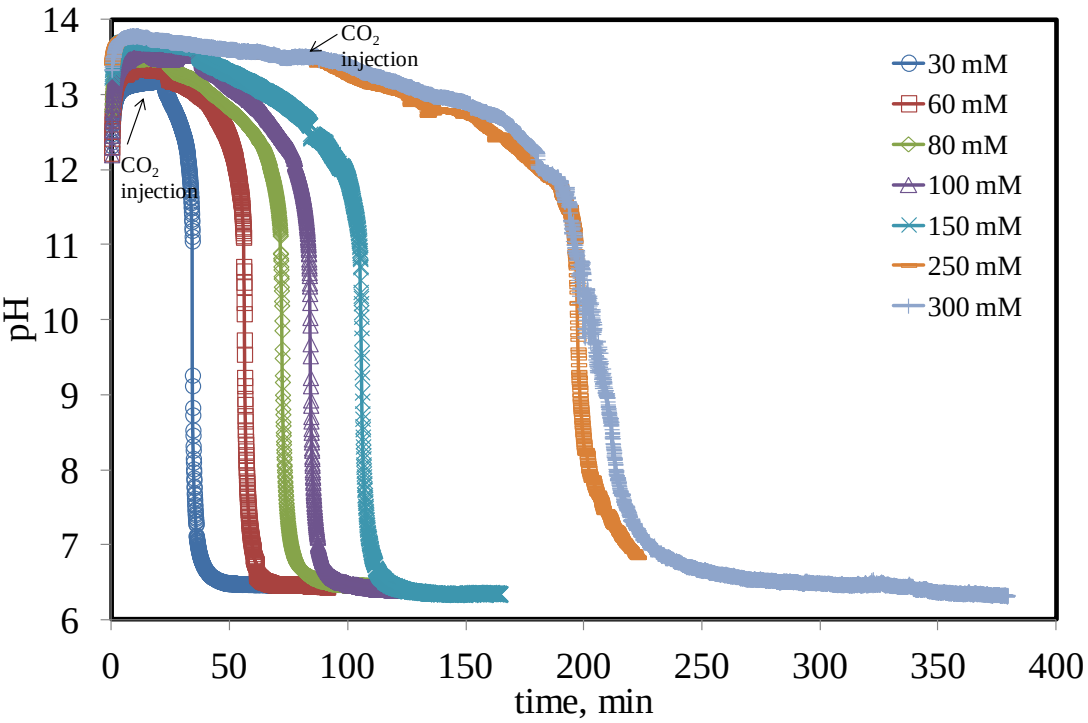

Figure 4.2. pH values during $BaCO_3$ crystallization at different $Ba(OH)_2.8H_2O$ concentrations

The conductivity values at which $Ba(OH)_2.8H_2O$ was completely dissolved for different $Ba(OH)_2.8H_2O$ concentrations were plotted as shown in Figure 4.3. As shown in the figure, there was a linear increase in conductivity up to 150 mM and above the 150 mM, the conductivity values stayed almost unchanged. 150 mM is the solubility limit for $Ba(OH)_2.8H_2O$. Significant amount of $Ba(OH)_2.8H_2O$ remained undissolved in water above the solubility limit. Up to the solubility limit of 150 mM of $Ba(OH)_2.8H_2O$ at 25°C, the conductivity values are linearly related to the $Ba(OH)_2.8H_2O$ concentration with a slope of 0.3603.

$$Conductivity = 0.3603 * [Ba(OH)_2.8H_2O] \quad (4.1)$$

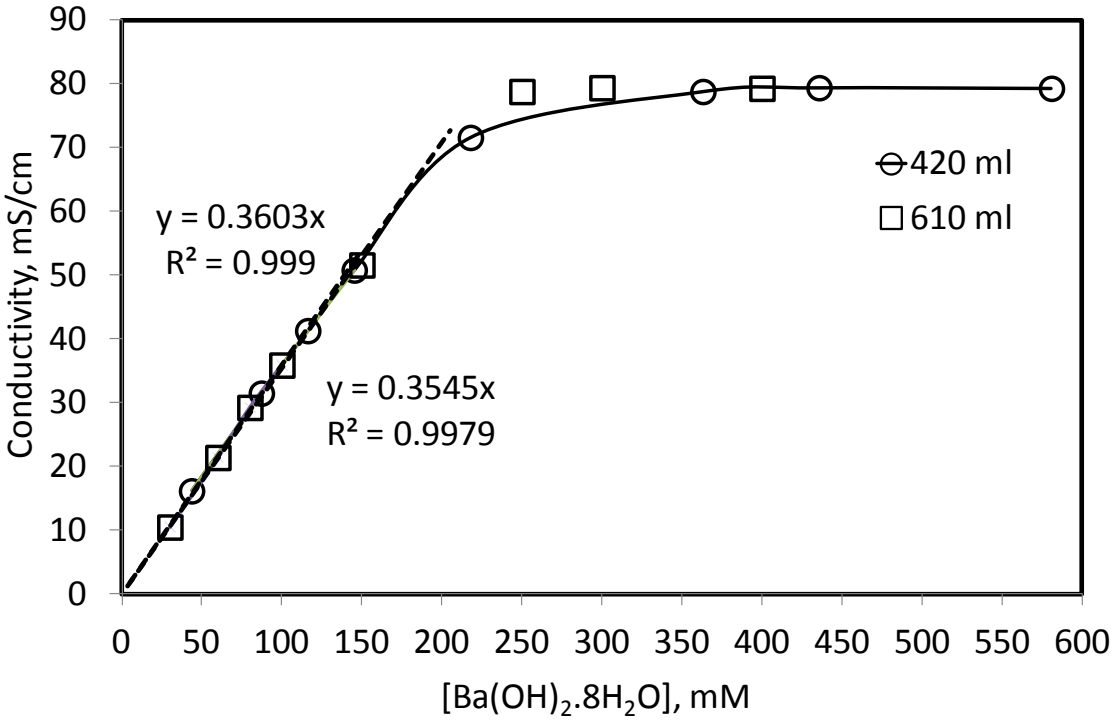

Figure 4.3. Conductivity values at which $Ba(OH)_2.8H_2O$ was completely dissolved at different $Ba(OH)_2.8H_2O$ concentrations

The linear change in conductivity by $Ba(OH)_2.8H_2O$ concentration up to the solubility limit of $Ba(OH)_2.8H_2O$ could be related to Ba^{++} ion concentration. Because 1 mol of Ba^{++} ions was formed from the dissolution of 1 mol of $Ba(OH)_2.8H_2O$. Concentration of Ba^{++} ion in $Ba(OH)_2.8H_2O$ solution can be calculated according to Eq. (4.2).

$$[Ba^{++}] = (Conductivity) * \left(\frac{1}{slope}\right) \quad (4.2)$$

Figure 4.4 shows the calculated Ba^{++} ion concentrations for all $Ba(OH)_2.8H_2O$ solutions studied from Eq. (4.2). As shown in the figure, the initial Ba^{++} ion concentrations calculated were always greater than the indicated values due to the dissolution of these powders in 420 ml of DI water in the stabilization tank. As soon as the pump was started, the concentration was decreased to the indicated values as a result of dilution of $Ba(OH)_2.8H_2O$ solution with the DI water placed within the pump. When CO_2 was injected, the Ba^{++} ion concentrations started to decrease almost linearly

indicating that both the CO_2 dissolution rates and $BaCO_3$ crystallization rates are almost constant and equal to each other.

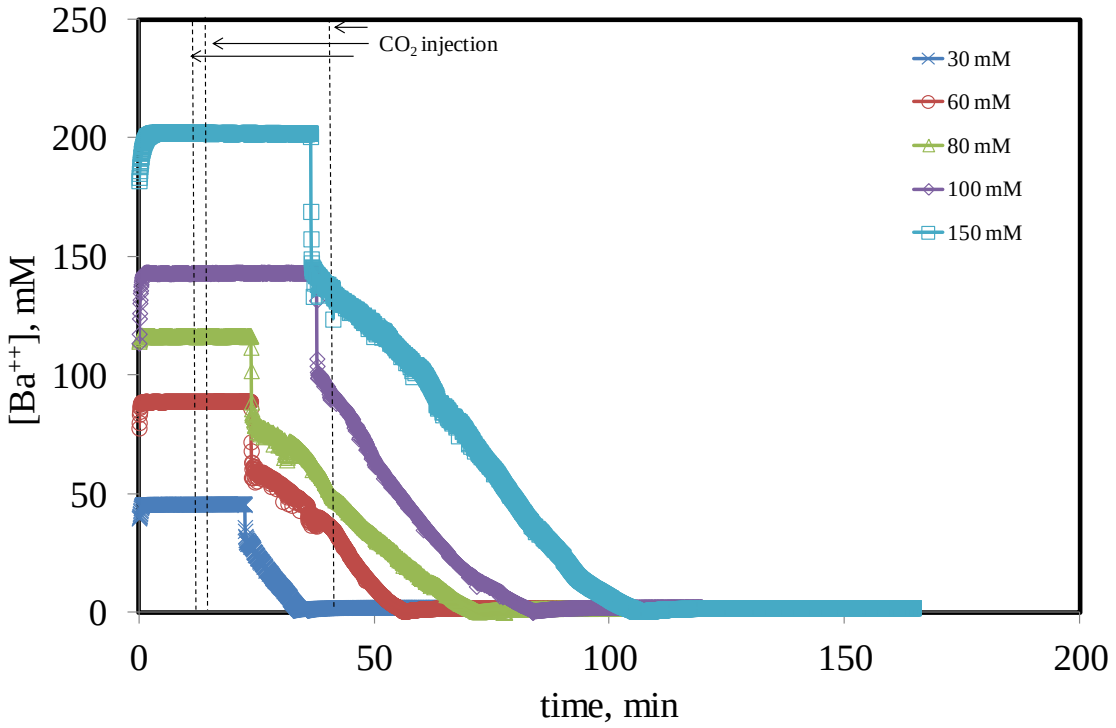

Figure 4.4. Calculated Ba^{++} ion concentrations during $BaCO_3$ crystallization at different $Ba(OH)_2.8H_2O$ solutions

The OH^- ion concentrations from the pH of the $Ba(OH)_2.8H_2O$ solutions can be calculated according to Eq. (4.3).

$$[OH^-] = 10^{(-(14-pH))} \tag{4.3}$$

The OH^- ion concentrations for $Ba(OH)_2.8H_2O$ concentration up to 150 mM experiments were calculated according to Eq. (4.3). Figure 4.5 shows the calculated OH^- ion concentrations with time during $BaCO_3$ crystallization. Similar trend was seen with the changes in Ba^{++} ion concentrations. That was, the OH^- ion concentration was higher than the indicated values due to water content in the stabilization tank and OH^- ion concentrations were decreased when the waters in the pump were added to the tank to the indicated values. However, the fluctuation in OH^- ion concentrations was more significant compared to Ba^{++} ion concentrations.

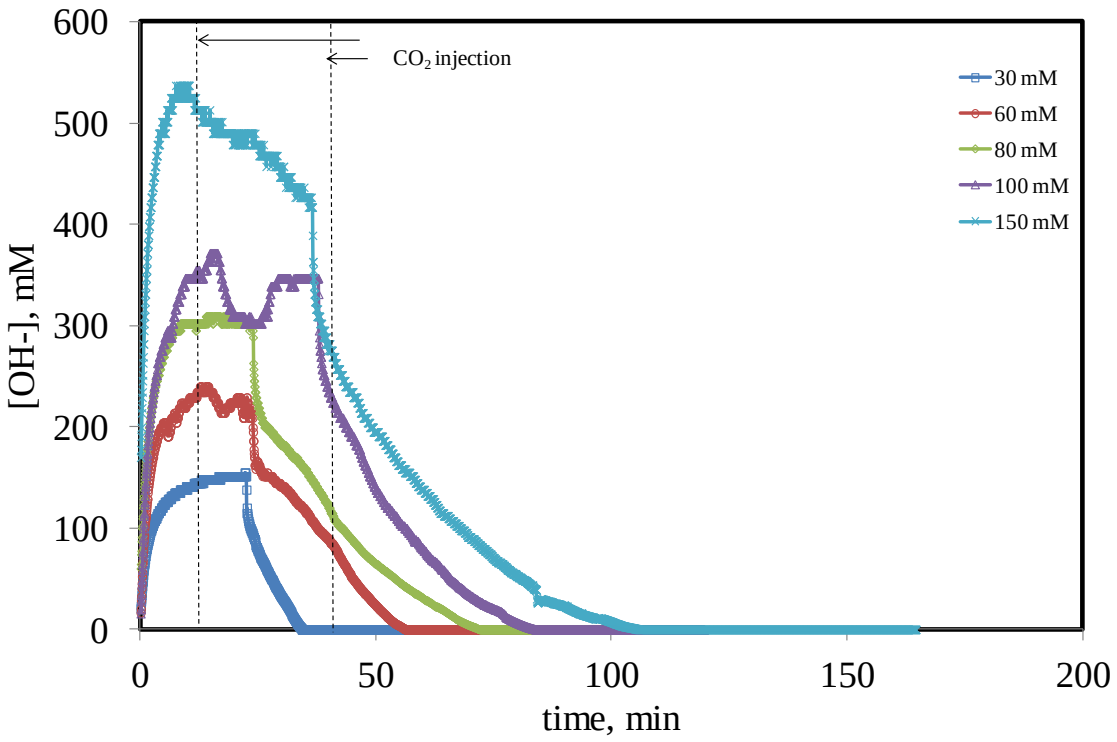

Figure 4.5. Calculated OH^- ion concentrations during $BaCO_3$ crystallization at different $Ba(OH)_2.8H_2O$ concentrations

Figure 4.6 shows the change in Ba^{++} and OH^- ion concentrations at different $Ba(OH)_2.8H_2O$ concentrations. As shown in the figure, the OH^- ion concentration almost two times bigger than the Ba^{++} ion concentrations which was the stoichiometric value for the $Ba(OH)_2.8H_2O$ solutions. There was a linear increase in Ba^{++} and OH^- ion concentrations up to 150 mM. For Ba^{++} ion concentrations, above the solubility limit, there was no change. The calculated OH^- ion concentrations decreased at higher concentrations, higher than the solubility limit of 150 mM, there would be some charged species such as $BaOH^+$, $BaHCO_3^+$ which did not change the conductivity but reduces the pH values.

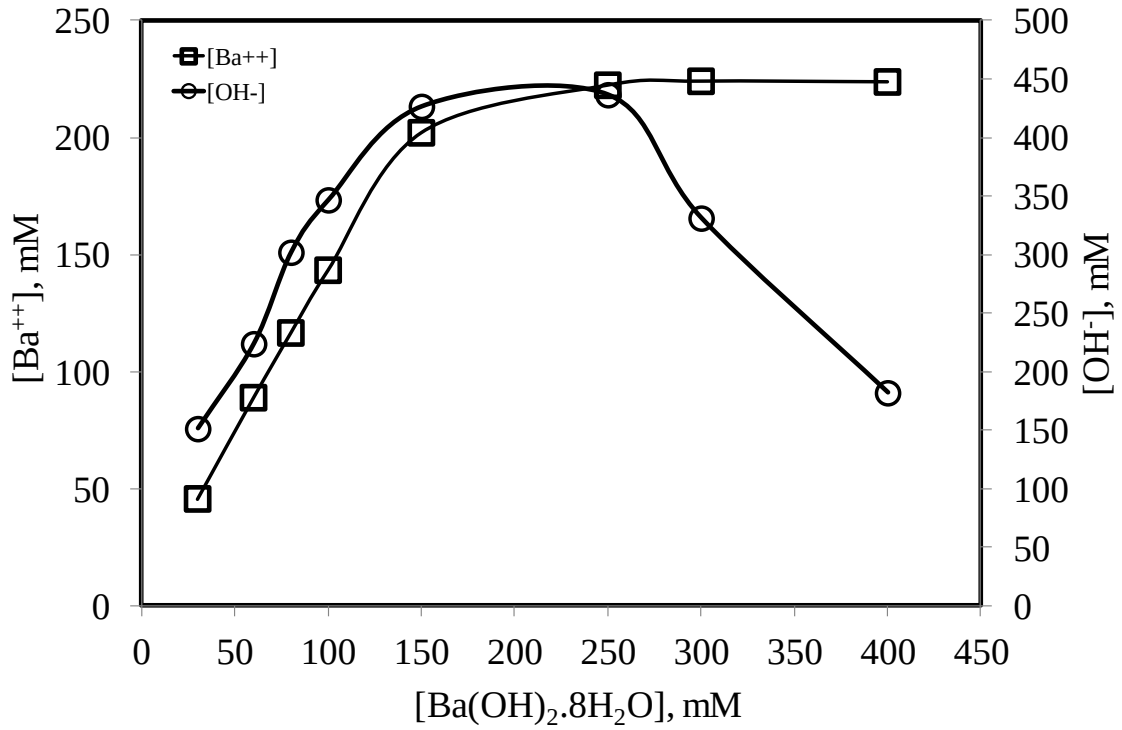

Figure 4.6. Calculated Ba^{++} and OH^- ion concentrations at different $Ba(OH)_2.8H_2O$ concentrations

Preparation of $Ba(OH)_2.8H_2O$ in 420 ml of stabilization tank resulted in a higher concentration, *C*. Addition of 190 ml of water within the pump resulted in a decrease in concentration, C_0. CO_2 was also injected at the same time when the pump was operated. A mathematical approximation was applied whether the CO_2 injection, and therefore, the $BaCO_3$ crystallization affected the conductivity measurements. As can be seen from Eqn. 4.4 to Eqn. 4.10, the decrease in concentration would be linearly related to the final concentration of the $Ba(OH)_2.8H_2O$ solution prepared.

$$\Delta C = C_0 - C \tag{4.4}$$

$$C_0 * V_1 = C * (V_1 + V) \tag{4.5}$$

$$C = C_0 * \left(\frac{V_1}{V + V_1}\right) = C_0 * \left(\frac{420\ ml}{(420 + 190) ml}\right) \tag{4.6}$$

$$C = 0.69 * C_0 \tag{4.7}$$

$$\Delta C = C_0 - (0.69 * C_0) \tag{4.8}$$

$$\Delta C = C_0(1 - 0.69) \tag{4.9}$$

$$\Delta C = 0.31 * C_0 \tag{4.10}$$

The difference in measured conductivity values at different $Ba(OH)_2.8H_2O$ concentrations was shown in Figure 4.7. As can be seen in the figure, there was a linear relationship between the difference and $Ba(OH)_2.8H_2O$ concentration with a slope of 0.2864 close to 0.31. This indicate that although the difference was very small, injection of CO_2 influenced very little at the beginning of the crystallization since only small amount of $BaCO_3$ converted initially.

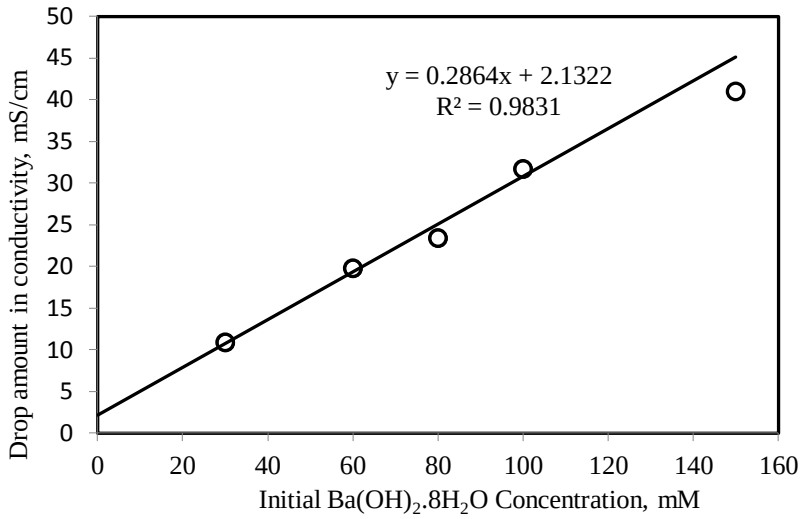

Figure 4.7. Drop in concentration upon addition of water in the pump for different $Ba(OH)_2.8H_2O$ concentrations

Figure 4.8 shows the change in pH and conductivity values for 80 mM of $Ba(OH)_2.8H_2O$ concentration during $BaCO_3$ crystallization. As shown in the figure, a sudden decrease upon CO_2 injection was due to the decrease in $Ba(OH)_2.8H_2O$ concentration as a result of mixing of water in the circulating pump into the solution in the stabilization tank. The effect of CO_2 injection was shown as a steady decrease in conductivity values. pH values were always greater than 12 during $BaCO_3$ crystallization, however, to the end, a sudden decrease in pH was seen. The numbers indicated in the figure showed the samples taken during the crystallization.

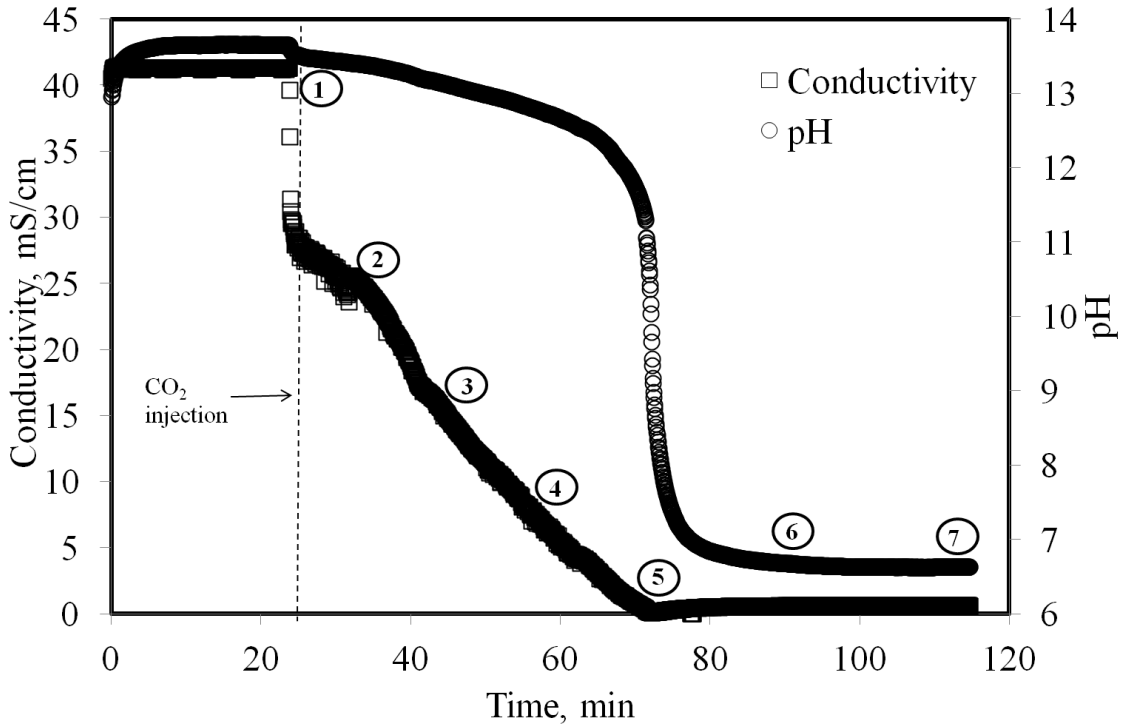

Figure 4.8. pH and conductivity values for 80 mM $Ba(OH)_2.8H_2O$ concentration during $BaCO_3$ crystallization

Figure 4.9 shows the SEM images of $BaCO_3$ particles produced in 30 mM of $Ba(OH)_2.8H_2O$ concentrations. As shown in the figure, first sample was particles obtained from the dissolved $Ba(OH)_2.8H_2O$ solution before the CO_2 injection. These particles must be $BaCO_3$ particles as the impurity in the $Ba(OH)_2.8H_2O$ solution. When CO_2 was injected, $BaCO_3$ particles were synthesized (sample 2). As crystallization progressed, particles started to grow along their length (sample 3 and sample 4). As all Ba^{++} ions were consumed, particles were seen to dissolve and their length became shorter (sample 5). Upon further CO_2 injection, particles started to grow again along their length and diameter through dissolution-recrystallization mechanism (sample 6 and sample 7).

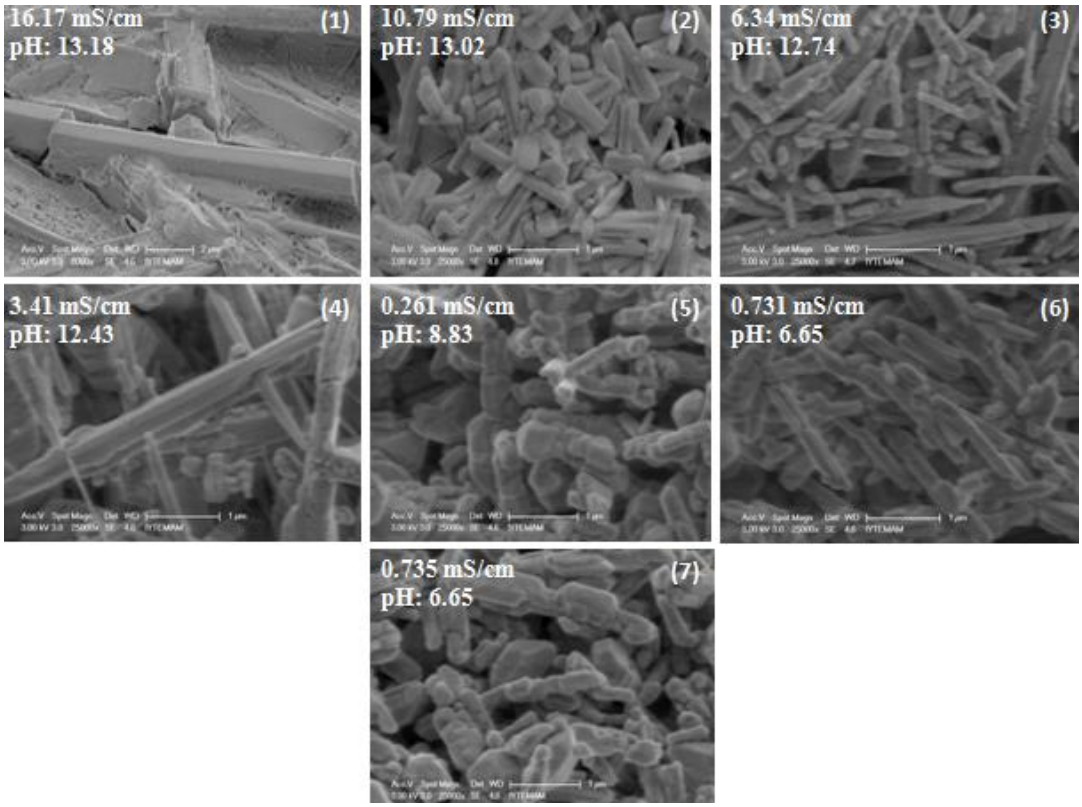

Figure 4.9. SEM images of $BaCO_3$ particles produced in 30 mM of $Ba(OH)_2.8H_2O$ solution

Figure 4.10 shows the SEM images of $BaCO_3$ particles produced in 60 mM of $Ba(OH)_2.8H_2O$ concentration. As shown in this figure, there was small amount of $Ba(OH)_2.8H_2O$ at the beginning of the experiment, then rod-like $BaCO_3$ particles started to produce but not by homogeneous size and shape distribution. Besides existing of rod-like morphology, less amount of pencil-like morphology was observed. Despite of small particles were observed at the early stages of crystallization, $BaCO_3$ particles became larger through the end stages of crystallization.

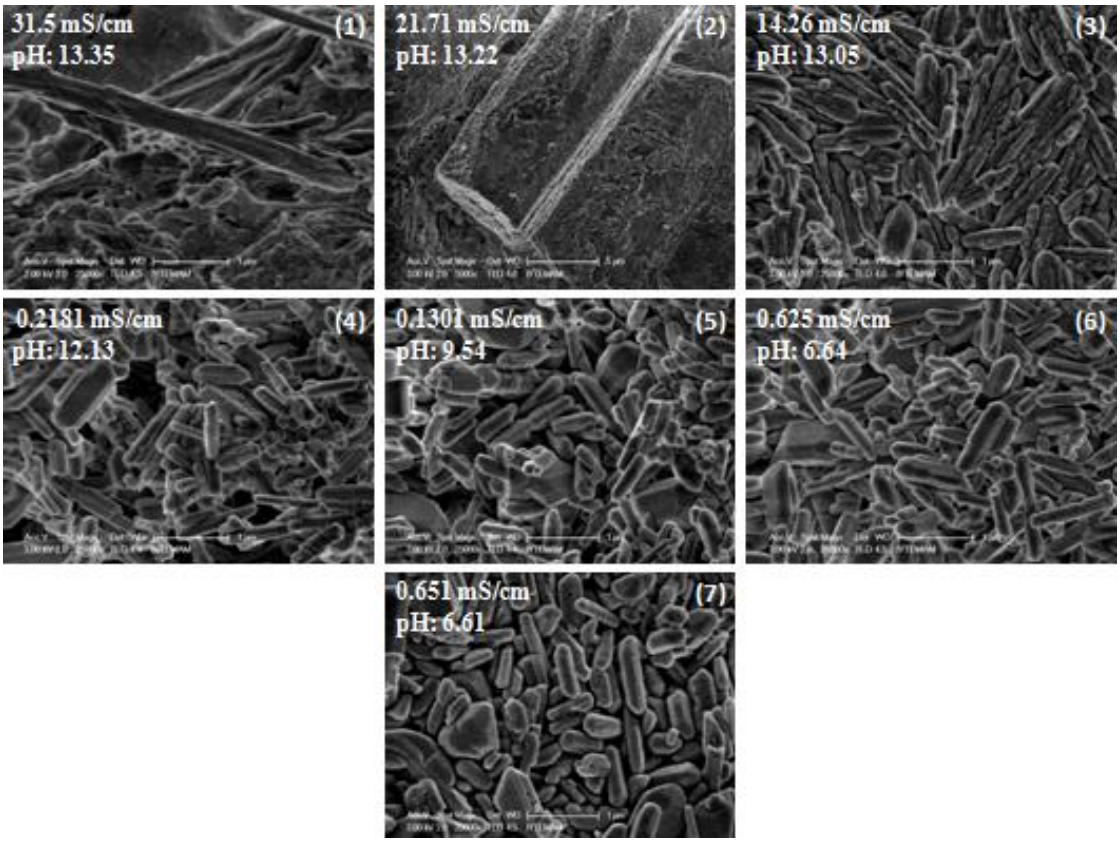

Figure 4.10. SEM images of $BaCO_3$ particles produced in 60 mM of $Ba(OH)_2.8H_2O$ solution

Figure 4.11 shows the SEM images of $BaCO_3$ particles produced in 80 mM of $Ba(OH)_2.8H_2O$ concentration. According to this figure, rod-like shaped $BaCO_3$ particles were produced with almost homogeneous particle size distribution. At early stages of crystallization, longer particles were produced. Then, particles started to become smaller length-wise and diameter-wise. After the turning point or consumption of Ba^{++} ions, particles became larger their both length and diameter through the end of crystallization.

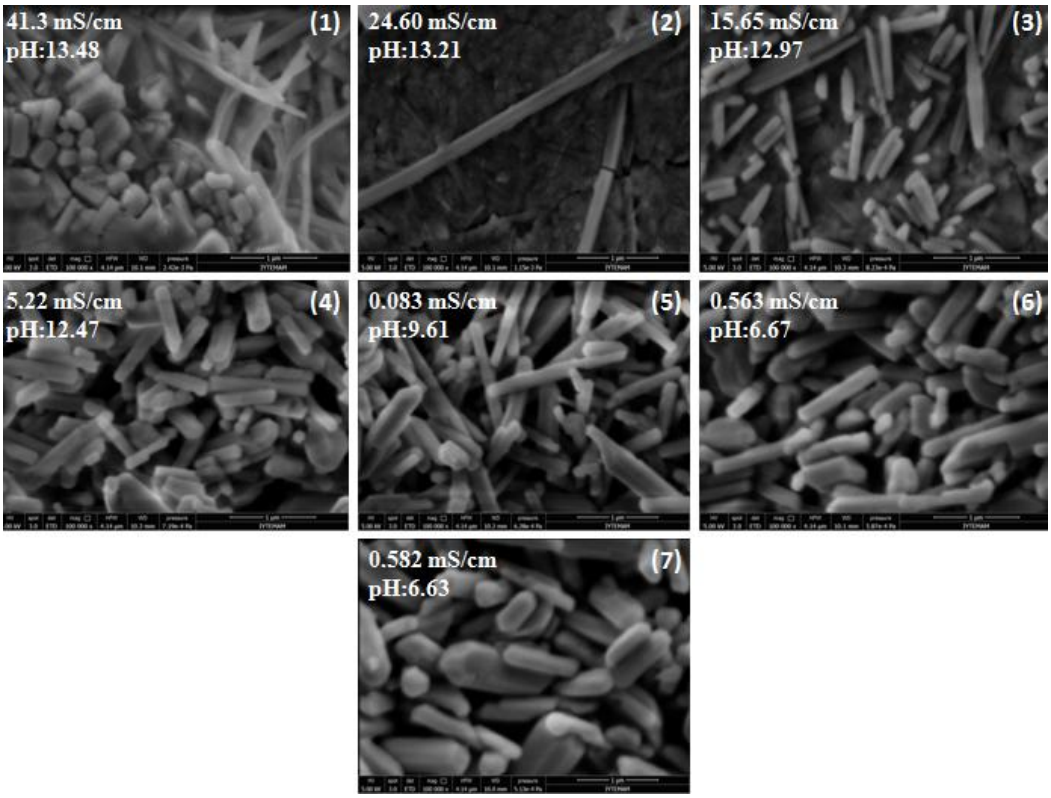

Figure 4.11. SEM images of $BaCO_3$ particles produced in 80 mM of $Ba(OH)_2.8H_2O$ solution

SEM images of 100 mM of $BaCO_3$ particles produced in $Ba(OH)_2.8H_2O$ concentration were shown in Figure 4.12. Similar trend was observed, that is, rod-like $BaCO_3$ particles were produced initially. Their lengths and their diameters decreased due to their dissolution. When Ba^{++} ion depleted in the solution, these particles were seen to grow on their lengths and diameters by recrystallization mechanism.

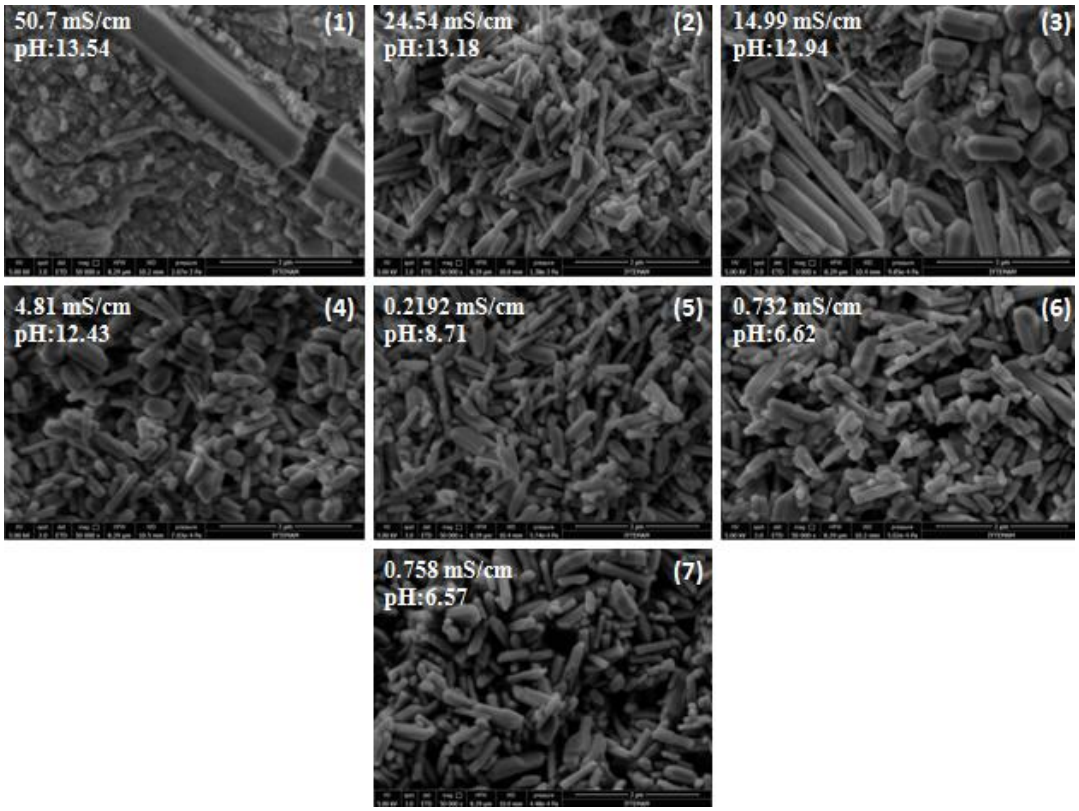

Figure 4.12. SEM images of $BaCO_3$ particles produced in 100 mM of $Ba(OH)_2.8H_2O$ solution

SEM images of 150 mM of $BaCO_3$ particles produced in $Ba(OH)_2.8H_2O$ concentration were shown in Figure 4.13. This concentration was the solubility limit for the $Ba(OH)_2.8H_2O$. As shown in the figure, rod-like and pencil-like morphology were observed. Rod-like $BaCO_3$ particles were produced at the early stages of crystallization. Some of rod-like $BaCO_3$ particles converted into the pencil-like morphology through the end of crystallization. Generally rod-like morphology of $BaCO_3$ particles was dominant in the system. Particle sizes increased to the end of crystallization.

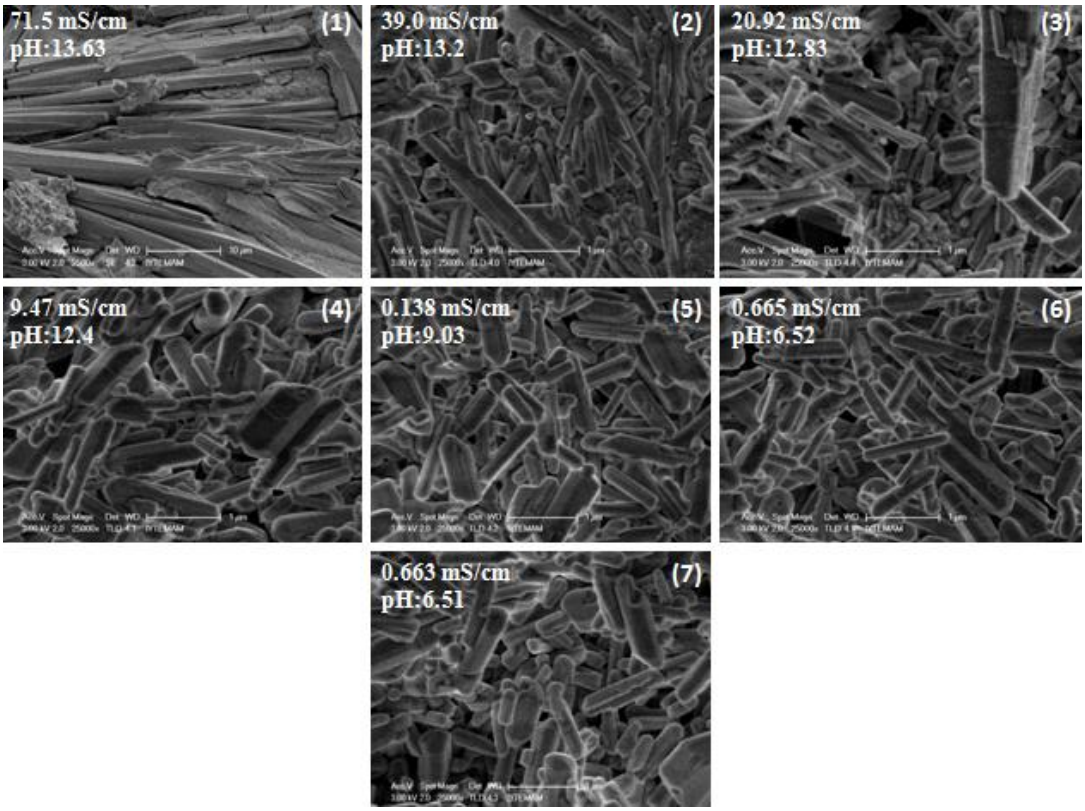

Figure 4.13. SEM images of $BaCO_3$ particles produced in 150 mM of $Ba(OH)_2.8H_2O$ solution

Figure 4.14 shows the SEM images of $BaCO_3$ particles produced in 250 mM of $Ba(OH)_2.8H_2O$ slurry. It was called as 'slurry' because the solubility limit was about 150 mM and it was certain $Ba(OH)_2.8H_2O$ of 250 mM did not dissolve completely. As can be seen in the figure, there were $Ba(OH)_2.8H_2O$ particles present besides the impurity of $BaCO_3$ particles in the solution before CO_2 injection and at the beginning of the crystallization. Rod-like morphology was observed at the early stages of crystallization. Rod-like particles converted into pencil-like particles through the end stages of crystallization. $Ba(OH)_2.8H_2O$ particles were observed in samples due to existence of undissolved $Ba(OH)_2.8H_2O$. Therefore, homogeneous particle size and morphological distributions were not observed. Also, agglomeration of particles occurred. As there were larger particles probably due to impurity, at the beginning of experiment, smaller particles were observed at the early stages of crystallization. The particles became larger through the end of crystallization.

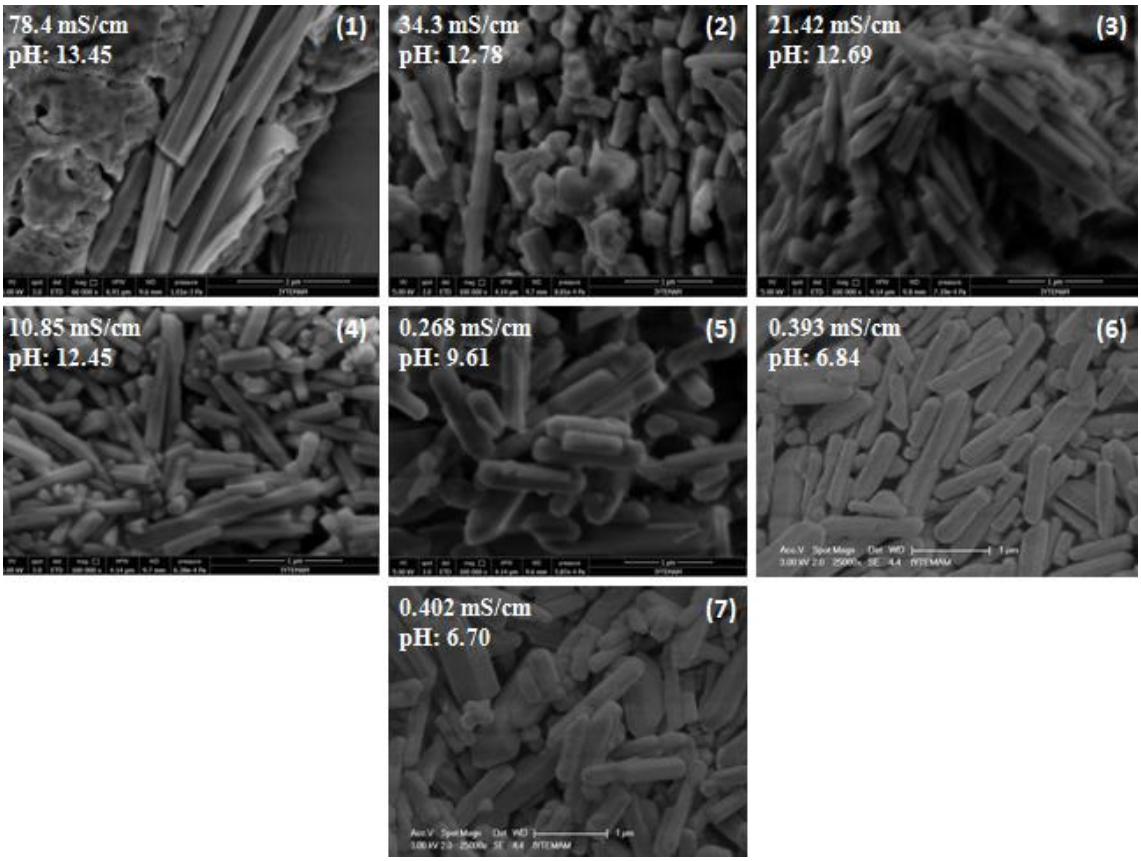

Figure 4.14. SEM images of $BaCO_3$ particles produced in 250 mM of $Ba(OH)_2.8H_2O$ solution

Figure 4.15 shows the SEM images of $BaCO_3$ particles produced in 300 mM of $Ba(OH)_2.8H_2O$ slurry. Similar trend were seen for the higher concentrations of $Ba(OH)_2.8H_2O$, higher than the solubility limit. As shown in this figure, rod-like $BaCO_3$ particles were observed at the early stages of crystallization. Pencil-like morphology was also started to appear through the end of crystallization. Particle sizes were increased through the crystallization. Also, $Ba(OH)_2.8H_2O$ particles were observed in samples due to existence of undissolved $Ba(OH)_2.8H_2O$ in the slurry.

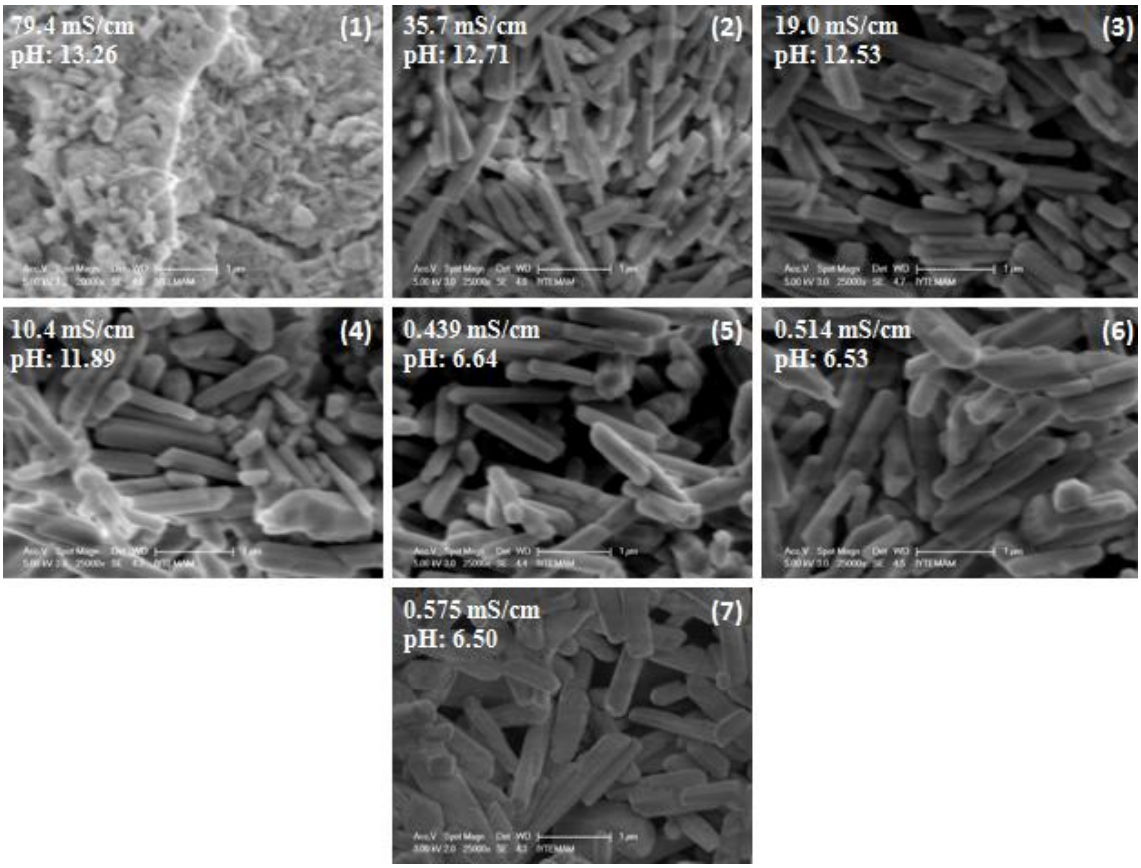

Figure 4.15. SEM images of $BaCO_3$ particles produced in 300 mM of $Ba(OH)_2.8H_2O$ solution

Figure 4.16 shows the SEM images of $BaCO_3$ particles produced in 400 mM of $Ba(OH)_2.8H_2O$. Extended hours of crystallization took place since conversion of high concentration of $Ba(OH)_2.8H_2O$ was longer. Therefore, after turning point, experiment was terminated. Due to the presence of undissolved $Ba(OH)_2.8H_2O$, $Ba(OH)_2.8H_2O$ particles were also observed in samples. The pencil-like morphology was dominant. The particle sizes were seen to increase through the end of the crystallization.

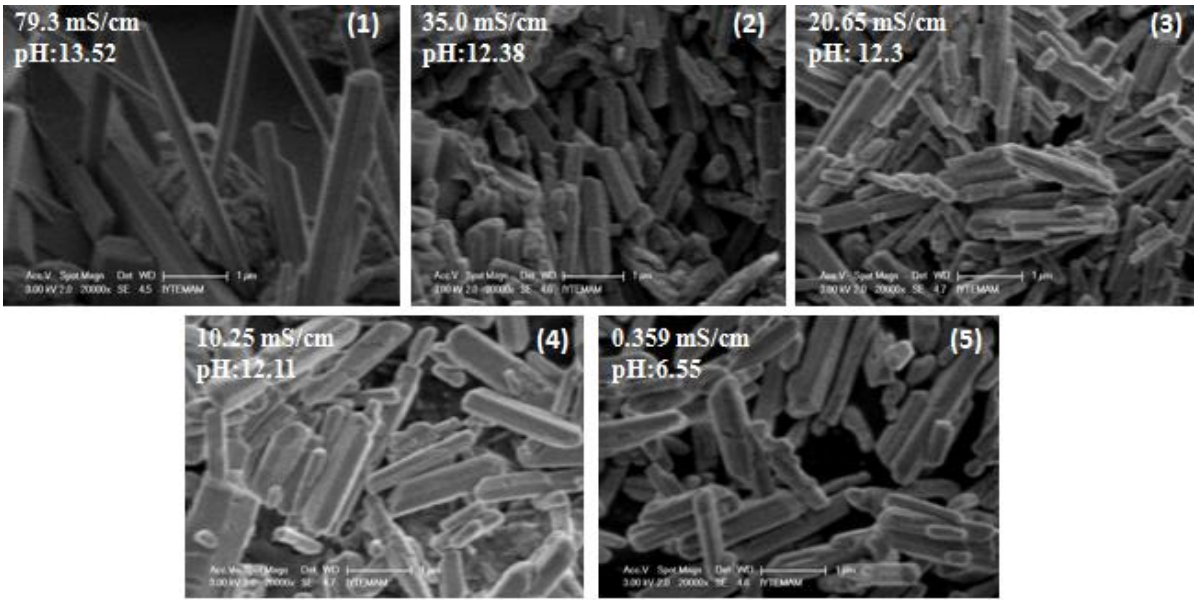

Figure 4.16. SEM images of $BaCO_3$ particles produced in 400 mM of $Ba(OH)_2.8H_2O$ solution

A proposed crystallization mechanism of $BaCO_3$ particles was given in Figure 4.17. Because the $BaCO_3$ particles were too low at the beginning of crystallization, the particles obtained after centrifugation would be the impurity in $Ba(OH)_2.8H_2O$ solution. These rod-like particles were seen as longer and thinner at Figure 4.17-(a) and (b). As crystallization progressed, as shown in Figure 4.17-(c), rod-like nano $BaCO_3$ particles produced. These particles were seen to become thinner while their lengths become longer as shown in Figure 4.17-(d) and (e). Once the Ba^{++} ions consumed completely, after turning point, the $BaCO_3$ particles were seen to grow both length wise and diameter wise as shown in Figure 4.17-(f). As CO_2 injection continued, particles were seen further to grow along its both diameter and length as shown in Figure 4.17-(g).

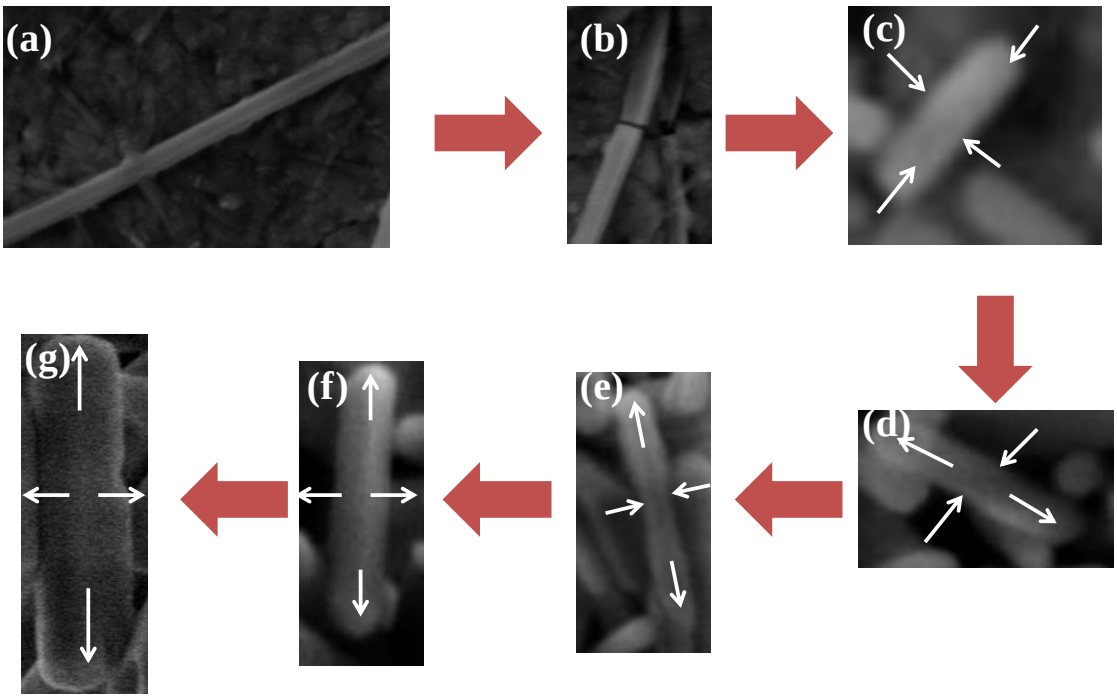

Figure 4.17. Proposed crystallization mechanism for rod-like $BaCO_3$ particles

Figure 4.18 shows the SEM images of $BaCO_3$ particles produced in different $Ba(OH)_2.8H_2O$ concentrations at the turning point of the crystallization. As can be seen from the figure, when concentration of $Ba(OH)_2.8H_2O$ increased, $BaCO_3$ particles became larger. The best rod-like morphology and the particle size distribution were observed at 80 mM $Ba(OH)_2.8H_2O$ concentration.

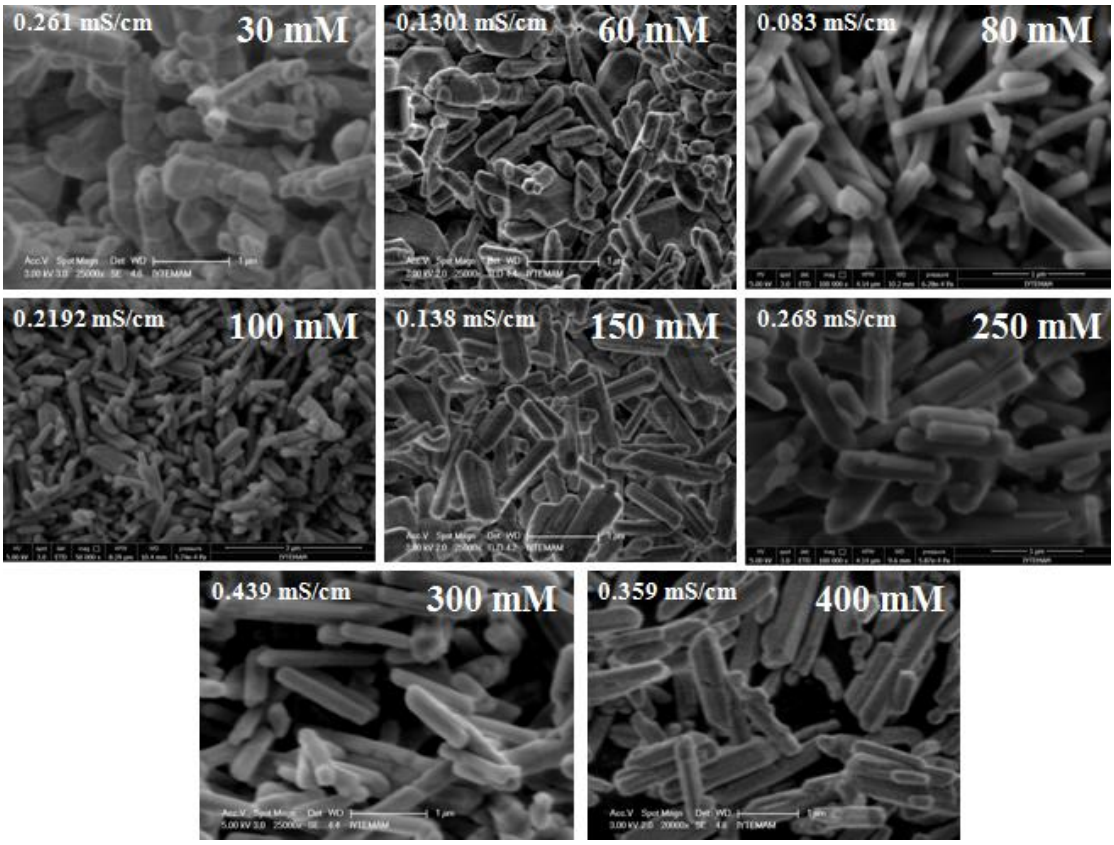

Figure 4.18. SEM images of $BaCO_3$ particles produced in different $Ba(OH)_2.8H_2O$ concentrations at the turning point when Ba^{++} ions consumed

Figure 4.19 shows the average particle diameters of $BaCO_3$ synthesized for different $Ba(OH)_2.8H_2O$ concentrations at the turning points. The rod-like particles settled much faster, the measurements of the average diameter and zeta potential values were unsuccessful. However, the diameter and length of the particles were estimated from the SEM images. At least 10 particles were scaled randomly in the SEM images and shown in the figure along with the average particle size. As can be seen in the Figure 4.19, average particle diameter was higher at the beginning of the crystallization. As the crystallization progressed, the average particle diameter decreased until the consumption of all Ba^{++} ions in the solution. Decrease in particle size might also be related to the dissolution of $BaCO_3$ particles as a result of depletion of Ba^{++} ions in the solution. When all Ba^{++} ions were consumed and CO_2 injection was continued, the average particle diameter started to increase probably due to dissolution-recrystallization mechanism of crystallization.

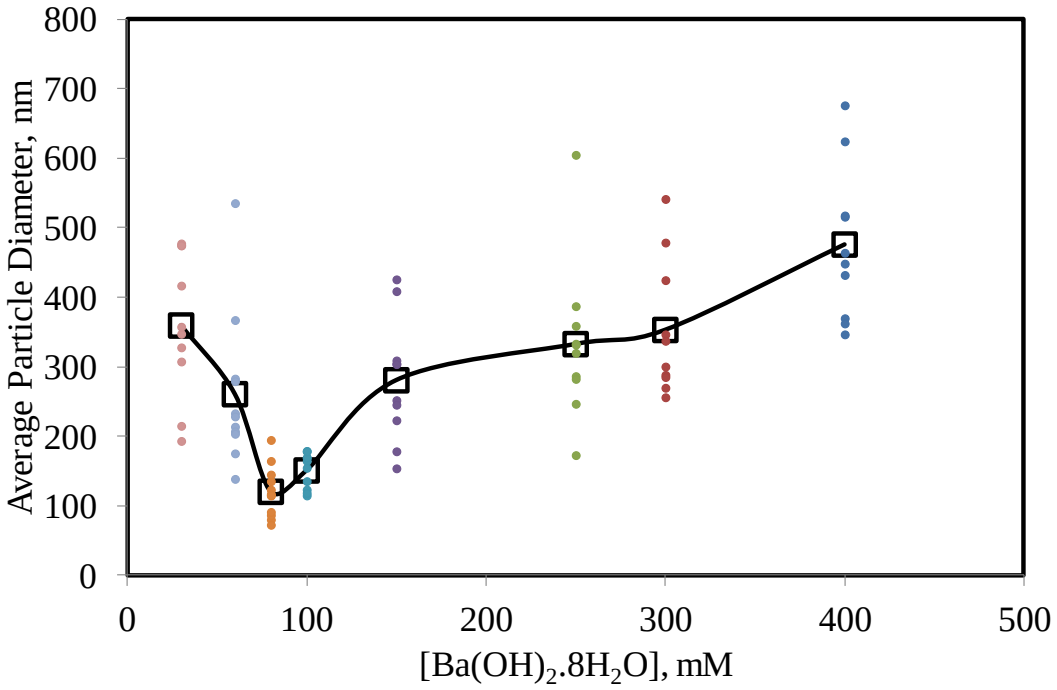

Figure 4.19. Average particle diameters for different $Ba(OH)_2.8H_2O$ concentrations at the turning points

Figure 4.20 shows the average particle diameter and aspect ratio for 80 mM of $Ba(OH)_2.8H_2O$ concentration. As can be seen in the figure, aspect ratio was small initially and increased as CO_2 was injected in the solution. However, the length of particles decreased as some of the particles dissolved in the solution. A slight increase in aspect ratio or length of the particles was seen during the crystallization. At the late stages of crystallization while average diameter of particles slightly increased, the change in length was relatively small and, as a result, aspect ratio decreased slightly. Also, reaction took place for 90 minutes for 80 mM of $Ba(OH)_2.8H_2O$.

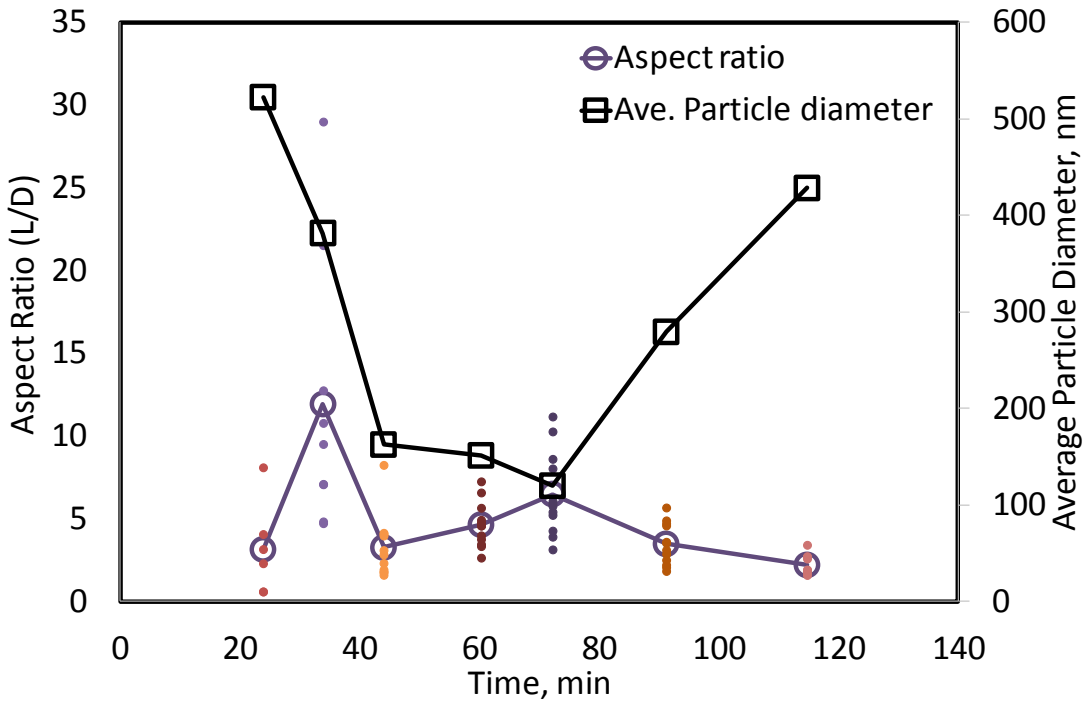

Figure 4.20. Average particle diameters and aspect ratios for 80 mM of $Ba(OH)_2.8H_2O$ concentration during $BaCO_3$ crystallization

Figure 4.21 shows the average particle diameters and aspect ratios changes with $Ba(OH)_2.8H_2O$ concentrations at the turning point. As can be seen from the figure, there was a U-trend in average particle diameter with $Ba(OH)_2.8H_2O$ concentration. The average particle diameter was higher at low $Ba(OH)_2.8H_2O$ concentrations and decreased with increasing $Ba(OH)_2.8H_2O$ concentration up to 80 mM. The $BaCO_3$ average particle diameter became larger when $Ba(OH)_2.8H_2O$ concentration increased afterwards. The aspect ratio was lower initially and almost unchanged at the higher $Ba(OH)_2.8H_2O$ concentrations. The minimum average particle diameter for $BaCO_3$ was about 120 nm at 80 mM of $Ba(OH)_2.8H_2O$ solution, however, the aspect ratio was the highest of about 7. It meant the average particle diameter was about 120 nm and the average particle length was about 840 nm. As the concentration was increased, the average particle diameter was increased to about 400 nm and aspect ratio was constant about 4; that was average diameter increased to 400 nm and length increased to 1600 nm.

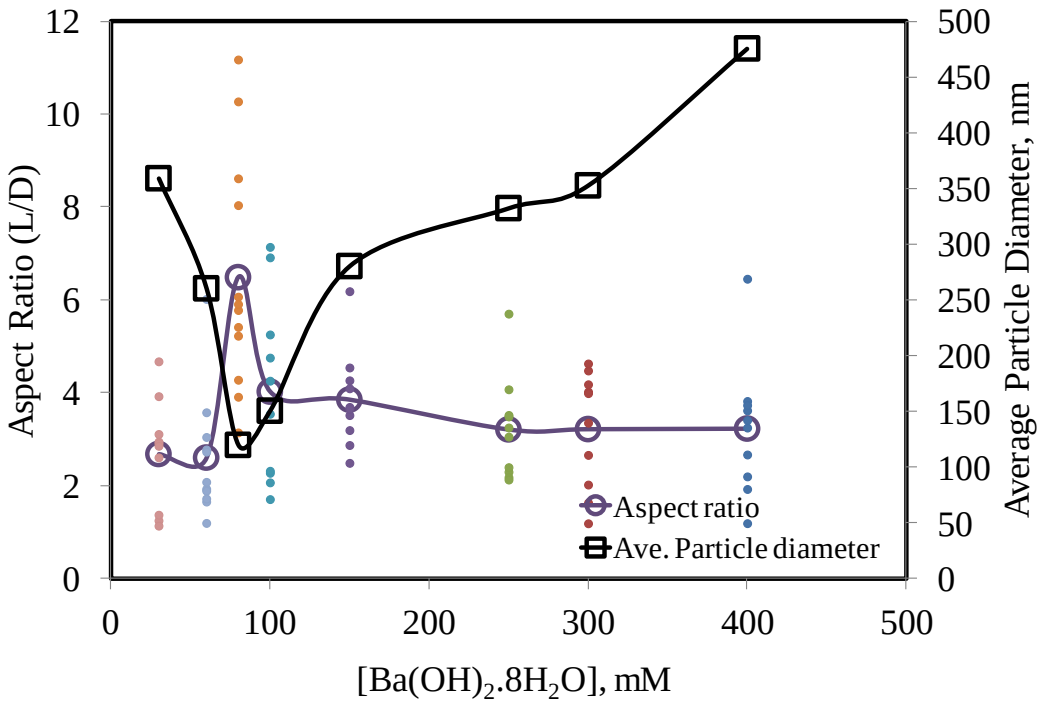

Figure 4.21. Average particle diameters and aspect ratios by changing $Ba(OH)_2.8H_2O$ concentrations at turning point

Figure 4.22 show that XRD pattern of $BaCO_3$ particles produced in 80 mM $Ba(OH)_2.8H_2O$ concentration during $BaCO_3$ crystallization process. *C* symbol shows $BaCO_3$ peaks and *H* symbol shows $Ba(OH)_2.8H_2O$ peaks. At sample 1 which was the sample collected before CO_2 injection, $Ba(OH)_2.8H_2O$ was observed as orthorhombic and monoclinic phases. At other samples, sharp and strong diffraction peaks were the same as 19, 25, 28, 35, 39, 42, 43, 44, 47, 56, 61 and 70º in 2θ degree and these peaks showed well defined orthorhombic $BaCO_3$ structure. Different $BaCO_3$ crystalline forms were not observed.

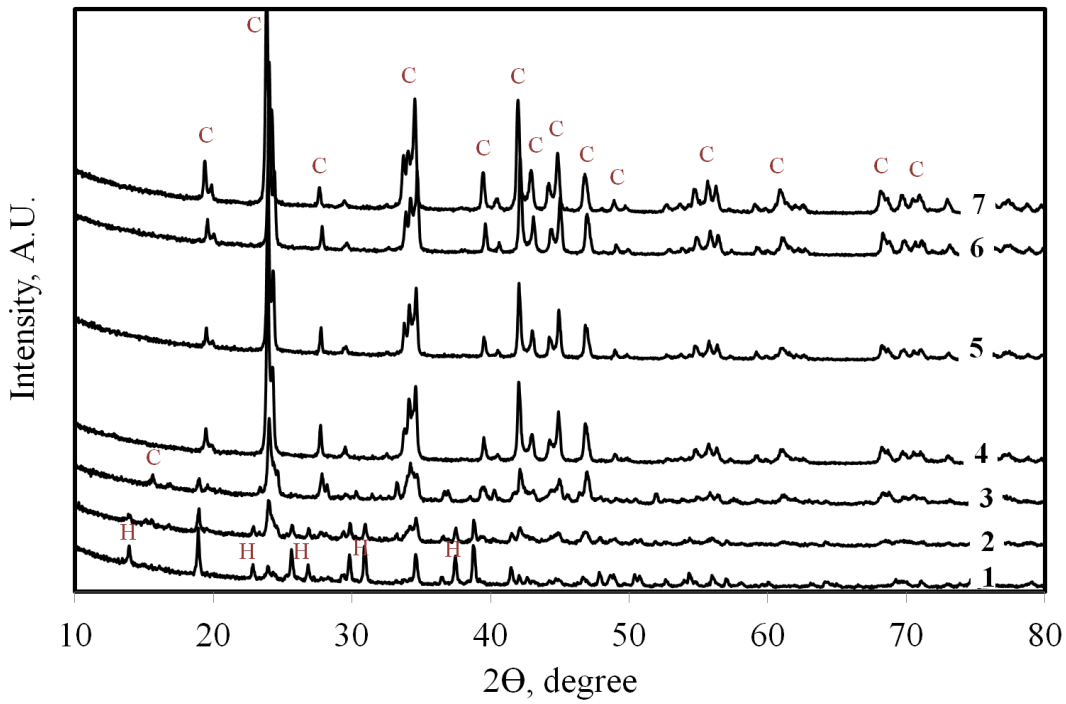

Figure 4.22. XRD pattern for $BaCO_3$ particles produced in 80 mM of $Ba(OH)_2.8H_2O$ concentration

XRD pattern of all $BaCO_3$ particles obtained at different $Ba(OH)_2.8H_2O$ concentrations at the turning point of crystallization at about zero conductivity were shown in Figure 4.23. All strong and sharp diffracted peaks were the same and identical at 19, 25, 28, 35, 39, 42, 43, 44, 47, 56, 61 and 70º in 2θ degree. These peaks were formed in orthorhombic $BaCO_3$ crystal structure without any other crystal forms.

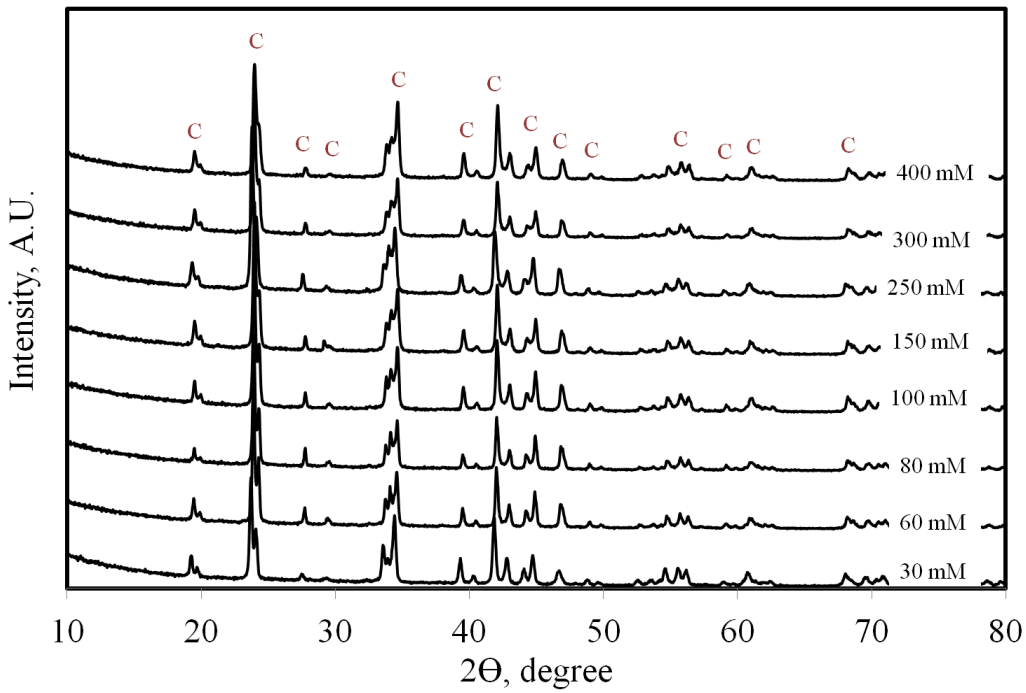

Figure 4.23. XRD pattern for all $BaCO_3$ particles obtained at different $Ba(OH)_2.8H_2O$ concentrations at turning point (about zero conductivity)

In the literature, different concentration of $BaCl_2$ was studied by hydrothermal method by Xu and Xue. When these particles were compared to the $BaCO_3$ particles synthesized in different $Ba(OH)_2.8H_2O$ concentrations, 5 µm in diameter and hexagonal pencil-like shaped of $BaCO_3$ particles were produced by them at high temperature and with long reaction times (Xu & Xue, 2006). However, in this study, $BaCO_3$ particles of diameters between 100 and 250 nm were produced at room temperature and in 90 minutes. Also, Li et al. studied the effect of concentration of $BaCl_2$ on morphology and size of $BaCO_3$ particles by microemulsion method. Despite, Li et al. produced 200 nm in diameter of belt-like $BaCO_3$ particles, at temperature varied from 140ºC to 180ºC and for 12 hours. It seemed that this thesis conditions were much more favorable compared to these methods appeared in the literature.

4.2. Effect of CO_2 Flow Rate on $BaCO_3$ Production

CO_2 dissolution rate may affect the agglomeration of particles, particle size and morphology. Therefore, influence of CO_2 flow rate on particle size, particle morphology and agglomeration of particles were investigated. By keeping other parameters constant

such as concentration of $Ba(OH)_2.8H_2O$, stirring rate, length in reaction chamber, reactor volume, temperature, liquid ($Ba(OH)_2.8H_2O$) flow rate, three CO_2 flow rates were studied. Figure 4.24-(a) and Figure 4.24-(b) show the conductivity and pH values for different CO_2 flow rates during $BaCO_3$ crystallization. Similar behavior were observed as $BaCO_3$ synthesis for different $Ba(OH)_2.8H_2O$ concentrations. As shown in the figures, the $BaCO_3$ crystallization times decreased as CO_2 injection rate into the reaction chamber was increased. It seemed that CO_2 flow rate influence the $BaCO_3$ crystallization and the crystallization rate.

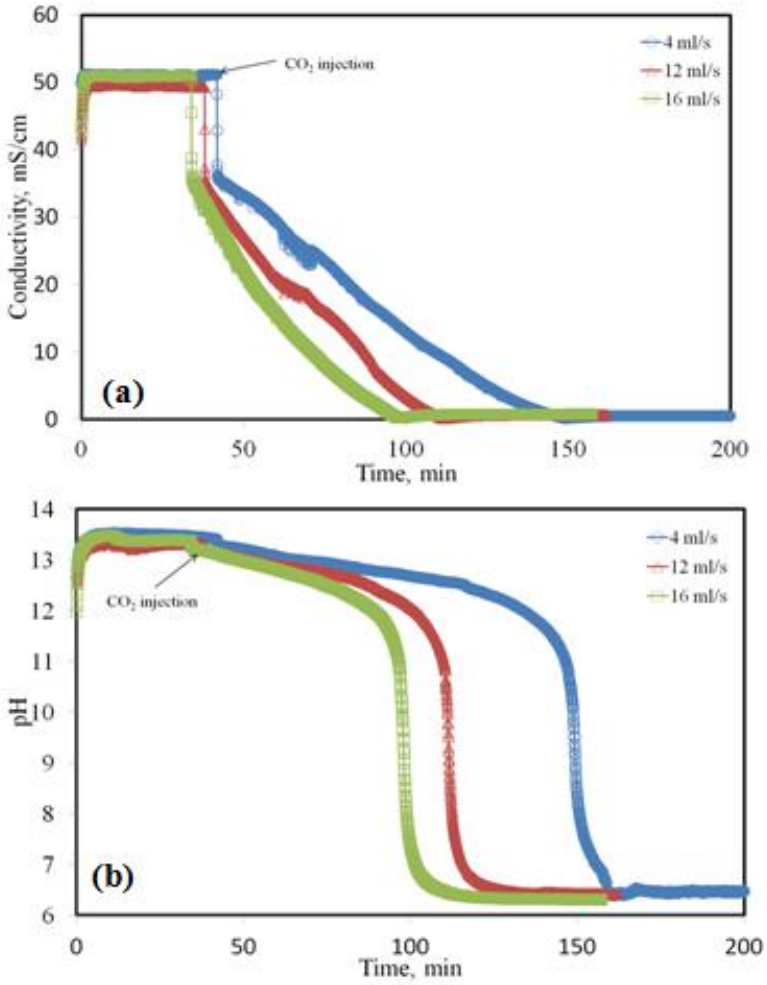

Figure 4.24. (a) Conductivity and (b) pH values at different CO_2 flow rates during $BaCO_3$ crystallization

Figure 4.25 shows the SEM images of $BaCO_3$ particles synthesized at 4 ml/s CO_2 flow rate. First sample was obtained before CO_2 injection when $Ba(OH)_2.8H_2O$

was dissolved completely. Sample 5 was obtained when the reaction was completed at the turning point of crystallization. Sample 7 was the last sample obtained at the end of the experiment. As shown in the figure, rod-like $BaCO_3$ particles were produced. At the early stages of crystallization, longer particles were produced. Through the turning point, particles became smaller. After the turning point, both the diameter and length of particles started to grow. There was a homogeneous morphological distribution.

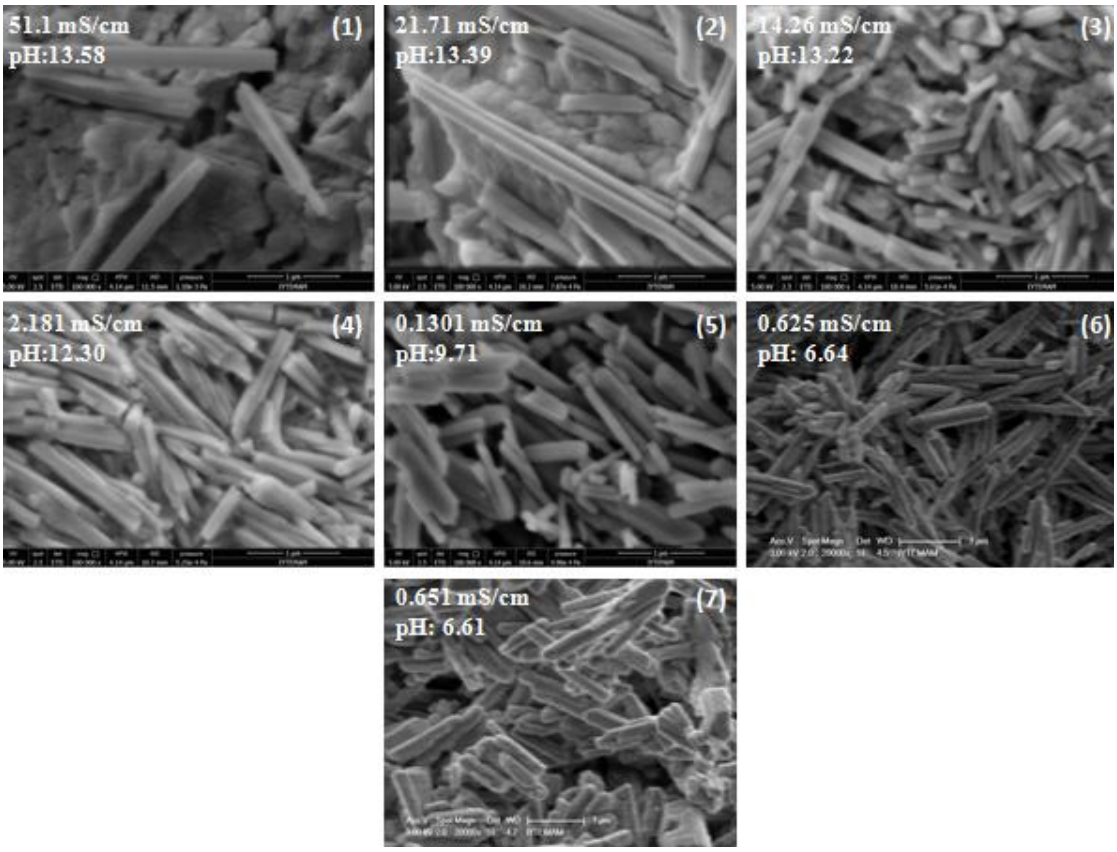

Figure 4.25. SEM images of $BaCO_3$ particles synthesized at 4 ml/s CO_2 flow rate during $BaCO_3$ crystallization

SEM images of $BaCO_3$ particles produced at 12 ml/s CO_2 flow rate were given in Figure 4.26. Despite of very bigger particles were observed at the early stages of crystallization, smaller particles were observed through the turning point. After the turning point, particles became larger. Rod-like shaped $BaCO_3$ were produced with homogeneous morphological distribution. A small amount of agglomeration was discerned.

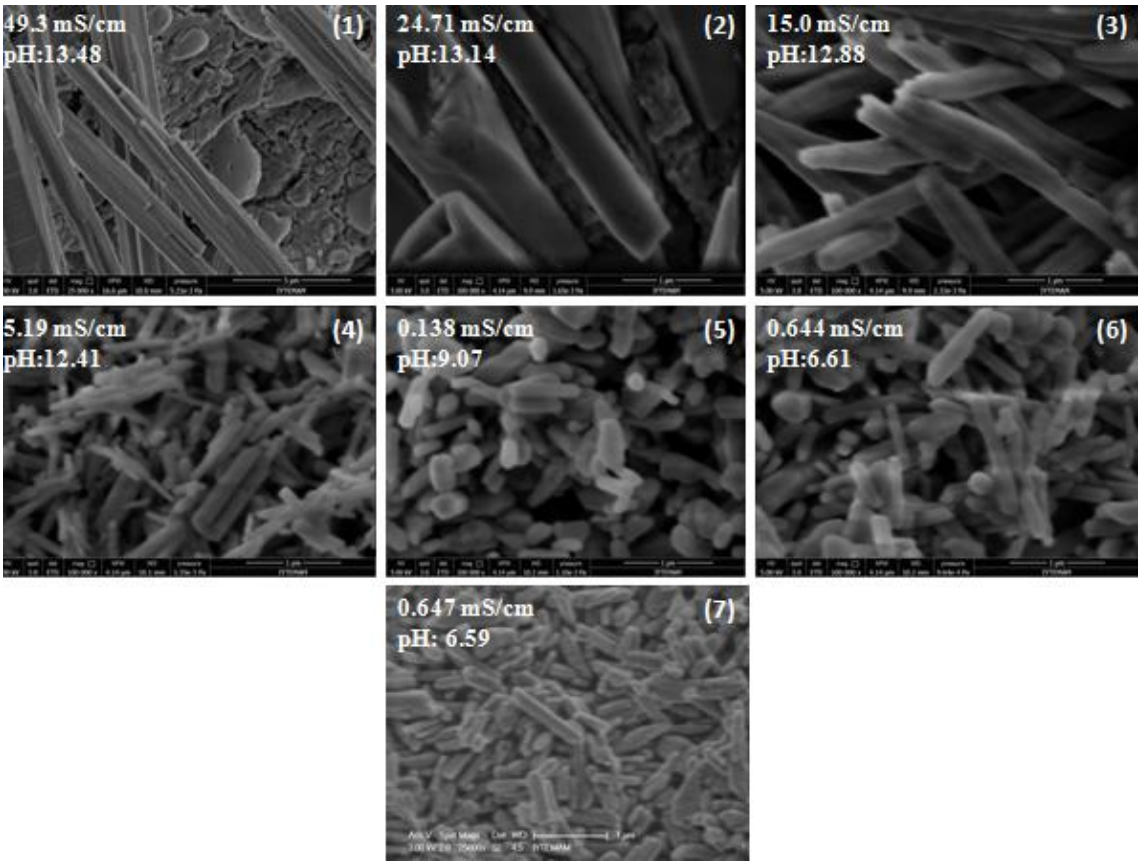

Figure 4.26. SEM images of $BaCO_3$ particles produced at 12 ml/s CO_2 flow rate during $BaCO_3$ crystallization

Figure 4.27 shows the SEM images of $BaCO_3$ particles produced at 16 ml/s CO_2 flow rate. Thick and longer particles started to dissolve at the beginning of experiment. At the early stages of crystallization, particles became smaller (sample 2). Then, it was seen that the particles started to grow with a pencil-like morphology and longer particles were observed (sample 3). Later on, regular particles with longer rod-like morphology were observed dominantly at the turning point. Particles again became longer at the end of crystallization.

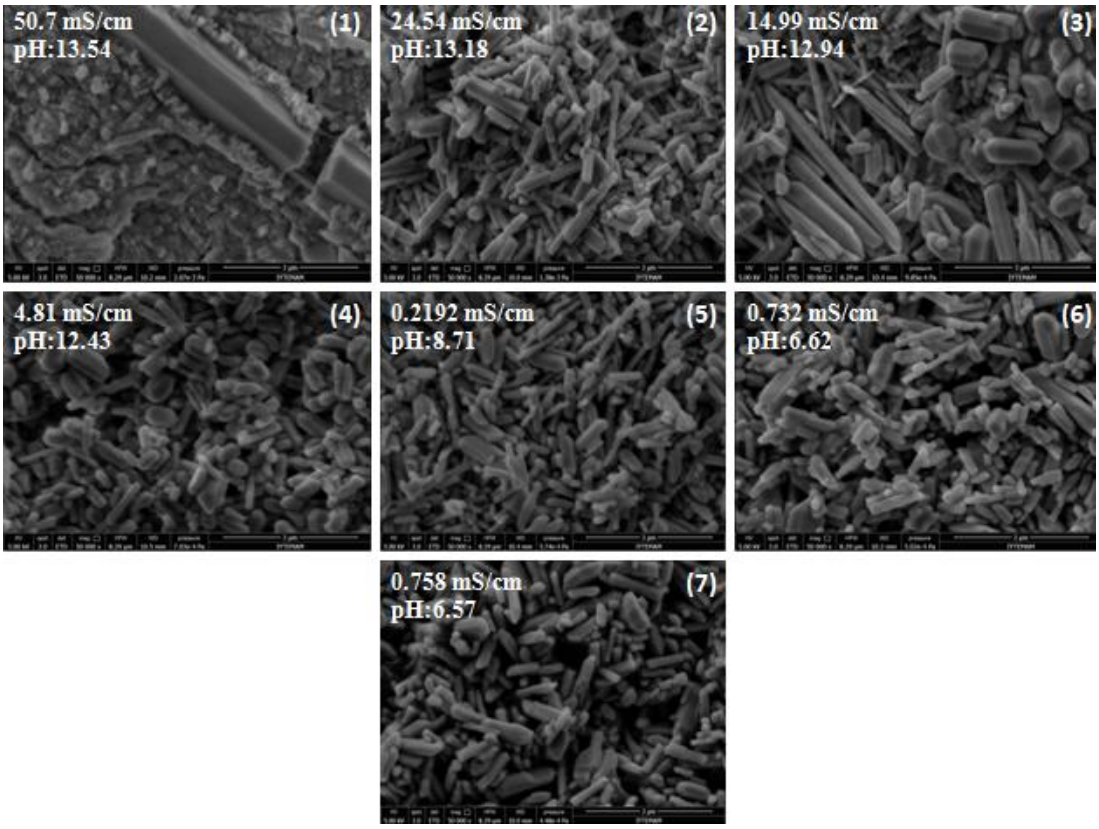

Figure 4.27. SEM images of $BaCO_3$ particles produced at 16 ml/s CO_2 flow rate during $BaCO_3$ crystallization

Figure 4.28 shows the SEM images of the $BaCO_3$ particles obtained at the turning point of crystallization for the three different CO_2 flow rates. As shown in the figure, the particle diameter slightly increased as CO_2 injection rate was increased.

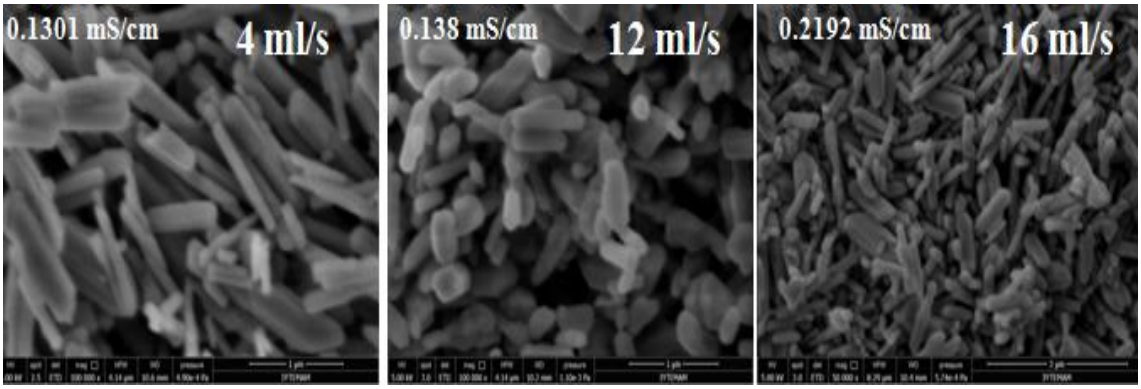

Figure 4.28. SEM images of different CO_2 flow rates on $BaCO_3$ crystallization at turning point

Figure 4.29 shows the average particle diameter and aspect ratio for the $BaCO_3$ particles at the turning point of about zero conductivity for the three CO_2 flow rates. When CO_2 flow rate was increased, average particle diameter was increased. The smallest average particle diameter was 127 nm and belonged to 4 ml/s of CO_2 flow rate. The average particle diameter slightly increased with increasing the CO_2 flow rates. However, the L/D, aspect ratio decreased significantly indicating that much smaller $BaCO_3$ particles were produced at higher CO_2 flow rates. Figure 4.30 shows the average particle diameter and aspect ratio of $BaCO_3$ particles synthesized at 4 ml/s CO_2 flow rate. As can be seen in the figure, average particle diameters varied from 120 to 400 nm. The smallest average particle diameter was 127 nm at turning point of crystallzation. Also, when average particle diameters were small, L/D ratio was increased and when average particle diameters were high through the end of the crystallization, L/D ratio was decreased.

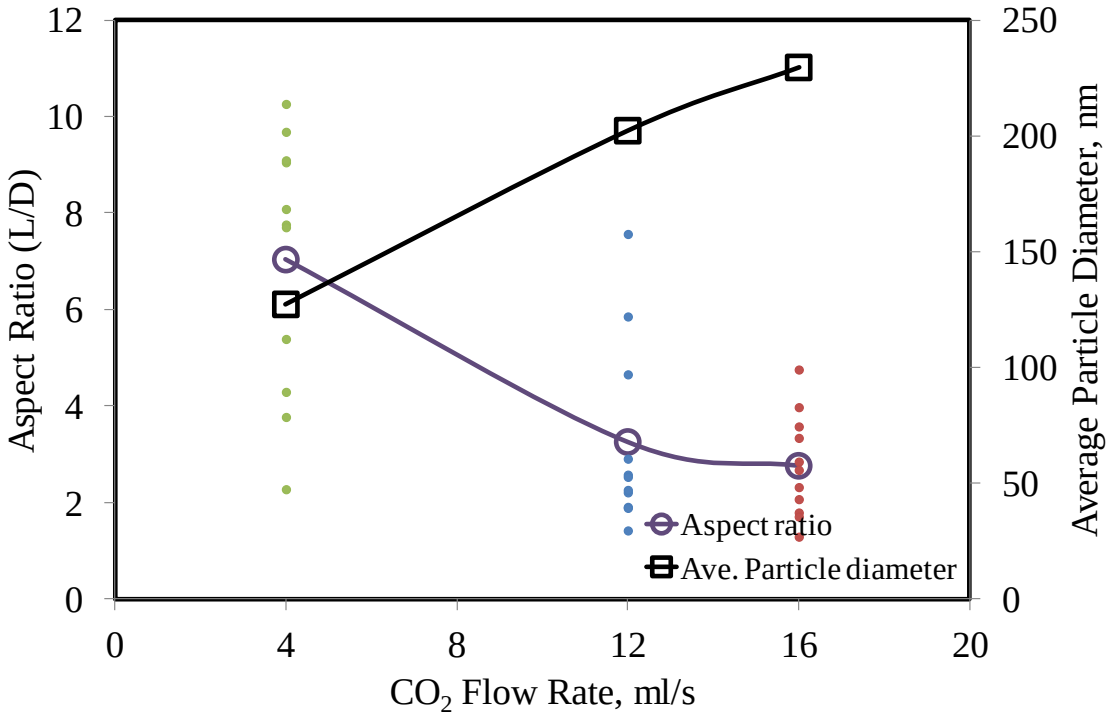

Figure 4.29. Average particle diameters and aspect ratios by changing CO_2 flow rate at turning point

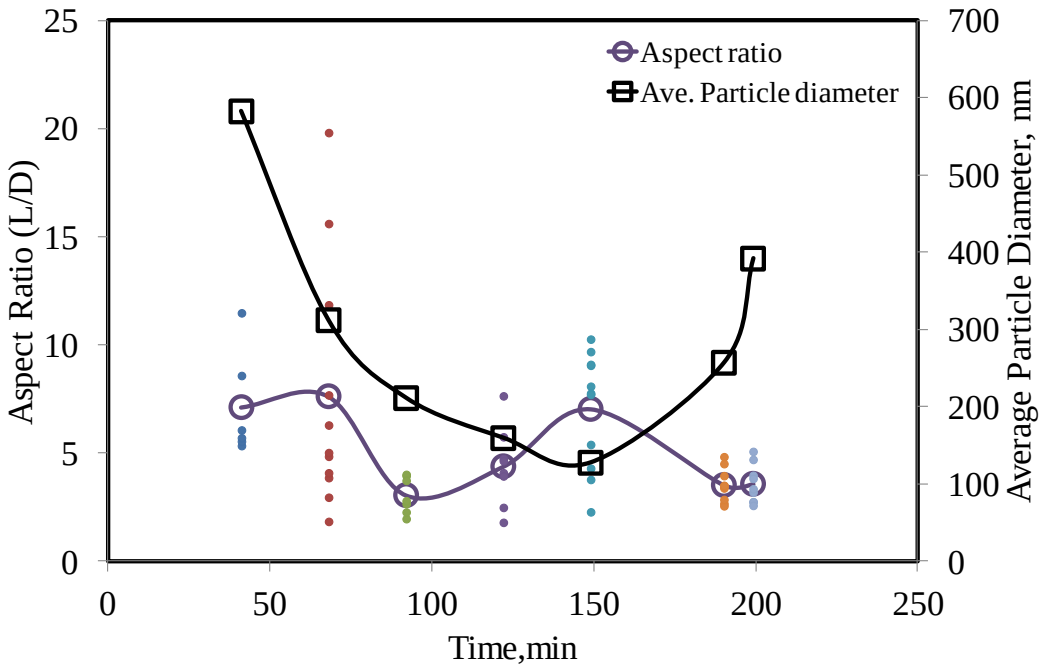

Figure 4.30. Average particle diameters and aspect ratios for 4 ml/s CO_2 flow rate during $BaCO_3$ crystallization

Figure 4.31 show the XRD pattern of produced $BaCO_3$ crystals at 4 ml/s of CO_2 flow rate. The sharp and strong diffraction peaks were the same for all samples at 4, 5, 6 and 7 as 19, 25, 28, 35, 39, 42, 43, 44, 47, 56, 61 and 70º in 2θ degree and these peaks indicated well defined orthorhombic $BaCO_3$ structure. There were no different $BaCO_3$ crystalline forms.

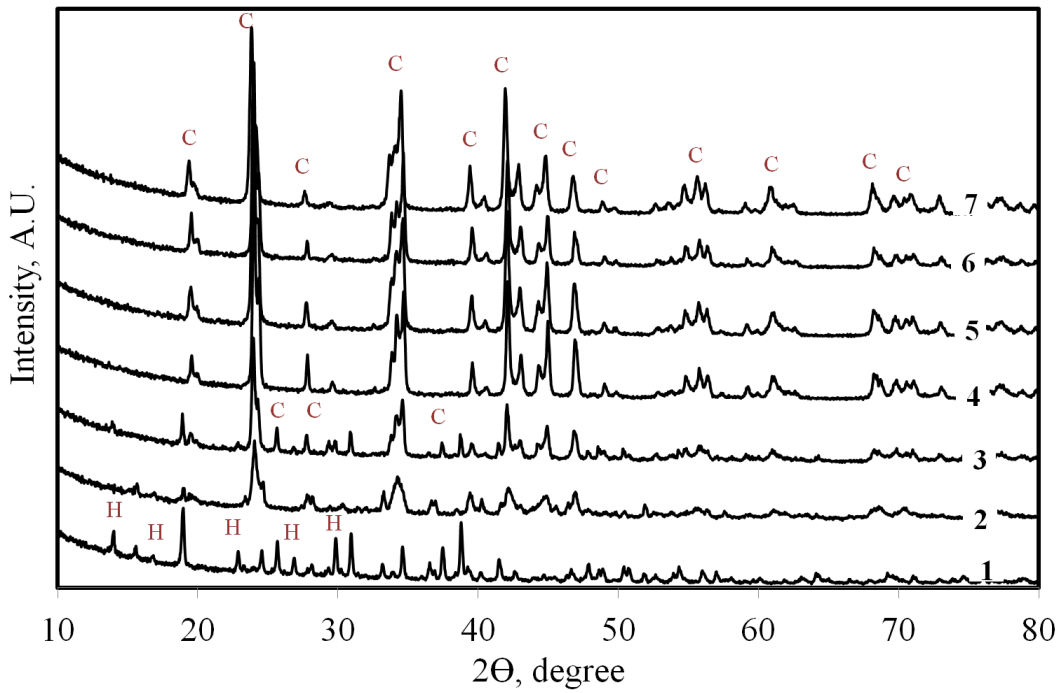

Figure 4.31. XRD pattern for 4 ml/s CO_2 flow rate during $BaCO_3$ crystallization

XRD pattern of the $BaCO_3$ particles obtained for each CO_2 flow rates at the turning points of crystallization at about zero conductivity were shown in Figure 4.32. All strong and sharp diffracted peaks were the same and identical at 19, 25, 28, 35, 39, 42, 43, 44, 47, 56, 61 and 70º in 2θ degree. These peaks were formed in orthorhombic $BaCO_3$ crystal structure without any other crystal form of $BaCO_3$.

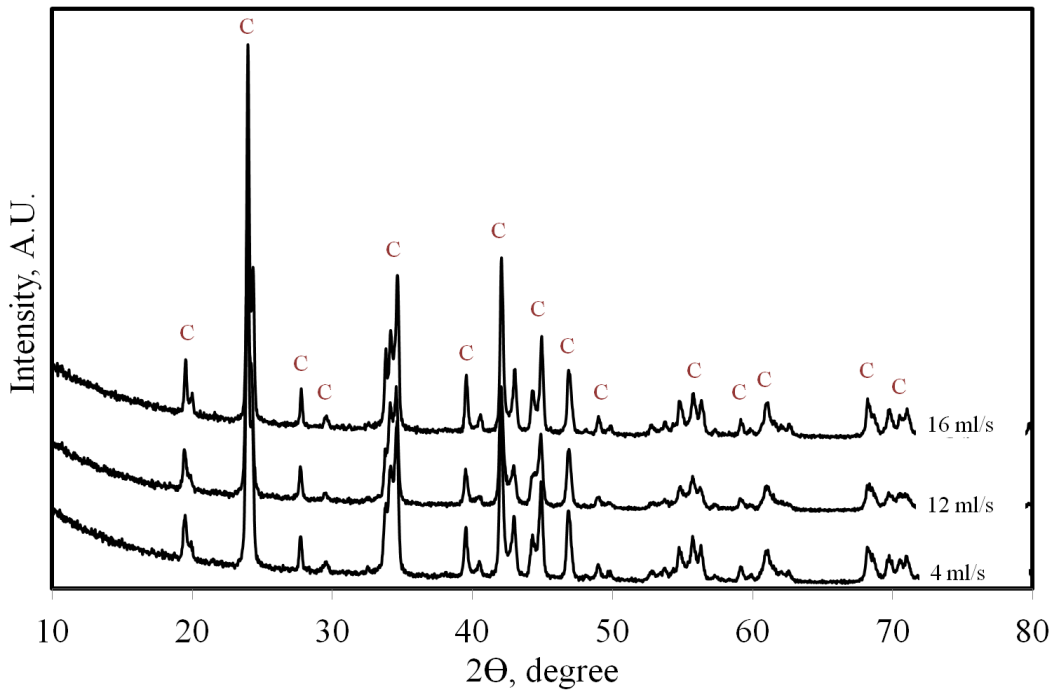

Figure 4.32. XRD pattern for all CO_2 flow rate at turning point

4.3. Effect of Length in Reaction Chamber on $BaCO_3$ Production

CO_2 dissolution rate may be controlled by varying the contact length between the liquid and gas phases. Effect of length in reaction chamber on morphology, particle size and agglomeration of $BaCO_3$ particles was investigated. By keeping other parameters constant such as concentration of $Ba(OH)_2.8H_2O$, stirring rate, CO_2 flow rate, reactor volume, temperature, liquid ($Ba(OH)_2.8H_2O$) flow rate, two different length in reaction chamber as 10 cm and 15 cm were studied. The Figure 4.33-(a) and Figure 4.33-(b) show the conductivity and pH values at two different lengths in the reaction chamber during $BaCO_3$ crystallization. Crystallization time was decreased by increasing contact length between the gas phase and liquid phase in reaction chamber. The CO_2 diffusion rate is proportional to the total contact area between the gas and liquid phases. The crystallization time became shorter for the longer contact length that for the shorter one.

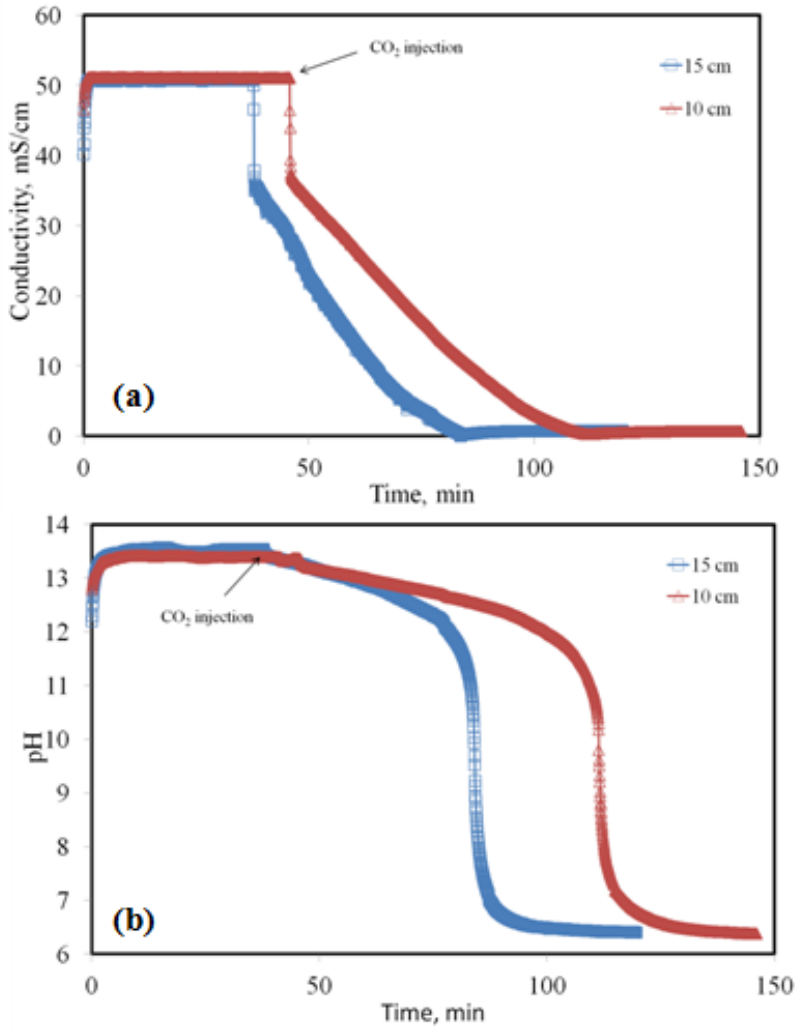

Figure 4.33. (a) Conductivity and (b) pH values at different length in reaction chamber during $BaCO_3$ crystallization

Figure 4.34 shows the SEM images of $BaCO_3$ particles obtained for 10 cm length in reaction chamber during crystallization. According to this figure, $Ba(OH)_2.8H_2O$ particles were observed on picture (1) before CO_2 injection. When CO_2 injection was started, at the early stages of crystallization, both longer and small particles were observed. Slight agglomeration was discerned before the turning point, however, the agglomeration disappeared at the turning point at about zero conductivity. During the crystallization process, a homogeneous size distribution could not be achieved due to existing of both longer and smaller particles, since rod-like shaped $BaCO_3$ particles were produced.

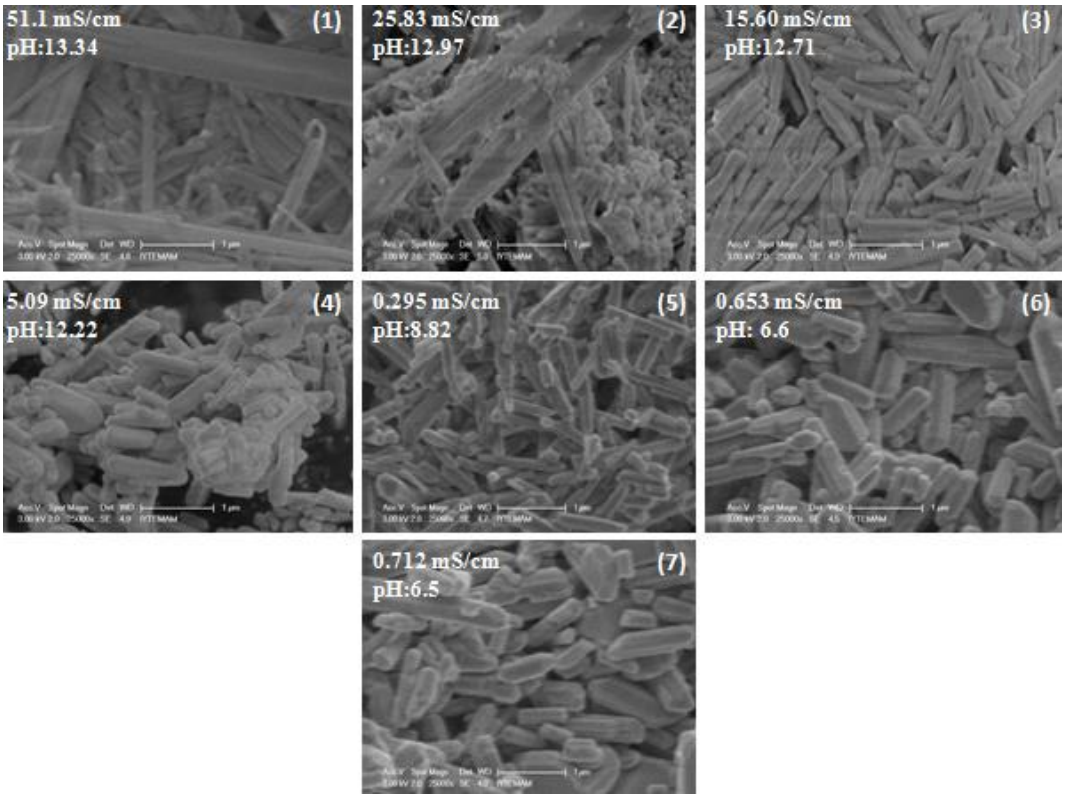

Figure 4.34. SEM images of 10 cm reaction chamber length during $BaCO_3$ crystallization

Figure 4.35 shows the SEM images of $BaCO_3$ particles obtained for 15 cm length in reaction chamber. As can be seen in the figure, almost homogeneous morphological distribution as rod-like shape and homogeneous size distribution were observed through the end of crystallization. There was negligible agglomeration when the length was higher.

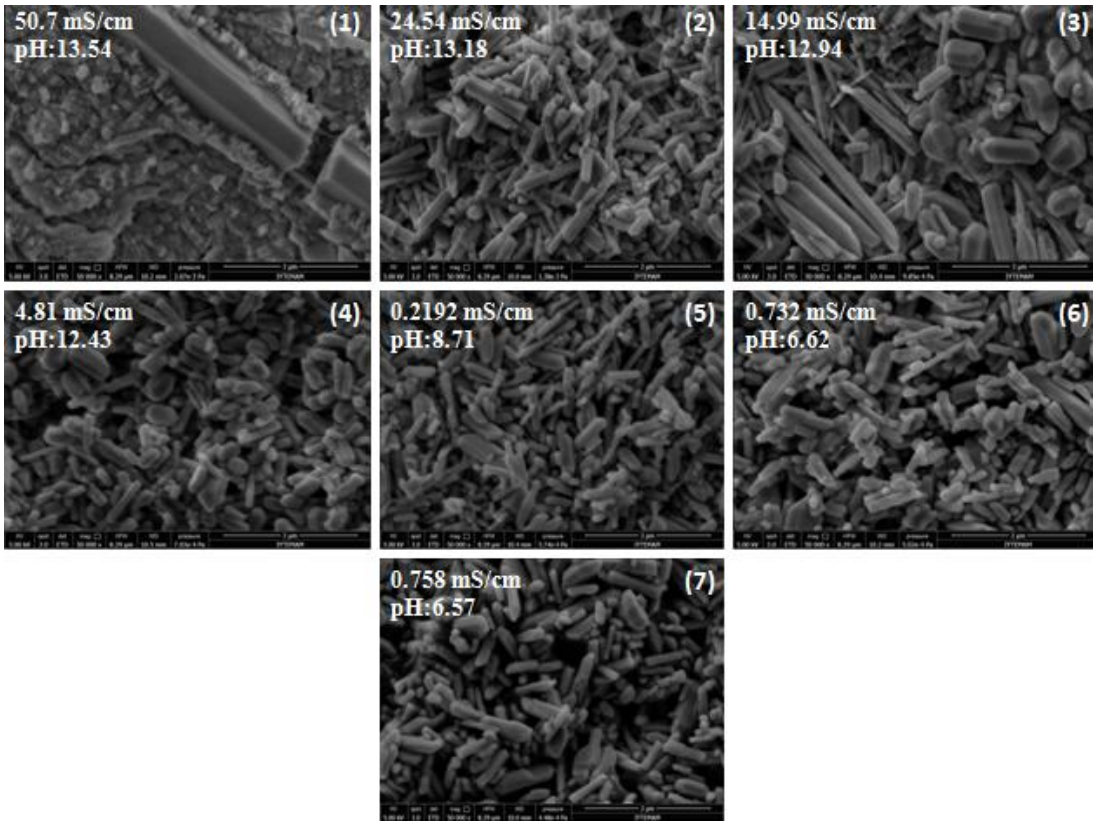

Figure 4.35. SEM images of 15 cm reaction chamber length during $BaCO_3$ crystallization

The SEM images of the $BaCO_3$ particles at the two reaction chamber lengths at the turning points at about zero conductivity shown in Figure 4.36. When length in reaction chamber was decreased, particle size slightly increased. For 10 cm length, there was no homogeneous morphological distribution while for 15 cm, it was observed as rod-like shaped $BaCO_3$ particles in everywhere. $BaCO_3$ particles which were produced by 15 cm length in reaction chamber gave the better result than that of the l0 cm one. Crystallization took place about 2 hours for 15 cm length in reaction chamber.

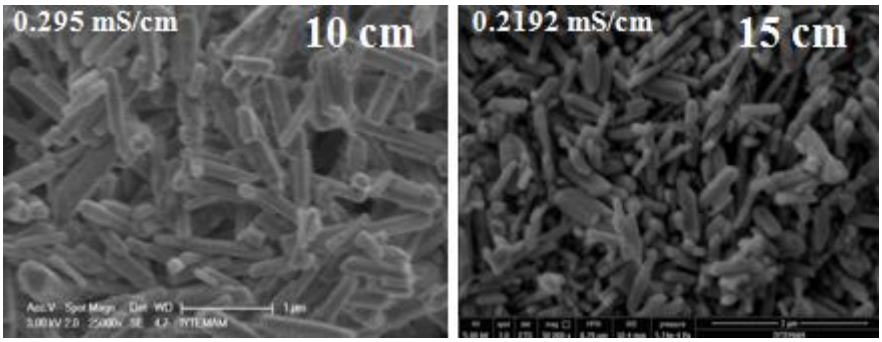

Figure 4.36. SEM images of different reaction chamber length on $BaCO_3$ crystallization at turning point (about zero conductivity)

Figure 4.37 show that average particle diameters and aspect ratios for both 10 and 15 cm length in reaction chamber at the turning points of about zero conductivity. According to this figure, average particle size of $BaCO_3$ particles decreased by increasing length in reaction chamber. 15 cm length in reaction chamber had the smallest average particle diameter at the turning point. Also, Figure 4.38 shows the average particle diameters and aspect ratios for 15 cm length in reaction chamber during $BaCO_3$ crystallization. Average particle diameters were varied between 140 and 400 nm for 15 cm length in reaction chamber during crystallization and at about zero conductivity average particle diameter was 144 nm. The aspect ratios varied slightly and were almost stable at about L/D as 4.

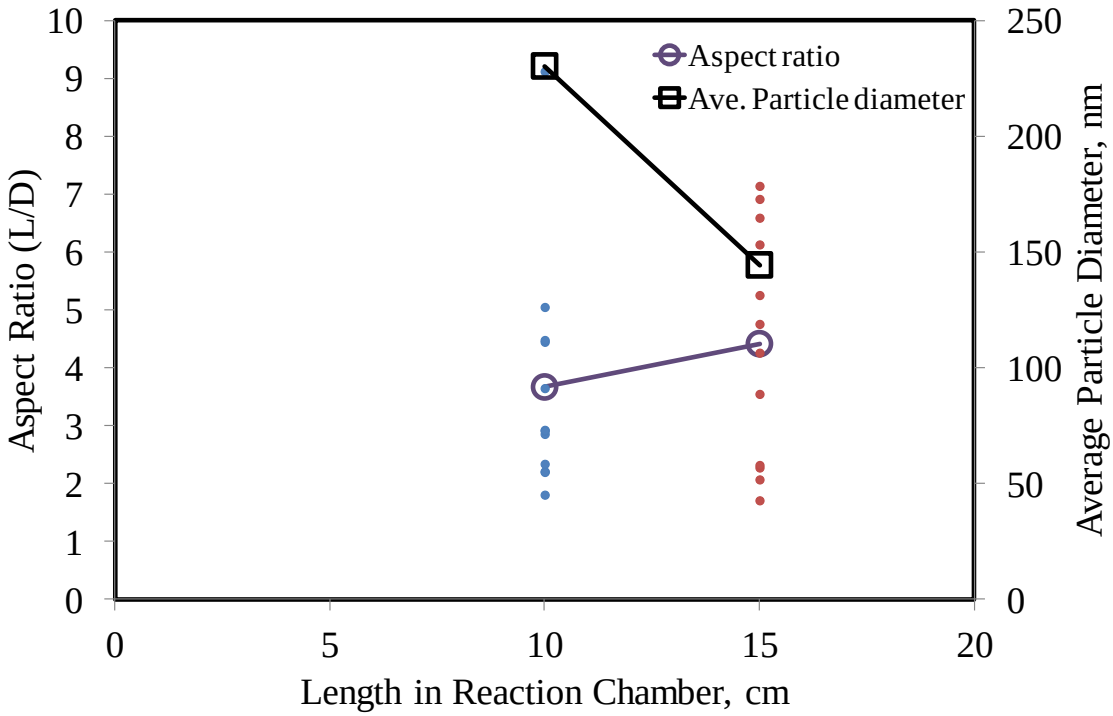

Figure 4.37. Average particle diameters and aspect ratios by changing reaction chamber length at the turning point of about zero conductivity

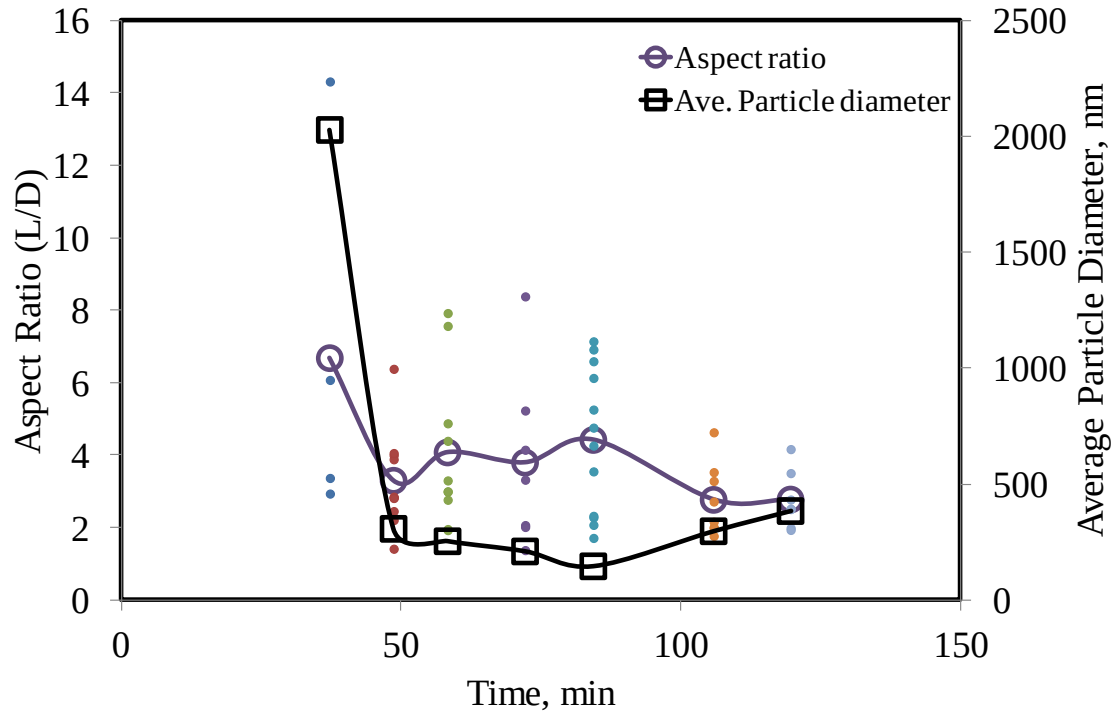

Figure 4.38. Average particle diameters and aspect ratios for 15 cm length in reaction chamber during $BaCO_3$ crystallization

XRD pattern of 10 cm and 15 cm length in reaction chamber at the turning point of about zero conductivity were shown in Figure 4.39. All strong and sharp diffracted peaks were the same and identical at 19, 25, 28, 35, 39, 42, 43, 44, 47, 56, 61 and 70º in 2θ degree. These peaks were formed in orthorhombic $BaCO_3$ crystal structure. Any other crystal forms of $BaCO_3$ were not detected.

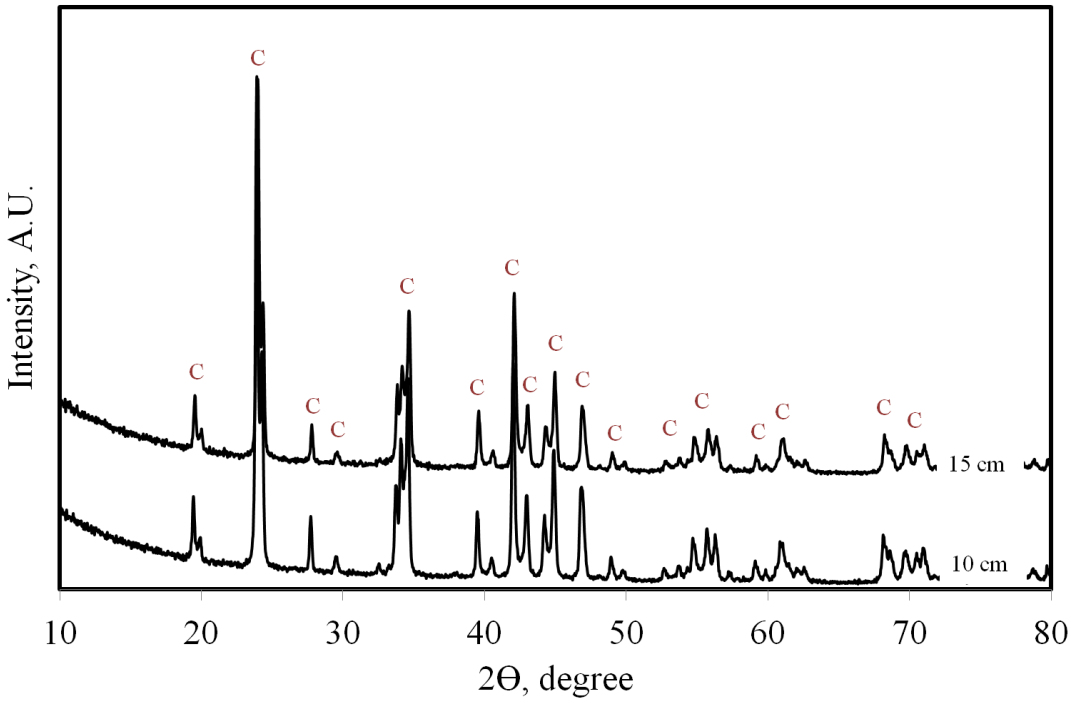

Figure 4.39. XRD pattern for 10 and 15 cm reaction chamber length at turning point

Figure 4.40 shows the XRD pattern of produced $BaCO_3$ crystals with 15 cm length in reaction chamber during $BaCO_3$ crystallization process. The sharp and strong diffraction peaks were the same for all samples in 4, 5, 6 and 7 at 19, 25, 28, 35, 39, 42, 43, 44, 47, 56, 61 and 70º in 2θ degree and these peaks gave well defined orthorhombic $BaCO_3$ structure. There were no different $BaCO_3$ crystalline forms.

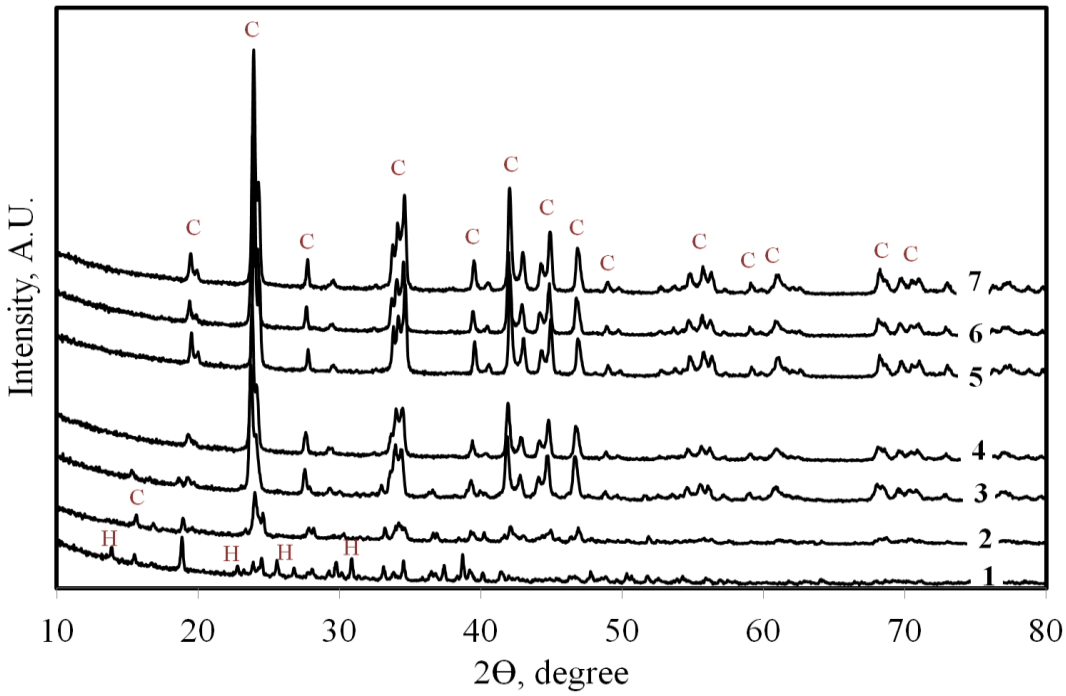

Figure 4.40. XRD pattern for 15 cm reaction chamber length during $BaCO_3$ crystallization

4.4. Effect of Stirring Rate on $BaCO_3$ Production

Effect of stirring rate on morphology, particle size and agglomeration of $BaCO_3$ particle production was investigated. By keeping other parameters constant such as concentration of $Ba(OH)_2.8H_2O$, reaction chamber length, CO_2 flow rate, reactor volume, temperature, liquid ($Ba(OH)_2.8H_2O$) flow rate, two different stirring rates as 600 and 900 rpm were studied. Stirring rate in the stabilization tank which means reactor would not directly associate with the CO_2 dissolution rate. Figure 4.41-(a) and Figure 4.41-(b) show the conductivity and pH values at different stirring rates during $BaCO_3$ crystallization. Both conductivity and pH values were identical for each stirring rates. It seems that there was no effect of stirring rate neither on $BaCO_3$ production nor on the CO_2 dissolution rates.

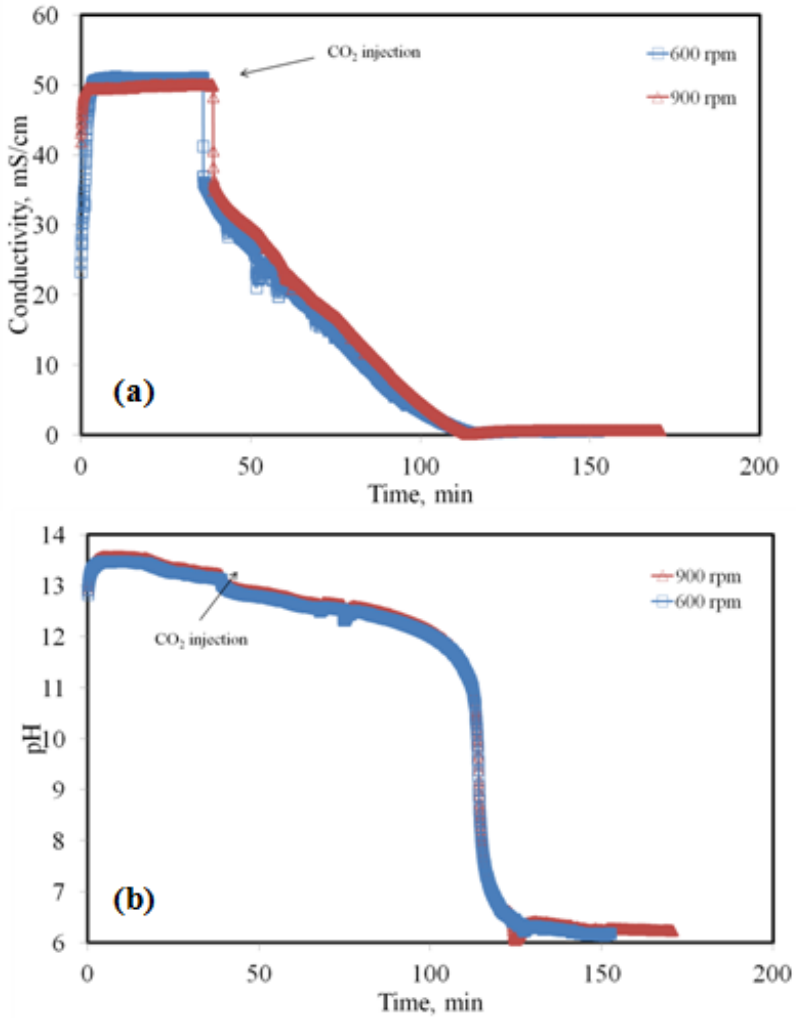

Figure 4.41. (a) Conductivity and (b) pH values at different stirring rates during $BaCO_3$ crystallization

Figure 4.42 show that SEM images of produced $BaCO_3$ particles by 600 rpm as stirring rate during $BaCO_3$ crystallization. According to this figure, homogeneous rod-like $BaCO_3$ particles were produced with homogeneous particle size. There was no agglomeration problem.

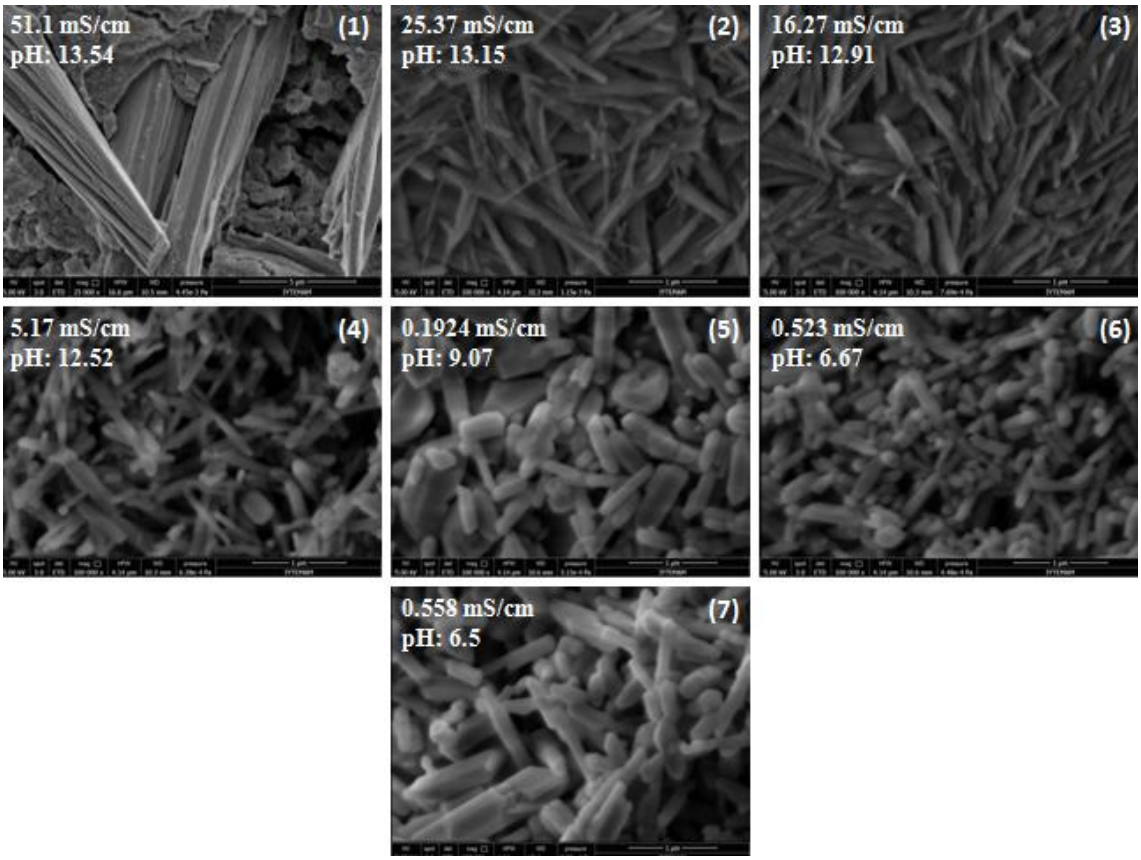

Figure 4.42. SEM images of 600 rpm during $BaCO_3$ crystallization

Figure 4.43 show that SEM images of produced $BaCO_3$ particles by 900 rpm as stirring rate during $BaCO_3$ crystallization. According to this figure, homogeneous rod-like $BaCO_3$ particles were produced with homogeneous particle size. There was no agglomeration problem.

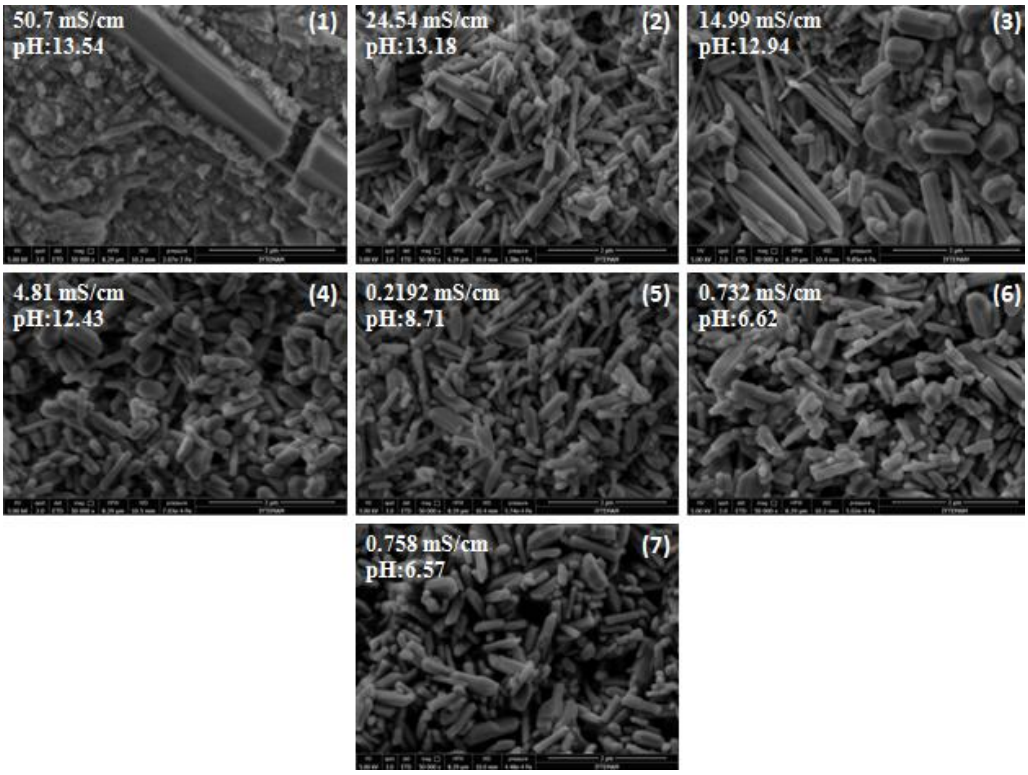

Figure 4.43. SEM images of 900 rpm during $BaCO_3$ crystallization

Figure 4.44 show that SEM images of $BaCO_3$ particles obtained at 600 and 900 rpm as stirring rates at the turning point of about zero conductivity. According to these images, despite the fact that their magnification was different in scale there was no certain difference between them.

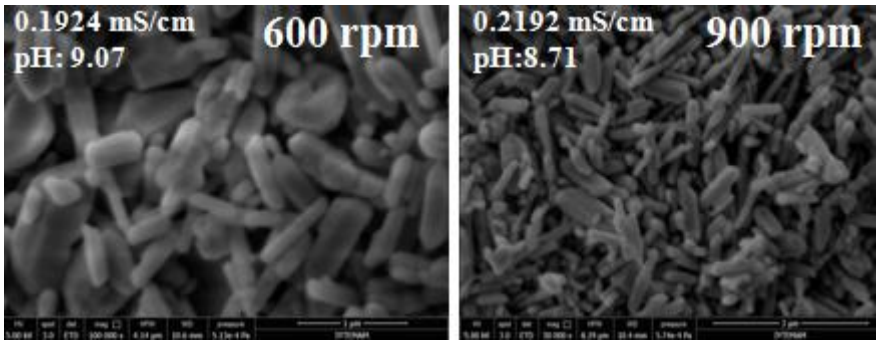

Figure 4.44. SEM images of 600 and 900 rpm at turning point about zero conductivity

Figure 4.45 show that average particle diameters and aspect ratios for the two stirring rates at the turning points of about zero conductivity. Average particle diameters were nearly same for both rpm values and also L/D ratios were nearly same.

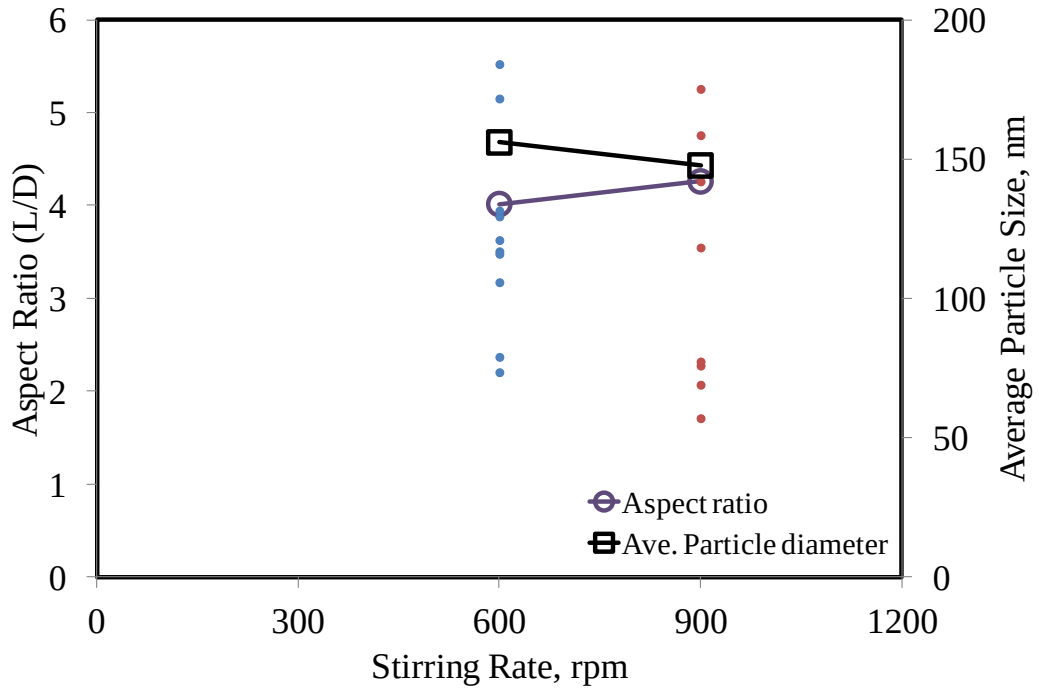

Figure 4.45. Average particle diameters and aspect ratios for all rpm values at turning points about zero conductivity

Figure 4.46 shows the XRD pattern of the $BaCO_3$ particles produced at 600 rpm and 900 rpm of stirring rates at the turning point. All strong and sharp diffracted peaks were the same and identical at 19, 25, 28, 35, 39, 42, 43, 44, 47, 56, 61 and 70º in 2θ degree. These peaks were formed in pure orthorhombic $BaCO_3$ crystal structure and there were no any other crystal forms of $BaCO_3$.

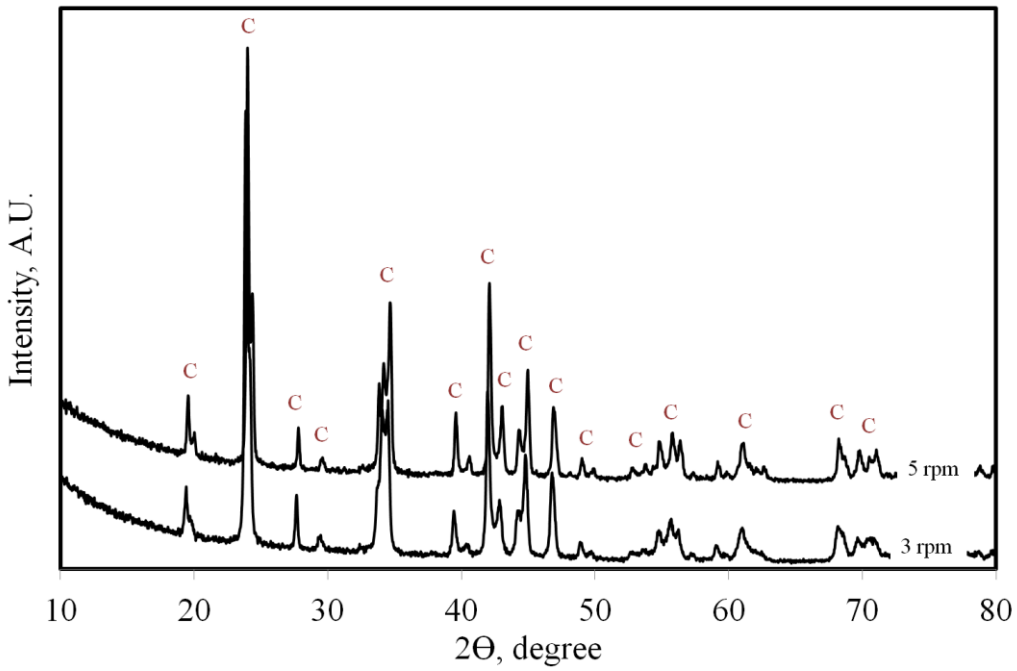

Figure 4.46. XRD pattern for 600 and 900 rpm at turning point

4.5. Effect of Circular Pipe Position for CO_2 injection on $BaCO_3$ Production

Effect of CO_2 injection level by circular pipe on $BaCO_3$ production was investigated. Other parameters such as concentration of $Ba(OH)_2.8H_2O$, temperature, stirring rate and CO_2 flow rate were kept constant. Circular pipe level was fixed as top and bottom of the reactor. Morphology of $BaCO_3$ particles was affected by contact time of gas and liquid reactants. Figure 4.47-(a) and Figure 4.47-(b) show the conductivity and pH values at different circular pipe positions during $BaCO_3$ crystallization. As shown in the figure, a sharp decrease in conductivity for the circular pipe positioned at the bottom of the tank. When the circular pipe was positioned at the top of the tank, the decrease in conductivity was lower. An acceleration was seen for the pipe placed on the top of the tank was inserted in the $Ba(OH)_2.8H_2O$ solution. The sharp decrease in conductivity indicated that CO_2 dissolve in liquid $Ba(OH)_2.8H_2O$ solution faster because there were more contact area between the gas bubbles and the water. It also shows that the $BaCO_3$ crystallization rate was higher for the pipe inserted at the bottom.

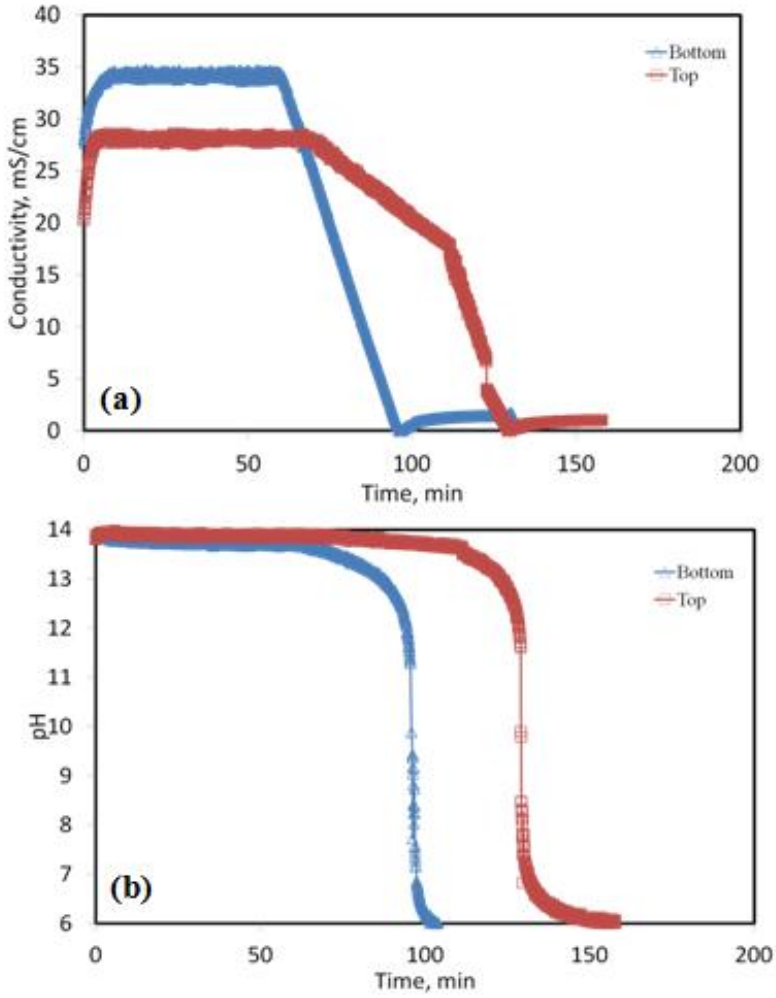

Figure 4.47. (a) Conductivity and (b) pH values for different circular pipe position during $BaCO_3$ crystallization

Figure 4.48 shows the SEM images of $BaCO_3$ particles were produced at different CO_2 injection levels by the circular pipe during $BaCO_3$ crystallization. Sample (1) shows the sample which was taken before CO_2 injection. Sample (5) shows the sample taken at the turning point of crystallization and sample (7) was taken at the end of crystallization. At the top position of circular pipe, at the beginning of experiment before CO_2 injection, dissolved $Ba(OH)_2.8H_2O$ solution were observed. On the turning point, $BaCO_3$ particles were produced in rod-like and pencil-like morphology. There was no homogeneous size and morphological distribution. At the end of crystallization, both rod-like and pencil-like $BaCO_3$ particles were observed. For the bottom position, on the turning point, rod like $BaCO_3$ particles was produced with homogeneous size and morphological distributions. The best morphology and particle sizes were observed with the bottom position of circular pipe.

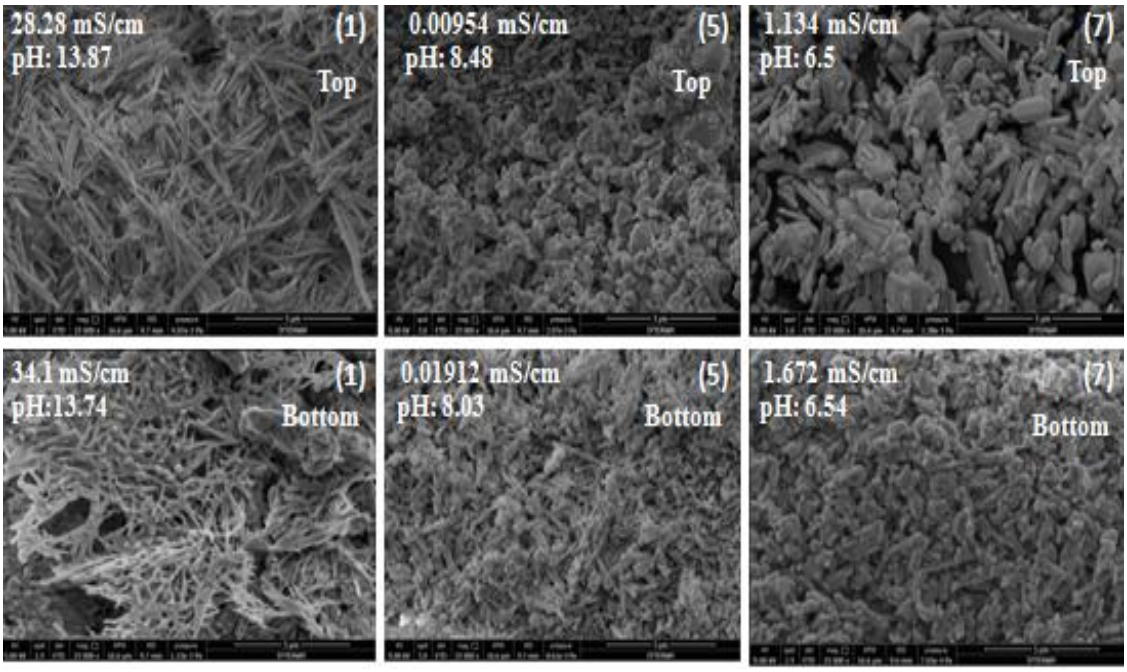

Figure 4.48. SEM images of $BaCO_3$ particles at different CO_2 injection level by circular pipe

Figure 4.49-(a) and Figure 4.49-(b) show the average particle diameter and aspect ratio for top and bottom positions of circular pipe to inject CO_2 to the system during $BaCO_3$ crystallization. At the beginning of crystallization particles had higher average diameter and smaller aspect ratio. At the turning point, the smallest average particle diameter was 150 nm for the top position. Average particle diameters became larger through the end of the crystallization. At the turning point, the smallest average particle diameter was 139 nm for bottom position. Average particle diameters became larger through the end of the crystallization. On the bottom position, the smallest average particle diameter was provided as 139 nm than top one.

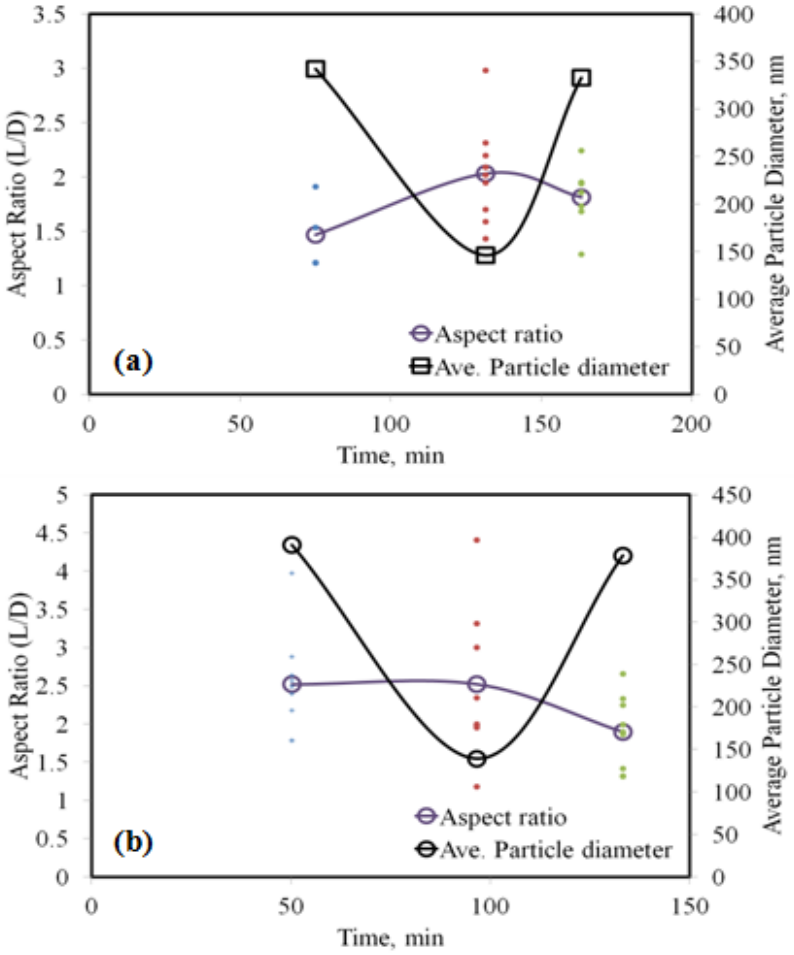

Figure 4.49. Average particle diameters and aspect ratios for (a) top position and (b) bottom position as circular CO_2 injection level during $BaCO_3$ crystallization

Figure 4.50 shows the XRD pattern of $BaCO_3$ particles produced when the circular pipe was at the top and bottom positions as the CO_2 injection level. The *b* symbol shows bottom position and *t* symbol shows top position. The b-i and t-i show initial sample (1). The only pattern for the first sample before CO2 injection, were different than the others. The b-0 and t-0 show the peaks on turning point and b-f and t-f show the peaks at the end of crystallization .The strong and sharp diffractions show that these samples were orthorhombic $BaCO_3$ for b-f, t-f, b-0 and t-0 and also there were no any different peaks detected. Different $BaCO_3$ crystalline forms were not observed.

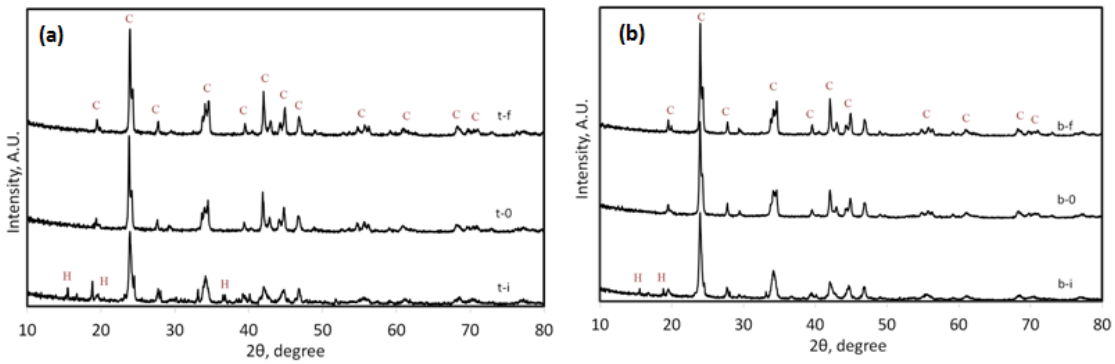

Figure 4.50. XRD pattern for $BaCO_3$ particles at (a) top and (b) bottom CO_2 injection level by circular pipe

CHAPTER 5

CONCLUSION

Small penetration method, which was initially developed to produce hollow nano $CaCO_3$, was used to produce nano $BaCO_3$ particles. Effects of $Ba(OH)_2.8H_2O$ concentration, CO_2 flow rate, gas-liquid contact area as the length in reaction chamber, and stirring rates on the particle size and morphology were studied. It was found that conductivity of $Ba(OH)_2.8H_2O$ solution was linearly related to the $Ba(OH)_2.8H_2O$ concentration up to its solubility limit which was defined as 150 mM of $Ba(OH)_2.8H_2O$. The linearity was related to the Ba^{++} ion concentration. The produced $BaCO_3$ particles were characterized by SEM and XRD analysis. The SEM images of particles indicated rod-like and pencil-like $BaCO_3$ particles. The XRD patterns indicated that these particles were orthorhombic $BaCO_3$ and no other crystal structure was detected. Therefore, hollow nano $BaCO_3$ particles could not be produced as occurred for the $CaCO_3$ particles. There was an U-shape in particle size with respect to $Ba(OH)_2.8H_2O$ concentration. The average particle diameters decreased as concentration of $Ba(OH)_2.8H_2O$ increased up to 80 mM and it increased as the $Ba(OH)_2.8H_2O$ concentration further increased. Average particle sizes were varied between 100 nm and 400 nm during $BaCO_3$ crystallization and average particle size of $BaCO_3$ particles were 120 nm at about zero conductivity for 80 mM of $Ba(OH)_2.8H_2O$ concentration. Different CO_2 flow rates were studied to produce $BaCO_3$ particles. Crystallization time was decreased by increasing CO_2 flow rate. The average particle diameter was found as 127 nm at about zero conductivity at 4 ml/s of CO_2 flow rate. Different gas-liquid contact area as the length in reaction chamber was studied. Crystallization time was decreased by increasing the length in reaction chamber. Particle size of produced $BaCO_3$ particles was decreased when length in reaction chamber was increased. The average particle diameter was observed as 144 nm at about zero conductivity for 15 cm length in reaction chamber. Different stirring rates did not affect the morphology and sizes of $BaCO_3$ particles. Circular pipe was set to top and bottom position for CO_2 injection. Crystallization time was decreased by bottom position due to high contact

area between liquid and gas reactants. Rod-like $BaCO_3$ particles of 139 nm were produced at about zero conductivity for bottom position of circular pipe.

It was shown that rod-like shaped orthorhombic $BaCO_3$ particles were produced in nano sizes between 100 and 400 nm of diameter and aspect ratio from 3 to 10 with almost homogeneous size distributions.

REFERENCES

Alavi, M. A., & Morsali, A. (2008). Syntheses of $BaCO_3$ nanostructures by ultrasonic method. *Ultrasonics sonochemistry, 15*(5), 833-838.

Chen, J., & Shao, L. (2003). Mass production of nanoparticles by high gravity reactive precipitation technology with low cost. *China Particuology, 1*(2), 64-69.

Chen, P.-C., Cheng, G., Kou, M., Shia, P., & Chung, P. (2001). Nucleation and morphology of barium carbonate crystals in a semi-batch crystallizer. *Journal of crystal Growth, 226*(4), 458-472.

Chen, P.-C., Shi, W., Du, R., & Chen, V. (2014). Crystallization kinetics of barium carbonate crystals in a lab-scale bubble-column scrubber. *Journal of the Taiwan Institute of Chemical Engineers, 45*(5), 2418-2426.

Cho, Y.-S., & Huh, Y.-D. (2012). Synthesis of self-assembled urchin-like superstructures of $BaCO_3$. *Materials Research Bulletin, 47*(11), 3709-3712.

Dadkhah, M., Salavati-Niasari, M., & Davar, F. (2013). A new inorganic framework in the synthesis of barium carbonate nanoparticles via convenient solid state decomposition route. *Advanced Powder Technology, 24*(1), 14-20.

Hong, T., Chen, F., & Xia, C. (2015). Barium carbonate nanoparticle as high temperature oxygen reduction catalyst for solid oxide fuel cell. *Electrochemistry Communications, 51*, 93-97.

Hong, T., Chen, F. L., & Xia, C. R. (2015). Barium carbonate nanoparticle to enhance oxygen reduction activity of strontium doped lanthanum ferrite for solid oxide fuel cell. *Journal of Power Sources, 278*, 741-750. doi:10.1016/j.jpowsour.2014.12.137

Kaszuwara, W., Witkowski, A., Leonowicz, M., Pawlik, P., & Paszula, J. (2008). Effect of Milling Medium on the Structure and Magnetic Properties of Mechanically Alloyed Barium Ferrite. *Reviews on Advanced Materials Science, 18*(6), 497-500. Retrieved from <Go to ISI>://WOS:000260615400002

Khorsand, M. R., Habibian, M., Rohani, N., & Zarei, A. R. (2010). Determination of Crystal Growth Rate and Morphology of Barium Carbonate Crystals in a Semi-batch Crystallizer. *Iran. J. Chem. Chem. Eng. Vol, 29*(1).

Li, L., Chu, Y., Liu, Y., Dong, L., Huo, L., & Yang, F. (2006). Microemulsion-based synthesis of $BaCO_3$ nanobelts and nanorods. *Materials Letters, 60*(17), 2138-2142.

Moayyer, H. A., Ataie, A., Nozari, A., & Jafari, S. (2013). *One-step Synthesis of $BaCO_3$ Nano-particles Via Mechano-chemical Method.* Paper presented at the Advanced Materials Research.

Moguel, L. F., Muhr, H., Dietz, A., & Plasari, E. (2010). CFD simulation of barium carbonate precipitation in a fluidized bed reactor. *Chemical Engineering Research and Design, 88*(9), 1206-1216.

Omrani, A., Rostami, A. A., & Sedaghat, E. (2010). Kinetics of cure for a coating system including DGEBA (n=0)/1,8-NDA and barium carbonate. *Thermochimica Acta, 497*(1-2), 21-26. doi:10.1016/j.tca.2009.08.004

Shamsipur, M., Pourmortazavi, S. M., Hajimirsadeghi, S. S., & Roushani, M. (2013). Applying Taguchi robust design to the optimization of synthesis of barium carbonate nanorods via direct precipitation. *Colloids and Surfaces a-Physicochemical and Engineering Aspects, 423*, 35-41. doi:10.1016/j.colsurfa.2013.01.042

Tai, C. Y., & Liu, H.-s. (2006). Synthesis of submicron barium carbonate using a high-gravity technique. *Chemical engineering science, 61*(22), 7479-7486.

Tipcompor, N., Thongtem, T., Phuruangrat, A., & Thongtem, S. (2012). Characterization of $SrCO_3$ and $BaCO_3$ nanoparticles synthesized by cyclic microwave radiation. *Materials Letters, 87*, 153-156. doi:10.1016/j.matlet.2012.08.002

Xu, J., & Xue, D. (2006). Chemical synthesis of $BaCO_3$ with a hexagonal pencil-like morphology. *Journal of Physics and Chemistry of Solids, 67*(7), 1427-1431. doi:10.1016/j.jpcs.2006.01.105

Zak, A. K., Hashim, A. M., & Darroudi, M. (2014). Optical properties of $ZnO/BaCO_3$ nanocomposites in UV and visible regions. *Nanoscale Research Letters, 9*. doi:Artn 399.10.1186/1556-276x-9-399

Zelati, A., Amirabadizadeh, A., & Kompany, A. (2011). Preparation and characterization of barium carbonate nanoparticles. *International Journal of Chemical Engineering and Applications, 2*(4), 299.

Zelati, A., Amirabadizadeh, A., Kompany, A., & Larimi, Z. M. Synthesis of $BaCO_3$ Nanopowder by the Gel-combustion Method at Different Calcination Temperatures and Characterization of the Samples by TEM and XRD.

Zeng, C., Li, P., Xu, H., Xu, Z., Li, H., & Zhang, Y. (2011). Chemical synthesis of nanosized $BaCO_3$ with a pillar-like morphology. *Ceramics International, 37*(4), 1215-1218.

Zhao, H., Shao, L., & Chen, J.-F. (2010). High-gravity process intensification technology and application. *Chemical Engineering Journal, 156*(3), 588-593.

http://www.merckmillipore.com, Accessed on June 6th, 2016

https://en.wikipedia.org/wiki/Solubility_table, Accessed on June 5th, 2016

http://mam.iyte.edu.tr/, Accessed on June 5th, 2016